

MODELLING OF MULTICOMPONENT MULTIPHASE DIFFUSION
IN CONDENSED CRYSTALLINE SYSTEMS
USING ATOM JUMP FREQUENCIES

By
COIMBATORE VENKATESWARAN ISWARAN

A DISSERTATION PRESENTED TO THE GRADUATE SCHOOL OF THE UNIVERSITY
OF FLORIDA IN PARTIAL FULFILLMENT OF THE REQUIREMENTS FOR THE
DEGREE OF DOCTOR OF PHILOSOPHY

UNIVERSITY OF FLORIDA

1993

Copyright 1993

by

Coimbatore Venkateswaran Iswaran

Dedicated

to my

MOTHER

***who, unfortunately, did not
live to see this project
come to fruition***

and my

FATHER

***with the hope that I merit
his patience
and understanding
and his faith in me***

ACKNOWLEDGEMENTS

Words are inadequate to describe my gratitude to Pallavoor N. Vaidyanathan, whose unwavering faith in my ability to see this project to its conclusion, I am happy to say, has not been in vain.

I would like to extend my heartfelt appreciation to Professor R.T. DeHoff, whose teaching techniques are second to none. It has been a privilege and a pleasure to have studied under his guidance. In this context I would like to quote a Sanskrit saying:

*ekamavaksharam yastu gurush-shishyam prabodhayet |
prithiviyam nasti tad-dravyam yad-dattva chanrni bhavet ||*
-subhAshitam
{Even if it be one syllable that the teacher imparts to the pupil, there exists not in this world, that wealth, with which to repay this debt."}

I would also like to thank Professor Holloway, for his generosity in allowing me to use his computing facilities as well as his coffee pot. I have been treated by the students of his group as one of their own, and I would like to thank them for that.

All of the computer simulations in this work were run on the departmental Apollo 10000 work-station (node: SILICA) under an account that Tom Swiler set up for me. I appreciate this, and recommend this in house computing facility to future students needing fast reliable computer output in their work.

It is not usual practice to thank one's family in the society where I grew up, but I have a family here in Washington D.C. (Atish and Meena Sanyal) who have risen above their calling to offer me support and affection.

Special thanks are due to Ms. Ann Wood Fuller for the crucial emotional support that she provided during the concluding stages of this ordeal.

If all the people that have provided support to me over the years were to be mentioned by name, this acknowledgement would read like a "Who's Who" of the city of Gainesville and could conceivably be longer than this manuscript. Therefore, I beg forgiveness from those not directly named, and extend my appreciation for them just the same.

Finally I thank Professor Reza Abbaschian and Professor Ellis D. Verink Jr. for their encouragement and support.

TABLE OF CONTENTS

	<u>page</u>
ACKNOWLEDGMENTS.....	(iv)
LIST OF TABLES.....	(viii)
LIST OF FIGURES.....	(ix)
ABSTRACT.....	(xviii)
 CHAPTERS	
1 INTRODUCTION.....	1
2 DIFFUSION STUDIES IN THE SOLID STATE	
-- A LITERATURE SURVEY.....	6
Fick's Phenomenological Laws of Diffusion.....	7
Analysis of Experimental Data Using Fick's Laws..	8
The Kirkendall Shift and Darken's Analysis.....	11
The Matano Interface.....	15
Difficulties in Applying Fickian Phenomenology to	
experiments.....	15
3 DIFFUSION STUDIES IN MULTICOMPONENT SYSTEMS.....	18
"Uphill" Diffusion in Ternary Systems.....	19
Theoretical Developments in Multi-component	
Diffusion.....	20
Experimental Work in Multi-component Systems....	22
New Strategies in Theoretical and Experimental	
Studies.....	24
4 EXPERIMENTALLY ACCESSIBLE REFERENCE SYSTEMS IN	
DIFFUSION.....	27
The Matano Interface.....	27
The Kirkendall Interface.....	35
Diffusion Coefficients Versus Jump Frequencies...	38
5 THE RELATIVE PENETRATION TENDENCY (RPT) MODEL....	40
Introduction.....	40
The Concept Illustrated With the 50-50 AB/BC	
Couple.....	42
Ternary Isomorphous Systems - Patterns of	
Behavior.....	47
Comparison With Experimental Data.....	55
Concluding Remarks.....	61

6	THE JUMP FREQUENCY APPROACH (JFA) IN DIFFUSION STUDIES.....	62
	Introduction.....	62
	Preliminary Development.....	63
	The Algorithm.....	66
	The Input.....	68
	The Setup.....	71
	The Simulation of Tracer Diffusion.....	71
	The Kirkendall Effect in Binary Isomorphous Diffusion.....	72
	Simulation of Diffusion in Ternary Isomorphous Systems.....	86
	"Uphill" Diffusion - Darken's Experiment.....	92
	Computer Modelling of Diffusion.....	97
	The JFA Versus the TFA.....	98
	The JFA Versus the RPT Modelling.....	99
	Concluding Remarks.....	101
7	DIFFUSION IN ISOMORPHOUS SYSTEMS	
	- A SURVEY USING THE JFA.....	102
	Introduction.....	102
	Case (A): All Γ 's Equal and Independent of Composition.....	110
	Cases (B), (C) and (D).....	115
	Concluding Comments.....	190
8	JFA MODELS FOR EXPERIMENTAL DATA IN ISOMORPHOUS SYSTEMS.....	191
	Introduction.....	191
	The Iron-Cobalt-Nickel System.....	192
	The Copper-Silver-Gold System.....	200
	The Copper-Nickel_Zinc System.....	206
	Discussion.....	214
9	JFA IN MULTI-PHASE SYSTEMS.....	218
	The Moving Phase Boundary Problem.....	218
	Planar Interface Migration in Binary Two-phase Systems.....	224
	The Binary Two-phase Case.....	227
	Growth of an Intermediate Phase During Diffusion.....	241
	Ternary and Higher Order Multi-phase Systems.....	264
	The Ideal Solution Model for Ternary Two-phase Fields.....	264
10	CONCLUSIONS AND RECOMMENDATIONS FOR FUTURE WORK..	269
	Conclusions.....	269
	Recommendations for Future Work.....	271

APPENDIX	COMPUTER SIMULATION PROGRAMS FOR DIFFUSION	
	USING THE JFA.....	276
REFERENCES.....		296
BIOGRAPHICAL SKETCH.....		300

LIST OF TABLES

Table 7.01: The composition of the Q-side, i.e., the right hand side of the semi-infinite diffusion couples surveyed, spanning the ternary isotherm in the system A-B-C. The P-side, i.e., the left hand side of all these couples is the 1/3-1/3-1/3 ternary alloy. For a graphical representation, see figure 7.01..... 104

Table 8.01: The end-point compositions of the alloys studied by Vignes and Sabatier in their work on diffusion in the Fe-Co-Ni system. These same compositions were used for the computer simulations for comparison with experiment.. 193

Table 8.02: The end-point compositions of the alloys studied by Ziebold and Ogilvie in their work on diffusion in the Cu-Ag-Au ternary system. These same compositions were used for the computer simulations for comparison with experiment.....201

Table 8.03: The end-point compositions of the alloys studied by Wan in his work on diffusion in the Cu-Ni-Zn ternary system. These same compositions were used for the computer simulations for comparison with the experiment.. 207

Table 9.01: The SIXTEEN combinations of the four jump frequencies (for each of the two components 'A' and 'B' in each of the two phases ' α ' and ' β ') that were used in the exploratory survey of interface migration in binary two-phase diffusion couples..... 231

Table 9.02: Computer generated values for the end-point compositions (in atom % of solute) below which η -phase will not form, for the phase diagram shown in figure 9.17. Both Γ_A and Γ_B in a given phase are set equal, so that there is no lattice motion. Twenty seven different combinations of the jump frequencies are used in the simulations, with Fast:Medium:Slow :: 10:5:1 ($\times 10^5$ jumps/sec)..... 254

Table 9.03: Computer generated values for the solubility limits in the terminal phases beyond which the intermediate phase will not form, in couples made of pure A and B {see figure 9.18}. The jump frequencies of A and B are set equal in any given phase, so that there is no lattice motion. 27 combinations of Γ 's were used in the simulations with Fast:Medium:Slow :: 10:5:1 ($\times 10^5$ jumps/sec)..... 258

Table 9.04: The values of the parabolic rate constants as a function of the two-phase field width. The first set of six cases are graphically depicted in figure 9.20 and the next six in figure 9.21..... 260

LIST OF FIGURES

Figure 5.01: The RPT model for an AB/BC ternary diffusion couple.....	43
Figure 5.02: Illustration of the composition path predicted by the RPT approach.....	48
Figure 5.03: Exploded Gibbs triangles depicting the composition paths for concentration independent relative penetration depths, with A:B:C::5:5:5 and 5:0:0.....	50
Figure 5.04: Exploded Gibbs triangles depicting the composition paths for concentration independent relative penetration depths, with A:B:C::5:5:0 and 5:3:0.....	51
Figure 5.05: Graphical representation of the dependence of the RPT's on composition and the composition paths for the case A:B:C::5:0:0.....	52
Figure 5.06: Exploded Gibbs triangles depicting the composition paths for concentration dependent relative penetration depths, with A:B:C::5:5:0 and 5:3:0.....	53
Figure 5.07: A comparison of Vignes and Sabatier's data on the Fe-Co-Ni system with Wan's RPT model.....	56
Figure 5.08: A comparison of Ziebold and Ogilvie's data on the Cu-Ag-Au system with Wan's RPT model.....	58
Figure 5.09: Wan's helical model for the RPT's in the Cu-Ni-Zn system.....	59
Figure 5.10: Comparison of Wan's experimental data with his helical RPT model.....	60
Figure 6.01: The redistribution of tracer atoms after a simulated diffusion anneal for 10000 seconds.....	73
Figure 6.02: Penetration profiles as a function of iterative steps in simulation, for a pure A-B couple, with $\Gamma_A = 10^7$ and $\Gamma_B = 10^6 \text{sec}^{-1}$	76
Figure 6.03: Penetration profiles as a function of iterative steps in simulation, for a pure A-B couple, with $\Gamma_A = 10^7$ and $\Gamma_B = 10^6 \text{sec}^{-1}$	77
Figure 6.04: Kirkendall shift patterns as a function of iterative steps in simulation, for a pure A-B couple, with $\Gamma_A = 10^7$ and $\Gamma_B = 10^6 \text{sec}^{-1}$	78

Figure 6.05: Kirkendall shift patterns as a function of iterative steps in simulation, for a pure A-B couple, with $\Gamma_A = 10^7$ and $\Gamma_B = 10^6 \text{sec}^{-1}$	79
Figure 6.06: Penetration profiles plotted against normalized distance axis for the same couple as figures 6.02, 6.03.....	81
Figure 6.07: Penetration profiles plotted against normalized distance axis for the same couple as figures 6.02, 6.03.....	82
Figure 6.08: A re-plot of figure 6.04, except that both axes are normalized with respect to time.....	84
Figure 6.09: A re-plot of figure 6.05, except that both axes are normalized with respect to time.....	85
Figure 6.10: Concentration-penetration profiles obtained by computer simulation of diffusion in a AB-BC couple..	88
Figure 6.11: Kirkendall shift profile for AB-BC couple	89
Figure 6.12: The composition path in the AB-BC couple	91
Figure 6.13: Illustration of the shift in the 'cross-over' point due to the concentration dependence of the jump frequencies.....	93
Figure 6.14: Jump frequency model for the "uphill" diffusion of carbon in steel containing silicon.....	96
Figure 6.15: An example of the computer modelling of quaternary isomorphous diffusion.....	100
Figure 7.01: The ternary isotherm divided into eight for the purpose of surveying isomorphous diffusion behavior via computer simulation.....	103
Figure 7.02: Illustration of the composition dependence of the jump frequencies in the ternary isomorphous system A-B-C, for the case where $\Gamma_A:\Gamma_B:\Gamma_C:\text{Fast}::\text{Slow}:\text{Slow}$	107
Figure 7.03: Illustration of the composition dependence of the jump frequencies in the ternary isomorphous system A-B-C, for the case where $\Gamma_A:\Gamma_B:\Gamma_C:\text{Fast}::\text{Fast}:\text{Slow}$	108
Figure 7.04: Illustration of the composition dependence of the jump frequencies in the ternary isomorphous system A-B-C, for the case where $\Gamma_A:\Gamma_B:\Gamma_C:\text{Fast}::\text{Medium}:\text{Slow}$	109

Figure 7.05: The composition paths of the 18 couples simulated, with the Γ 's of A, B and C identical..... 111

Figure 7.06: The concentration penetration profiles for couples # 1-6 for the case where the Γ 's are identical.. 112

Figure 7.07: The concentration penetration profiles for couples # 7-12 for the case where the Γ 's are identical. 113

Figure 7.08: The concentration penetration profiles for couples # 13-18 for the case where the Γ 's are identical 114

Figure 7.09: The composition paths of the 18 couples simulated, for the case where the Γ 's are concentration independent and are in the ratio A:B:C::Fast:Fast:Slow.. 116

Figure 7.10: The composition paths of the 18 couples simulated, for the case where the Γ 's are dependent on concentration and are in the ratio A:B:C::Fast:Fast:Slow 118

Figure 7.11: The composition paths of the 18 couples simulated, for the case where the Γ 's are concentration independent and are in the ratio A:B:C::Fast:Slow:Slow.. 119

Figure 7.12: The composition paths of the 18 couples simulated, for the case where the Γ 's are dependent on concentration and are in the ratio A:B:C::Fast:Slow:Slow 120

Figure 7.13: The composition paths of the 18 couples simulated, for the case where the Γ 's are concentration independent and are in the ratio A:B:C::Fast:Medium:Slow 122

Figure 7.14: The composition paths of the 18 couples simulated, for the case where the Γ 's are concentration dependent and are in the ratio A:B:C::Fast:Medium:Slow.. 123

Figure 7.15: Concentration penetration and Kirkendall shift pattern for couple #01 [$\Gamma_A:\Gamma_B:\Gamma_C$::Fast:Fast:Slow].. 125

Figure 7.16: Concentration penetration and Kirkendall shift pattern for couple #01 [$\Gamma_A:\Gamma_B:\Gamma_C$::Fast:Slow:Slow].. 126

Figure 7.17: Concentration penetration and Kirkendall shift pattern for couple #01 [$\Gamma_A:\Gamma_B:\Gamma_C$::Fast:Medium:Slow]. 127

Figure 7.18: Concentration penetration and Kirkendall shift pattern for couple #02 [$\Gamma_A:\Gamma_B:\Gamma_C$::Fast:Fast:Slow].. 129

Figure 7.19: Concentration penetration and Kirkendall shift pattern for couple #02 [$\Gamma_A:\Gamma_B:\Gamma_C$::Fast:Slow:Slow].. 130

Figure 7.20: Concentration penetration and Kirkendall shift pattern for couple #02 [$\Gamma_A:\Gamma_B:\Gamma_C::$ Fast:Medium:Slow]..	131
Figure 7.21: Concentration penetration and Kirkendall shift pattern for couple #03 [$\Gamma_A:\Gamma_B:\Gamma_C::$ Fast:Fast:Slow]...	132
Figure 7.22: Concentration penetration and Kirkendall shift pattern for couple #03 [$\Gamma_A:\Gamma_B:\Gamma_C::$ Fast:Slow:Slow]...	133
Figure 7.23: Concentration penetration and Kirkendall shift pattern for couple #03 [$\Gamma_A:\Gamma_B:\Gamma_C::$ Fast:Medium:Slow]..	134
Figure 7.24: Concentration penetration and Kirkendall shift pattern for couple #04 [$\Gamma_A:\Gamma_B:\Gamma_C::$ Fast:Fast:Slow]...	136
Figure 7.25: Concentration penetration and Kirkendall shift pattern for couple #04 [$\Gamma_A:\Gamma_B:\Gamma_C::$ Fast:Slow:Slow]...	137
Figure 7.26: Concentration penetration and Kirkendall shift pattern for couple #04 [$\Gamma_A:\Gamma_B:\Gamma_C::$ Fast:Medium:Slow]..	138
Figure 7.27: Concentration penetration and Kirkendall shift pattern for couple #05 [$\Gamma_A:\Gamma_B:\Gamma_C::$ Fast:Fast:Slow]...	139
Figure 7.28: Concentration penetration and Kirkendall shift pattern for couple #05 [$\Gamma_A:\Gamma_B:\Gamma_C::$ Fast:Slow:Slow]...	140
Figure 7.29: Concentration penetration and Kirkendall shift pattern for couple #05 [$\Gamma_A:\Gamma_B:\Gamma_C::$ Fast:Medium:Slow]..	141
Figure 7.30: Concentration penetration and Kirkendall shift pattern for couple #06 [$\Gamma_A:\Gamma_B:\Gamma_C::$ Fast:Fast:Slow]...	142
Figure 7.31: Concentration penetration and Kirkendall shift pattern for couple #06 [$\Gamma_A:\Gamma_B:\Gamma_C::$ Fast:Slow:Slow]...	143
Figure 7.32: Concentration penetration and Kirkendall shift pattern for couple #06 [$\Gamma_A:\Gamma_B:\Gamma_C::$ Fast:Medium:Slow]..	144
Figure 7.33: Concentration penetration and Kirkendall shift pattern for couple #07 [$\Gamma_A:\Gamma_B:\Gamma_C::$ Fast:Fast:Slow]...	146
Figure 7.34: Concentration penetration and Kirkendall shift pattern for couple #07 [$\Gamma_A:\Gamma_B:\Gamma_C::$ Fast:Slow:Slow]...	147
Figure 7.35: Concentration penetration and Kirkendall shift pattern for couple #07 [$\Gamma_A:\Gamma_B:\Gamma_C::$ Fast:Medium:Slow]..	148
Figure 7.36: Concentration penetration and Kirkendall shift pattern for couple #08 [$\Gamma_A:\Gamma_B:\Gamma_C::$ Fast:Fast:Slow]...	149

Figure 7.37: Concentration penetration and Kirkendall shift pattern for couple #08 $[\Gamma_A:\Gamma_B:\Gamma_C::\text{Fast:Slow:Slow}] \dots$	150
Figure 7.38: Concentration penetration and Kirkendall shift pattern for couple #08 $[\Gamma_A:\Gamma_B:\Gamma_C::\text{Fast:Medium:Slow}] \dots$	151
Figure 7.39: Concentration penetration and Kirkendall shift pattern for couple #09 $[\Gamma_A:\Gamma_B:\Gamma_C::\text{Fast:Fast:Slow}] \dots$	152
Figure 7.40: Concentration penetration and Kirkendall shift pattern for couple #09 $[\Gamma_A:\Gamma_B:\Gamma_C::\text{Fast:Slow:Slow}] \dots$	153
Figure 7.41: Concentration penetration and Kirkendall shift pattern for couple #09 $[\Gamma_A:\Gamma_B:\Gamma_C::\text{Fast:Medium:Slow}] \dots$	154
Figure 7.42: Concentration penetration and Kirkendall shift pattern for couple #10 $[\Gamma_A:\Gamma_B:\Gamma_C::\text{Fast:Fast:Slow}] \dots$	155
Figure 7.43: Concentration penetration and Kirkendall shift pattern for couple #10 $[\Gamma_A:\Gamma_B:\Gamma_C::\text{Fast:Slow:Slow}] \dots$	156
Figure 7.44: Concentration penetration and Kirkendall shift pattern for couple #10 $[\Gamma_A:\Gamma_B:\Gamma_C::\text{Fast:Medium:Slow}] \dots$	157
Figure 7.45: Concentration penetration and Kirkendall shift pattern for couple #11 $[\Gamma_A:\Gamma_B:\Gamma_C::\text{Fast:Fast:Slow}] \dots$	158
Figure 7.46: Concentration penetration and Kirkendall shift pattern for couple #11 $[\Gamma_A:\Gamma_B:\Gamma_C::\text{Fast:Slow:Slow}] \dots$	159
Figure 7.47: Concentration penetration and Kirkendall shift pattern for couple #11 $[\Gamma_A:\Gamma_B:\Gamma_C::\text{Fast:Medium:Slow}] \dots$	160
Figure 7.48: Concentration penetration and Kirkendall shift pattern for couple #12 $[\Gamma_A:\Gamma_B:\Gamma_C::\text{Fast:Fast:Slow}] \dots$	161
Figure 7.49: Concentration penetration and Kirkendall shift pattern for couple #12 $[\Gamma_A:\Gamma_B:\Gamma_C::\text{Fast:Slow:Slow}] \dots$	162
Figure 7.50: Concentration penetration and Kirkendall shift pattern for couple #12 $[\Gamma_A:\Gamma_B:\Gamma_C::\text{Fast:Medium:Slow}] \dots$	163
Figure 7.51: Concentration penetration and Kirkendall shift pattern for couple #13 $[\Gamma_A:\Gamma_B:\Gamma_C::\text{Fast:Fast:Slow}] \dots$	164
Figure 7.52: Concentration penetration and Kirkendall shift pattern for couple #13 $[\Gamma_A:\Gamma_B:\Gamma_C::\text{Fast:Slow:Slow}] \dots$	165
Figure 7.53: Concentration penetration and Kirkendall shift pattern for couple #13 $[\Gamma_A:\Gamma_B:\Gamma_C::\text{Fast:Medium:Slow}] \dots$	166

Figure 7.54: Concentration penetration and Kirkendall shift pattern for couple #14 $[\Gamma_A:\Gamma_B:\Gamma_C::\text{Fast}:\text{Fast}:\text{Slow}] \dots$	168
Figure 7.55: Concentration penetration and Kirkendall shift pattern for couple #14 $[\Gamma_A:\Gamma_B:\Gamma_C::\text{Fast}:\text{Slow}:\text{Slow}] \dots$	169
Figure 7.56: Concentration penetration and Kirkendall shift pattern for couple #14 $[\Gamma_A:\Gamma_B:\Gamma_C::\text{Fast}:\text{Medium}:\text{Slow}] \dots$	170
Figure 7.57: Concentration penetration and Kirkendall shift pattern for couple #15 $[\Gamma_A:\Gamma_B:\Gamma_C::\text{Fast}:\text{Fast}:\text{Slow}] \dots$	171
Figure 7.58: Concentration penetration and Kirkendall shift pattern for couple #15 $[\Gamma_A:\Gamma_B:\Gamma_C::\text{Fast}:\text{Slow}:\text{Slow}] \dots$	172
Figure 7.59: Concentration penetration and Kirkendall shift pattern for couple #15 $[\Gamma_A:\Gamma_B:\Gamma_C::\text{Fast}:\text{Medium}:\text{Slow}] \dots$	173
Figure 7.60: Concentration penetration and Kirkendall shift pattern for couple #16 $[\Gamma_A:\Gamma_B:\Gamma_C::\text{Fast}:\text{Fast}:\text{Slow}] \dots$	174
Figure 7.61: Concentration penetration and Kirkendall shift pattern for couple #16 $[\Gamma_A:\Gamma_B:\Gamma_C::\text{Fast}:\text{Slow}:\text{Slow}] \dots$	175
Figure 7.62: Concentration penetration and Kirkendall shift pattern for couple #16 $[\Gamma_A:\Gamma_B:\Gamma_C::\text{Fast}:\text{Medium}:\text{Slow}] \dots$	176
Figure 7.63: Concentration penetration and Kirkendall shift pattern for couple #17 $[\Gamma_A:\Gamma_B:\Gamma_C::\text{Fast}:\text{Fast}:\text{Slow}] \dots$	177
Figure 7.64: Concentration penetration and Kirkendall shift pattern for couple #17 $[\Gamma_A:\Gamma_B:\Gamma_C::\text{Fast}:\text{Slow}:\text{Slow}] \dots$	178
Figure 7.65: Concentration penetration and Kirkendall shift pattern for couple #17 $[\Gamma_A:\Gamma_B:\Gamma_C::\text{Fast}:\text{Medium}:\text{Slow}] \dots$	179
Figure 7.66: Concentration penetration and Kirkendall shift pattern for couple #18 $[\Gamma_A:\Gamma_B:\Gamma_C::\text{Fast}:\text{Fast}:\text{Slow}] \dots$	180
Figure 7.67: Concentration penetration and Kirkendall shift pattern for couple #18 $[\Gamma_A:\Gamma_B:\Gamma_C::\text{Fast}:\text{Slow}:\text{Slow}] \dots$	181
Figure 7.68: Concentration penetration and Kirkendall shift pattern for couple #18 $[\Gamma_A:\Gamma_B:\Gamma_C::\text{Fast}:\text{Medium}:\text{Slow}] \dots$	182
Figure 7.69: A survey of the change in Kirkendall shift patterns as a function of end-point composition for the 18 couples simulated. {concentration independent Γ 's in the ratio A:B:C::Fast:Fast:Slow}	184

Figure 7.70: A survey of the change in Kirkendall shift patterns as a function of end-point composition for the 18 couples simulated. {concentration dependent Γ 's in the ratio A:B:C::Fast:Fast:Slow}.....	185
Figure 7.71: A survey of the change in Kirkendall shift patterns as a function of end-point composition for the 18 couples simulated. {concentration independent Γ 's in the ratio A:B:C::Fast:Slow:Slow}.....	186
Figure 7.72: A survey of the change in Kirkendall shift patterns as a function of end-point composition for the 18 couples simulated. {concentration dependent Γ 's in the ratio A:B:C::Fast:Slow:Slow}.....	187
Figure 7.73: A survey of the change in Kirkendall shift patterns as a function of end-point composition for the 18 couples simulated. {concentration independent Γ 's in the ratio A:B:C::Fast:Medium:Slow}.....	188
Figure 7.74: A survey of the change in Kirkendall shift patterns as a function of end-point composition for the 18 couples simulated. {concentration dependent Γ 's in the ratio A:B:C::Fast:Medium:Slow}.....	189
Figure 8.01: Composition dependence of jump frequencies in the Fe-Co-Ni system.....	195
Figure 8.02: A comparison of composition paths obtained experimentally by Vignes and Sabatier with those generated by simulation.....	196
Figure 8.03: A comparison between computed and experimentally measured concentration penetration profiles for couple # 13 in the Fe-Co-Ni system.....	197
Figure 8.04: An example of Kirkendall shift and the concentration profiles in the Fe-Co-Ni system (couple #12) generated by computer simulation.....	199
Figure 8.05: The model used for the concentration dependence of the Γ 's in the Cu-Ag-Au system to simulate diffusion in the couples studied by Ziebold and Ogilvie...	202
Figure 8.06: A comparison of the composition paths obtained experimentally by Ziebold and Ogilvie on the right, with the paths computed by simulation.....	204
Figure 8.07: An example of the Kirkendall shift and the concentration profiles in the Cu-Ag-Au system (couple #5), generated by computer simulation.....	205

Figure 8.08: The model used for concentration dependence of jump frequencies for simulating wan's experiments in the Cu-Ni-Zn system.....	208
Figure 8.09: A comparison of the composition paths in the Cu-Ni-Zn system studied by Wan, for couples # 1-3, with the computed path according to the jump frequency model presented in figure 8.08.....	210
Figure 8.10: A comparison of the composition paths in the Cu-Ni-Zn system studied by Wan, for couples # 4-6, with the computed path according to the jump frequency model presented in figure 8.08.....	211
Figure 8.11: A comparison of the composition paths in the Cu-Ni-Zn system studied by Wan, for couples # 7-11, with the computed path according to the jump frequency model presented in figure 8.08.....	212
Figure 8.12: An example of the Kirkendall shift and the concentration profiles (couple #9) in the Cu-Ni-Zn system generated by computer simulation.....	213
Figure 8.13: A comparison of measured Kirkendall shifts and those predicted by computer simulations in the Cu-Ni-Zn system.....	215
Figure 9.01: An illustration of the variability in binary two-phase diffusion couples, introduced as a consequence of the shape of the phase diagram and the end-point compositions chosen.....	226
Figure 9.02: The first of the three phase diagrams explored in the simulation of planar phase boundary migration during diffusion in binary two-phase systems....	228
Figure 9.03: The second of the three phase diagrams explored in the simulation of planar phase boundary migration during diffusion in binary two-phase systems....	229
Figure 9.04: The last of the three phase diagrams explored in the simulation of planar phase boundary migration during diffusion in binary two-phase systems....	230
Figure 9.05: The concentration profiles for the 16 combinations of Γ 's considered, for phase diagram I.....	233
Figure 9.06: The concentration profiles for the 16 combinations of Γ 's considered, for phase diagram II.....	234

Figure 9.07: The concentration profiles for the 16 combinations of Γ 's considered, for phase diagram III.....	235
Figure 9.08: The Kirkendall shift profiles for the 16 combinations of Γ 's considered, for phase diagram I.....	237
Figure 9.09: The Kirkendall shift profiles for the 16 combinations of Γ 's considered, for phase diagram II.....	238
Figure 9.10: The Kirkendall shift profiles for the 16 combinations of Γ 's considered, for phase diagram III.....	239
Figure 9.11: The interface shift patterns for the 16 combinations of Γ 's considered, for phase diagram III.....	242
Figure 9.12: The interface shift patterns for the 16 combinations of Γ 's considered, for phase diagram III.....	243
Figure 9.13: The interface shift patterns for the 16 combinations of Γ 's considered, for phase diagram III.....	244
Figure 9.14: Phase diagram employed to illustrate diffusion-induced formation and growth of the η -phase.....	245
Figure 9.15: The concentration profiles in a binary three-phase system, for a typical couple in which the intermediate phase (η) forms and grows during diffusion...	249
Figure 9.16: The lattice velocity (Kirkendall shift) profile for the couple shown in figure 9.15.....	250
Figure 9.17: The interphase interface shifts and the consequent growth of the η -phase plotted against $t^{1/2}$	251
Figure 9.18: Phase diagram used to generate Table 9.02..	252
Figure 9.19: Phase diagram used to generate Table 9.03..	256
Figure 9.20: The phase diagram used to study the effect of the two-phase field width on the parabolic rate constant for the growth of the intermediate phase.....	259
Figure 9.21: The parabolic rate constants plotted as a function of the two-phase field width.....	261
Figure 9.22: The parabolic rate constants plotted as a function of the η - β field width (for a fixed α - η field)...	263
Figure 9.23: An ideal solution model for the bundle of tie-lines in a ternary two-phase field.....	267

Abstract of Dissertation Presented to the Graduate School
of the University of Florida in Partial Fulfillment of the
Requirements for the Degree of Doctor of Philosophy

MODELLING OF MULTICOMPONENT MULTIPHASE DIFFUSION IN
CONDENSED CRYSTALLINE SYSTEMS USING ATOM JUMP FREQUENCIES

By

Coimbatore Vennkateswaran Iswaran

December 1993

Chairman: Robert T. DeHoff

Major Department: Materials Science & Engineering

The work presented here offers a novel approach to the study of diffusion in crystalline systems. Emphasis is placed on the intrinsic behavior of atoms that diffuse via a vacancy-atom interchange mechanism. The kinetic descriptors are the "effective mean jump frequencies" of these atoms, rather than diffusion coefficients. Each atomic species is characterized by these jump frequencies, which may vary with the composition of the volume element in which the jumps take place. Based on a reformulation of Fick's first law, computer models have been created to allow the simulation of various diffusion problems. The output of these programs consist of the concentration penetration profiles (and hence the composition paths in ternary and higher order systems), the Kirkendall shift patterns (and hence the lattice

velocity profiles) and, if applicable, the migration rate of planar phase boundaries (and hence the point defect generation/annihilation rate at these boundaries).

Starting with the simple case of tracer diffusion and progressively increasing the complexity of the system, the efficacy of the jump frequency approach (JFA) has been demonstrated. The problem of "uphill" diffusion of carbon in steels containing a substitutional element has been successfully modelled using the JFA.

A systematic survey of ternary isomorphous diffusion was undertaken and the results compared with previously published work based on the relative penetration tendency viewpoint. Published experimental work in the Fe-Co-Ni system, the Cu-Ag-Au system and the Cu-Ni-Zn system were reanalyzed using the JFA, and reasonable agreement demonstrated.

The problem of planar phase boundary migration in binary two-phase systems was addressed. A number of simulations were run to make a systematic evaluation of the effect of kinetic (jump frequencies), thermodynamic (phase diagram variables) and experimental (end-point compositions of the semi-infinite couples) input variables on the diffusion behavior of the system. The results of these simulations are presented and discussed.

Finally, the formation and growth of an intermediate phase during diffusion in binary three-phase systems was successfully simulated. The effect of input parameters on the growth rate was investigated and these results are also presented and discussed.

CHAPTER 1 INTRODUCTION

Kinetics of processes driven by thermodynamic forces have a profound and pivotal significance in the design and processing of materials. The advent of modern materials with novel strengthening mechanisms (multicomponent systems, mechanical alloys, dispersion strengthening, reinforced composites etc.) in conjunction with harsher operating conditions (e.g., higher temperatures) have created an accompanying need for controlling the kinetics of processes that would otherwise lead to an untimely degradation of the material properties stipulated by the design criteria.

Diffusion is often the slowest step in transformations requiring atom flows, especially in condensed crystalline systems, and is therefore the critical step in the kinetics. This fact has spurred a wealth of diffusion studies, both in the theoretical and experimental realms. The foundation of the majority of these studies has been the phenomenology developed by Adolph Fick¹ that relates fluxes to gradients in concentration and accumulations to the divergence of these fluxes. These efforts are briefly reviewed in the next two chapters (chapters 2 and 3).

In crystalline materials, in addition to the constraints imposed by the solid state, the requirement of maintaining a crystal lattice precludes an otherwise simpler description of the atom flows. In these cases, the choice of a reference frame, with respect to which the atom motions are defined, is a non-trivial problem. On the one hand, the atom movements are in direct response to the immediate environs encountered by these atoms, and on the other, these environs are continuously shifting and readjusting with respect to the outside world. Commonly accepted simplifying assumptions that make the study of diffusion tractable are subject to questions regarding the conditions under which they hold true. One such relatively well established concept is that of the Matano interface. Chapter 4 highlights the Matano interface and the resultant Boltzman-Matano analysis^{2,3} of experimental diffusion data with a view to pointing out some difficulties associated with it.

Zeroing in on the more fundamental aspects of atom movements, namely their *intrinsic fluxes and flows*, DeHoff and his co-workers^{4,5} developed what they call the relative penetration tendency (RPT) or the linear approximation approach (LAA). Their work represents a radical departure from the traditional Fickian analysis (TFA) and is a precursor to the development of the jump frequency approach (JFA), which is presented in this dissertation. Their analysis is reviewed in detail in chapter 5.

A fundamental feature of diffusion in substitutional alloy systems is the atom-vacancy interchange. Associated with these events is a *characteristic effective mean jump frequency* of the atom exchanging places with the point defect. In this work, a methodology for analyzing patterns of behavior in diffusion processes has been developed, which is based on introducing these jump frequencies as the kinetic descriptors that are analogous to the more traditional diffusion coefficients. Chapter 6 introduces and develops this concept in some detail. The design of computer simulation programs based on the JFA is described. Finally, the efficacy of the technique is demonstrated with the help of some selected examples.

In the next chapter (chapter 7), diffusion in ternary isomorphous systems is surveyed across the ternary isotherm using the computer simulations that invoke the JFA. Computer simulations using the JFA were carried out on the couples studied by DeHoff et al.⁵ The results are compared to those obtained by them for the RPT viewpoint. This chapter also introduces the concept of the concentration dependence of the jump frequencies and its effect on the composition paths.

The measure of success of any theoretical construct lies in its ability to predict experimental results. The results presented in three classic studies, that of Vignes and Sabatier⁶ in the Fe-Co-Ni system, of Ziebold and Ogilvie⁷ in the Cu-Ag-Au system and of Wan⁸ in the Cu-Ni-Zn system, are

reanalyzed in chapter 8 using the JFA. Satisfactory agreement between the computer simulations and the experimental diffusion paths is demonstrated.

One of the problems that has provided much of the intrigue in diffusion studies is that of phase boundary migration due to diffusion. In chapter 9, a theoretical basis is developed for the case of *planar interphase interface migration* in multi-component multi-phase systems. We start with the relatively simple case of binary-two-phase systems, with the end-point compositions of semi-infinite diffusion couples in the terminal one phase fields and with the interface equilibrium compositions dictated by the tie-line belonging to the temperature of the diffusion anneal. This is followed by the consideration of the formation and growth of an intermediate phase due to diffusion in binary three-phase systems. The bulk of this chapter consists of computer outputs of *exploratory (rather than comprehensive) surveys of patterns of behavior*. Emphasis is placed on the fact that the work presented in this dissertation *sets up a forum* in which questions (not necessarily yet asked) pertaining to specific diffusion problems are put in the appropriate format so that the JFA simulations can provide the answer. The difficulties encountered, as of the present time, in extending this approach to systems with three or more components are discussed toward the end of the chapter.

A summary of the conclusions drawn from this work is presented in chapter 10. This chapter recommends ways to resolve some legitimate concerns regarding the jump frequency approach that may be voiced at this writing. Recommendations for future work using the JFA in modelling diffusion phenomena are also made. The possibility of using the computer simulations based on the JFA as a teaching tool in undergraduate and graduate level courses in materials science is pursued. Advantage can and should be taken of a whole new vista that opens up because of the power and versatility of the jump frequency approach whose viability has been demonstrated in this dissertation.

CHAPTER 2

DIFFUSION STUDIES IN THE SOLID STATE--A LITERATURE SURVEY

The concept of representing flows in the presence of nonconservative forces due to gradients dates back 1822 to the work of Fourier.^{9,10} Fourier was concerned with developing a theory of heat flow at a time when the mathematical concepts of gradients and divergences were still at a stage of infancy. Indeed, Fourier's contribution to mathematics is as well recognized as his role as a physicist. The basic notion is simple and involves the phenomenological assertion that the flow is proportional to the driving force and that the proportionality constant is the mobility of whatever is flowing. For instance, in the case of heat conduction, the heat flux is proportional to the temperature gradient (which is the driving force), the proportionality constant being the thermal conductivity of the medium. Similarly, in the case of Ohm's law for electric current flow, the flow is proportional to the electromotive force (or the potential gradient) with the electrical conductivity as the proportionality constant.

Fick's Phenomenological Laws of Diffusion

Spurred by the success of these ideas, Adolf Fick¹ suggested a similar equation for mass flow during diffusion. The following equation, presented here for one-dimensional flow, known as Fick's First Law, has formed the basis for the bulk of diffusion studies in the literature.

$$J = -D \frac{\partial C}{\partial x} \quad (2.01)$$

where 'J' is the flux of atoms across a given plane,
 'C' is the concentration of atoms in that plane,
 is the gradient of that concentration,
 and 'D' is the diffusion coefficient.

The reason for the negative sign is that the direction of the flux is opposite that of the concentration gradient. Usually, the flux, J, has units of moles/unit area and the concentration is in moles per unit volume. From a units analysis it can be seen that D has units of [length]²/[time], usually cm²/sec.

In general, any extensive property of a thermodynamic system (mass, energy etc.) can be defined as an intensive quantity at a given point, which, when integrated over the volume of the system, yields the value of the extensive property,¹¹ i.e.,

$$Z = \int_V Z_v dV \quad (2.02)$$

where Z_v is the thermodynamic property in question. The time variation of Z in a given volume element inside the system has two contributing factors, (a) the net flow of Z into or out of the element, which is the divergence of J_z and (b) the production or destruction of Z in that element, $q(Z)$. Thus, for a given volume element, one can write

$$\frac{\partial Z_v}{\partial t} = -\text{div} J_z + q(Z) \quad (2.03)$$

Since the mass of the system is conserved, if Z refers to the mass, then the quantity $q(Z)$ disappears and in one dimension,

$$\frac{\partial C}{\partial t} = -\frac{\partial J}{\partial x} \quad (2.04)$$

Combining equations 2.01 and 2.02,

$$\frac{\partial C}{\partial t} = \frac{\partial}{\partial x} (D \frac{\partial C}{\partial x}) \quad (2.05)$$

This is Fick's Second Law.

Solutions for equation 2.05 yield the concentration profile patterns during diffusion. These solutions have been worked out for various initial and boundary conditions^{2,3,12-16}.

Analysis of Experimental Data Using Fick's Laws

The key quantity of interest in this analysis is the diffusion coefficient D , which can be extracted from

experimentally measured concentration-penetration profiles as follows. First, note that the equation 2.05 simplifies to

$$\frac{\partial C}{\partial t} = D \frac{\partial^2 C}{\partial x^2} \quad (2.06)$$

if 'D' is constant, i.e., independent of position and concentration. However, this situation is somewhat unrealistic, and hence one has to resort to an analysis developed by Boltzmann and Matano.^{2,3} Use the variable transformation

$$\lambda = \frac{x}{\sqrt{t}} \quad (2.07)$$

so that

$$\frac{\partial \lambda}{\partial x} = \frac{1}{\sqrt{t}}; \quad \frac{\partial \lambda}{\partial t} = -\frac{\lambda}{2t} \quad (2.08)$$

With this variable transformation, equation 2.05 becomes

$$-\frac{\lambda}{2} \frac{dC}{d\lambda} = \frac{d}{d\lambda} \left(D \frac{dC}{d\lambda} \right) \quad (2.09)$$

These are total derivatives since the time dependence has been eliminated. Integrating from one terminal composition C^- to a variable concentration C , and recognizing that the derivative evaluated at C^- is zero, we get

$$-\frac{1}{2} \int_{C^-}^C \lambda dC = D \left[\frac{dC}{d\lambda} \right]_{C^-}^C \quad (2.10)$$

For a given 't', equation 2.09 can be written as

$$D(C) = \frac{1}{2t} \cdot \left[\frac{dC}{dx} \right]_{c^-}^c \cdot \int_{c^-}^c x dC \quad (2.08)$$

By taking the slope of the experimentally measured C-x curve, as well as the required integral in the LHS of equation 2.11, with both quantities normally evaluated by curve-fitting, one can obtain 'D' as a function of concentration.

There are several points of interest in the above development. To begin with, the exact mechanism by which diffusion takes place is irrelevant to this analysis, since both equation 2.01 and 2.05 are phenomenological in nature. Second, the diffusion coefficient that is experimentally obtained is only valid at the concentration in question, and this concentration is not set *a priori* by the experimenter. This is not a problem in binary systems, where the entire range of compositions is guaranteed to fall between the terminal compositions and therefore one can obtain D as a continuous function of C in this composition range. In ternary systems, the values of D can only be evaluated at the points of intersection of two different diffusion couples, as explained later. In the study of systems with four or more elements, this restriction becomes a major stumbling block.

Third, and perhaps most important is the fact that the diffusion coefficient 'D' is not assigned to any particular atomic species. In the case of heat conduction, there is only one diffusing entity, but in substitutional alloy systems, this is not so. In consequence, except in the simplest of

cases, the so-called interdiffusion coefficient remains only remotely related to the actual vigor with which the two (or more) species intrinsically diffuse in response to the concentration gradient.

While Fick's laws successfully tackled the problem of diffusion in binary substitutional alloys, for higher order systems, one obtains a matrix of diffusion coefficients (this matrix is 1×1 in the binary case) whose physical meaning is often abstruse. This is not to say that attempts were not made to relate the "mechanism of diffusion" to the "diffusion coefficients." These are addressed below.

The Kirkendall Shift and Darken's Analysis

Smigelskas and Kirkendall,¹⁷ in a study of the Cu-Zn system, had installed inert markers at the original weld interface between the two terminal alloys. They reported, and this phenomenon was confirmed by Correa da Silva and Mehl,¹⁸ that the markers moved into the zinc-rich part of the couple. The marker movement suggested that Zn diffuses faster than copper and argued in favor of a vacancy-atom interchange mechanism for diffusion. Darken¹⁹ studied the phenomenon in some detail and was able to conclude that the "intrinsic" rates of diffusion of copper and zinc were not the same, and that as a result more zinc flows across the marker plane than copper in the other direction, thus causing the markers to move into the zinc rich region. Baluffi²⁰ has provided a

refinement of this analysis in which the possibility of the molar volume changing with concentration is rigorously taken into account.

It is Darken's analysis that provided the impetus for recognizing the differences between the various reference frames with respect to which the diffusion rates are measured.¹² Things that are not obvious from measurements in the laboratory frame are revealed by a different choice of reference frames. For example, the process as viewed by a genie sitting on a lattice site would be quite different from what is perceived in the laboratory frame. In this lattice reference frame, the form of Fick's laws remains the same, but the fluxes as well as the diffusion coefficients are intrinsic to the atomic species in question. These fluxes can and have been related to the so-called interdiffusion flux (note that there is only one such flux in the binary case), and the interdiffusion coefficient can also be written as a linear combination of the intrinsic diffusion coefficients.

One point that must be made clear at this juncture is that the lattice constantly and continuously readjusts to compensate for imbalances in the intrinsic flows, so that every plane in the diffusion zone (and not just the marker plane) is moving with a velocity, $\dot{\phi}(x)$ with respect to the laboratory frame, which is visualized as one corner of the room where the diffusion experiments are carried out. This fact is a pivotal point in the analysis of diffusion using the

jump frequency approach and will be expanded upon later. The lattice velocity ω , in the laboratory frame relates the intrinsic diffusion fluxes to the interdiffusion fluxes, designated by bold lettering, as follows.

$$\mathcal{J}_k = \mathbf{J}_k + c_k \cdot \omega = -D_k \frac{\partial C_k}{\partial x} + C_k \cdot \omega \quad (2.12)$$

where,

\mathbf{J}_k is the interdiffusion flux (i.e., with respect to the laboratory frame),

J_k , the intrinsic flux (i.e., wrt the lattice),

C_k , the concentration and D_k , the interdiffusion coefficient, of the atomic species 'k'.

In the binary case, subject to certain restrictive but reasonable assumptions discussed in greater detail in chapter 9, $\mathbf{J}_1 = -\mathbf{J}_2$, and $C_1 + C_2 = C$ (a constant), so that

$$\frac{\partial C_1}{\partial x} = -\frac{\partial C_2}{\partial x} \quad (2.13)$$

' ω ' can now be expressed as

$$\omega = \frac{1}{C} \cdot (D_1 - D_2) \cdot \frac{\partial C_1}{\partial x} = (D_1 - D_2) \cdot \frac{\partial X_1}{\partial x} \quad (2.14)$$

where X_k , is the atom fraction of species 'k'.

Comparing equation 2.12 for $k = 1, 2$ and inserting the conditions in equation 2.14 yields, for $k = 1$ e.g.,

$$\mathcal{J}_1 = -D_1 \frac{\partial C_1}{\partial x} + C_1 (D_1 - D_2) \frac{\partial X_1}{\partial x} \quad (2.15)$$

Multiply and divide throughout by 'C' to obtain,

$$\begin{aligned}
 & \text{and} \\
 J_1 &= -(X_2 D_1 + X_1 D_2) \cdot \frac{\partial C_1}{\partial x} \\
 J_2 &= -(X_1 D_2 + X_2 D_1) \cdot \frac{\partial C_2}{\partial x} \quad (2.16)
 \end{aligned}$$

We can define an interdiffusion coefficient, D , as

$$D = (X_1 D_2 + X_2 D_1) \quad (2.17)$$

Then equation 2.16 each simplifies to

$$J_k = -D \cdot \frac{\partial C_k}{\partial x} \dots [k = 1, 2] \quad (2.18)$$

Equation 2.18 vividly demonstrates the dilemma that arises when one tries to reconcile the continuum approach of the phenomenological theory with the atomistic approach that attempts to divine the mechanism of the process. Take, for instance, the simplest case represented by equation 2.18. This would be when the interdiffusion coefficient is constant (concentration independent). However, for this to happen, the two intrinsic diffusivities have to be concentration dependent in a peculiar way, so as to satisfy the requirements of equation 2.18!

In addition to the above development, Darken also demonstrated that the intrinsic diffusivity was related to the tracer diffusivity (an experimentally measurable entity), under conditions where the tracer atom concentration approaches zero, through the activity coefficient and the atom fraction of the species in question.

$$D_k = D_k^* \left(1 + \frac{\partial \ln \gamma_k}{\partial \ln X_k} \right) \quad (2.19)$$

so that for dilute solutions, the intrinsic diffusivity is the same as tracer diffusivity. This accomplishment provided a satisfying link between the phenomenology and the physics of the problem.

The Matano Interface

Another plane in the diffusion couple whose value can be unambiguously evaluated is the Matano interface. This is obtained by calculating the value of 'x' where the area under a presumed original step function is equal to that under the concentration-penetration curve. It is commonly (and erroneously, as it turns out) assumed that the Matano interface is fixed with respect to the external frame during diffusion, and that it is the same plane for all the components. The experimental observations to the contrary are usually dismissed as due to the imprecision associated with the determination of the C(x,t) profile, using, for example, the electron microprobe. This question is taken up in detail in chapter 4.

Difficulties in Applying Fickian Phenomenology to Experiments

With this brief review of the phenomenological theory, which is the bulwark of the current understanding of diffusion

phenomena, the triumphs and the pitfalls of the theory (even in the relatively simple case of one dimensional diffusional flow) can be enumerated.

For a ternary system, a tedious and complicated experimental procedure involving the preparation and analysis of many diffusion couples yields a 2×2 matrix of interdiffusion coefficients. These coefficients, D_{ij} , can only be evaluated at the points of intersection of the composition paths of these couples. Surfaces modelling the composition dependence of the elements of this matrix are thus obtained. This information may then be used to predict the diffusion behavior of any arbitrary couple constructed in the system. Unfortunately, the values of these hard-won coefficients are only very indirectly related to the actual motion of the three components through the lattice. It is therefore not possible to establish connections between the measured diffusion coefficients and the physical attributes of atoms that would then form a basis for predicting diffusion behavior of that species in other systems.

If a system has four or more components, e.g., Nb-Al-Ti-O, then the corresponding 3×3 matrix of *interdiffusion coefficients* cannot be evaluated from experimental information, as this would require the intersection of three composition paths from three couples, an event that has a probability of measure zero.

There is, therefore, no framework in the traditional approach that fosters the development of a perspective that allows inferences and extrapolation of observed behavior from one composition range to another within a system, much less from one system to another. Thus, progress in developing experimental information about diffusion in higher order systems requires an approach that is different from the traditional phenomenological formalism. Visualization of the actual intrinsic atom jumps, as they are driven by gradients, is a viable alternative with a physical basis.

The next chapter presents a brief review of the contributions made by various researchers, both in the theoretical and the experimental arenas, to the study of diffusion in multi-component systems within the context of the traditional Fickian approach (TFA), which was introduced in this chapter.

CHAPTER 3

DIFFUSION STUDIES IN MULTICOMPONENT SYSTEMS

The importance of the role played by diffusion in microstructural evolution, and hence in the consequent properties of the material, cannot be over-stated. As a result, an abundance of literature exists on this subject, both in metallic (substitutional and interstitial alloys) and nonmetallic systems. The processes studied are also widely varied and include growth, dissolution, precipitate coarsening, diffusion bonding, composite compatibility, oxidation and so on. Of special pertinence to this work are the studies involving one-dimensional diffusional flows in semi-infinite couples. By eliminating such complications as finite boundary conditions, non-linear diffusion geometries, etc., these studies tend to focus on understanding the fundamental process of diffusion rather than trying to gain a complete picture of some specific situation, which is precisely the intent of this investigation. Without diminishing the importance of empirical investigations, it seems logical that the development of a theoretical methodology would only serve to facilitate such research. The modelling of diffusion using the effective mean jump

frequencies is an attempt to provide a new more realistic framework for experimenters.

What follows is a brief synopsis of the important milestones achieved over the years by various investigators in understanding diffusion phenomena in metallic systems. For a comprehensive survey of literature on this subject, the reader is referred to other works.^{8,21-23}

"Uphill" Diffusion in Ternary Systems

One of the earliest surprises in the study of diffusion in higher order systems came from Darken's work,²⁴ in which he demonstrated that a given atomic species in an alloy can diffuse without or even up a composition gradient! In a semi-infinite couple of Fe-C and Fe-C-Si alloy with about the same carbon content, the carbon was found to redistribute itself on both sides of the weld interface. The resulting composition path (sequence of compositions encountered along the diffusion direction in the diffusion zone) was an S-shaped curve. Darken postulated that even though carbon diffused *uphill with respect to its concentration gradient*, it was, in fact diffusing *down its chemical potential gradient*, due to its higher thermodynamic activity on the side containing silicon. As will be seen in later chapter, Darken's experimental results can be duplicated by the jump frequency approach to diffusion studies. This experiment also served to underscore the underlying complexities that are not made evident in the

Fickian approach.

These S-shaped composition paths were also observed by Rhines et al.,²⁵ in their study of bronze-brass couples. In their case this effect is attributed to the differences in diffusivities of tin and zinc. They also concluded that the paths pointed away from the fast-moving species. Incidentally, one of the co-authors of this study of copper alloys was R.T. DeHoff, and it is this work that inspired him and his students to think of an alternative to the Fickian approach. As a matter of fact, an early attempt at formulating an alternative strategy was the relative penetration tendency (RPT) approach, envisaged by DeHoff. The RPT approach will be reviewed in a later chapter.

Theoretical Developments in Multi-component Diffusion

The significance of the shape of the composition path on gleaning information about the diffusion process was recognized by Rhines and Clark.²⁶ In a study of diffusion generated composition paths in the Al-Mg-Sn system, these authors generated a set of rules for the paths in both isomorphous and multi-phase couples, which is reviewed in detail by Kirkaldy and Brown.²⁷

The next significant progress in the study of ternary system was due to Kirkaldy and coworkers. Working with Brown²⁷ and Fedak,²⁸ Kirkaldy developed a more comprehensive set of rules and theorems, that included Rhines' work, for deriving

composition paths in ternary isothermal diffusion. He also was able to report the diffusion coefficients for silicon and carbon by analyzing (using basically a Boltzmann-Matano type approach) Darken's data.²⁹ He followed this work up with a series of theoretical papers,^{29,32} in which he attempted to reconcile, albeit unsuccessfully, the phenomenological approach with the atomistic approach. Kirkaldy was well aware of the import of the Kirkendall velocity of the lattice and took special care to use interdiffusion fluxes only. In addition, in much of Kirkaldy's analytical work, *the diffusion coefficients were constant for all components in a given phase*. This assumption is obviously naive in view of the fact that the diffusivities of the various atomic species may differ by several orders of magnitude in a given phase field as, for example, in ternary brasses.²²

Coates,³³ who was part of Kirkaldy's group, extended these ideas further. He explored the stability of planar interfaces using perturbation theory. Unfortunately, his results are unwieldy and are of limited practical value, except in limiting cases. For example, if the composition path were to run tangential to the two-phase field boundary, one would expect the onset of instability. He followed this work up with a very elegant treatment for precipitate growth in ternary dilute solutions of the type Fe-Mn-C.³⁴ Two of the remarkable outcomes of this research are the interface composition and interface velocity contours for various gross

compositions from which precipitation takes place. For example, Coates demonstrated that, due to the large difference in the diffusivities of carbon and manganese, a precipitating system will pick a tie line that does not pass through the gross composition for establishing conditions of equilibrium at the interface between the particle and the matrix. Once again, Coates also assumes constant diffusivities and neglected coefficients of the D_{ij} (i not equal to j) type, although he later extended his analysis to include them. Under these circumstances, one can easily extend this analysis to 4-component systems.³⁵

Experimental Work in Multi-component Systems

All the theoretical advances cited above were made at a time when the experimental information was lacking. Kirkaldy had already proposed a method for obtaining interdiffusion coefficients in ternary alloys. This method, later improved by Ziebold and Ogilvie,⁷ has been used by various researchers to obtain interdiffusion coefficients experimentally.^{6,8,21,29,36-38}

On the other hand, *obtaining intrinsic diffusion coefficients*, which provides the *real insight* into the mechanism, is even more tedious. A method, proposed by Philibert and Guy,^{39,40} once again requires two independent couples with the same composition at some given point, but in addition has the stipulation that this point also be the point marked by inert Kirkendall markers. This is nearly impossible

to achieve in a pair of sandwich type couples. However, Dayananda and Grace³⁷ ingeniously solved this problem by the use of vapor-solid diffusion couples in the Cu-Mn-Zn system. By controlling the vapor pressure of zinc, they were able to place different alloys under the vapor source, and yet maintain a constant concentration at the interface where the markers are located. Other noteworthy analyses of intrinsic behavior in ternary systems are due to Ziebold and Cooper⁴¹ and Schonert.⁴²

Dayananda and co-workers also reported experimentally determined intrinsic diffusivities in other systems.^{43,44} Wan⁸ also compared several different techniques for evaluating intrinsic diffusivities in the Cu-Ni-Zn system at 900°C. One method was to use the inter-relations between the chemical potentials and the tracer and intrinsic diffusivities, the other was use Philibert and Guy's idea, but circumvent the problem of markers not being in the desired spot by "estimating" the lattice velocity at that point. The success of these techniques was modest.

With regard to evaluating diffusion coefficients from concentration gradients, the following point is worth noting. On the one hand, in order to exploit the simplifying assumption that the diffusion coefficients are not functions of concentration, the couples studied should be selected so that the concentration differences are small. On the other hand, since the quantities needed for determining the D's are

the *gradients of the concentration*, obtained by differentiating the experimental penetration curves, it seems desirable to have a finite and large concentration difference between the end-point compositions. This juggling act that must be performed to achieve a middle ground between optimal analytical sensitivity and minimal corrections for errors due to simplifying assumptions is well recognized and has been tackled by various researchers starting with Ziebold.²¹

New Strategies in Theoretical and Experimental Studies

The impact of the experimental design on the determination of the highly sensitive off-diagonal diffusivities has also been explored in some detail by Kirkaldy et al.⁴⁵ The identification of extrema in gradients and fluxes can also be useful in bolstering the accuracy of the analysis. This idea is explored in some depth in a review by Dayananda and Murch.⁴⁶ They speak of an identifiable 'Zero flux plane' (ZFP), which when taken in conjunction with a thermodynamic model for the solution, yields simplified and yet accurate relationships that can then be used in evaluating the diffusion coefficients. The implications and nuances of the notion of the ZFP are numerous and interesting, but beyond the scope of this survey. Suffice it to say that Dayananda's work represents a constructive conceptual departure from the beaten path.

One of the major shortcomings of these techniques, apart

from their cumbersome nature, is the fact that the composition at which the D's are evaluated is unknown at the start of the experiment, since the point at which two composition paths intersect is by no means evident from the choice of the couple. This problem effectively stifles any effort to apply these ideas to quaternary systems, as no such intersection of composition paths can be guaranteed *a priori*.

Another problem in the type of research surveyed above (Kirkaldy's work for example) is that after a series of complex mathematical manipulations one sometimes arrives at negative values for the diffusion coefficients. This fact raises the following question: Does the negative result stem from the thermodynamics of the ternary solid solution, or a consequence of a large difference in the jump frequencies of the different atomic species, or due to a specific combination of thermodynamic and kinetic factors? As Castleman⁴⁷ points out, "It is obvious that without a detailed *apriori* understanding of the atomistic mechanisms operating in a given system, speculations of the kind described above are fruitless" {page 45}. By directly using the jump frequencies as input (which cannot be negative by definition) the approach presented in this work circumvents these problems.

On the subject of multi-phase systems, there is a significant amount of literature. Pertinent work in this area is cited in a later chapter that deals with the moving phase boundary problem.

Application of diffusion analysis to specific phenomena, e.g., growth, coarsening, oxidation, shape stability in mechanical alloying, etc., are also in the literature. For a sample of this type of research, the reader is referred to a special publication of TMS edited by Romig and Dayananda.⁴⁸

Despite the voluminous nature of the diffusion studies in both the theoretical and experimental areas, with all the attendant mind-boggling mathematics, with a few notable exceptions (e.g., Coates' work on the Fe-C-X system³³), very little attention has been paid to *analyzing patterns of behavior*. The relative penetration tendency approach is one such effort launched by DeHoff and his coworkers^{4,5,49} and is described in chapter 5. This chapter serves as a prelude to the introduction of the jump frequency approach in chapter 6, which forms the crux of the work presented here.

The next chapter concerns itself with the traditional Matano analysis and its shortcomings with regard to the experimental determination of kinetic descriptors of diffusion.

CHAPTER 4

EXPERIMENTALLY ACCESSIBLE REFERENCE FRAMES IN DIFFUSION

Two key pieces of information that can be gleaned from diffusion experiments involving one-dimensional diffusion in semi-infinite couples are the location of the Matano and Kirkendall interfaces in the diffusion zone. The former information is valuable in extracting kinetic descriptors for *interdiffusion*, while the latter provides a handle on extracting the descriptors for *intrinsic* diffusion of the atomic species. Care should be exercised to ensure the proper interpretation of these two interfaces in analyzing experimental data. This chapter sets up the mathematical basis for properly identifying these interfaces in semi-infinite diffusion couples.

The Matano Interface

During diffusion, it is important to recognize the reference frame with respect to which the velocities of the various moving entities are being described. Each definition of the reference frame leads to different expressions for describing the diffusion kinetics. The most obvious of these reference frames is the so called Laboratory Frame, whose

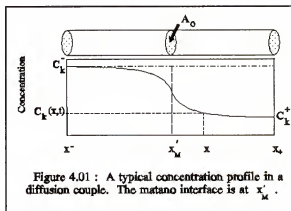
stationary origin may be visualized as one corner of the room where the experiment is carried out.

While the laboratory frame is straightforward, it does present conceptual difficulties in understanding the diffusion process because the moving atoms are responding to their immediate surroundings, and these surroundings are constrained by the crystal lattice which is continuously moving and readjusting. Therefore it is traditional to invoke an internal reference frame in the sample itself. The most common of these frames is based on the Matano interface. It is commonly assumed that the Matano interface stays fixed throughout the diffusion process, with respect to the laboratory frame, thereby obviating the need for an external reference frame. In practice, for multi-component diffusion, it is typically found that the Matano interface as determined from the concentration-penetration profiles is different for each component! This observation is usually attributed without analysis to the lack of experimental precision in determining the concentration, $C(x,t)$, although it is also known that the variation of molar volume with composition could be a contributing factor. In what follows, this discrepancy is resolved, with special focus on the role played by molar volume variations and the creation/annihilation of lattice sites due to the Kirkendall effect.

Locating the Matano Interface

Figure 4.01 sketches a typical concentration-penetration curve for component k at some time t of observation in a semi-infinite diffusion couple. The quantities defined are

$C_k(x,t)$, the concentration of component k ,
 C_k^- , the initial concentration of k on the LHS of the couple,
 C_k^+ , the initial concentration of k on the RHS of the couple,
 x^- , a position outside the diffusion zone on the left,
 x^+ , an analogous position on the right, and
 A_0 , the initial cross-sectional area of the sample.



The variable x is in the direction of diffusion and is a positional coordinate in the external frame. Experimental data is usually accumulated in terms of the atom fraction, X_k , for each of the components. A separate measurement of the molar volume, V , of the multi-component system would permit the evaluation of C_k from the atom fraction data, since

$$C_k = \frac{X_k}{V} \quad (4.01)$$

Under the constant V assumption, the cross-sectional area, A_0 , remains constant throughout the experiment. In that case, if x_M' is the position of the Matano interface, the number of atoms of k at time zero is:

$$n_k = C_k^- A_0 (X_M' - X^-) + C_k^+ A_0 (X^+ - X_M') \quad (4.02)$$

while at time 't'

$$n_k = \int_{X^-}^{X^+} C_k(x, t) A_0 dx \quad (4.03)$$

Invoke the conservation of atoms of k and set equations 4.02 and 4.03 equal to each other, to get

$$X_M' = \frac{\int_{X^-}^{X^+} C_k(x, t) dx + (C_k^- X^- - C_k^+ X^+)}{(C_k^- - C_k^+)} \quad (4.04)$$

If it turns out the values of x_M' obtained for each value of k from the concentration-penetration profiles are different, then this must arise either from experimental error or the incorrect assumption that A_0 remains constant.

A More Rigorous Calculation of x_m

Two factors may contribute to local volumetric expansions and contractions in the system associated with the diffusion process, (a) the dependence of molar volume on concentration and (b) the vacancy flux pattern. There is no reason to assume that the associated expansions and contractions are constrained to the diffusion direction; they are volumetric in nature. The distribution of the components of these volume changes in the x , y and z directions depends in a complex way upon the physical constraints on the system and its mechanical properties. For the present purpose, the essential effect of

these volume changes will be a surface rumpling which locally alters the cross-sectional area of the sample. Thus, in a rigorous analysis of the conservation of atoms, it must be explicitly recognized that the cross-sectional area $A(x,t)$ is a function of position and time. In this case, equation 4.03 becomes

$$n_k = \int_{x^-}^{x^+} C_k(x, t) A(x, t) dx \quad (4.05)$$

Equation 4.02 remains unchanged, as it reports the situation at $t = 0$. Setting equations 4.02 and 4.05 equal yields the value of x_M , this time without any assumptions regarding the constancy of volume.

$$X_M = \frac{\int_{x_-}^{x_+} A(x, t) dx + (C_k^- x_- - C_k^+ x_+)}{(C_k^- - C_k^+) A_0} \quad (4.06)$$

Once again, of course, nothing on the RHS depends on time, as was the case with equation 4.04, and therefore the value of x_M remains constant through time.

A Comparison Between x_M' and x_M

The integral in equation 4.06 may be written without simplification as a peculiarly weighted average cross-sectional area of the sample.

$$\int_{x^-}^{x^+} A(x, t) C_k(x, t) dx = \langle A(t) \rangle_k \int_{x^-}^{x^+} C_k(x, t) dx \quad (4.07)$$

where

$$\langle A(t) \rangle_k = \frac{\int_{x_-}^{x_+} A(x, t) \cdot C_k(x, t) dx}{\int_{x_-}^{x_+} C_k(x, t) dx} \quad (4.08)$$

Note that this average area, weighted by the concentration will be different for different values of k and further, this position dependent area is a function of time. Equation 4.06 may be rewritten as

$$X_M = \frac{\langle A(t) \rangle_k \int_{x^-}^{x^+} C(x, t) dx + (C_k^- x^- - C_k^+ x^+) A_0}{(C_k^- - C_k^+) A_0} \quad (4.09)$$

The difference in position of the rigorously evaluated Matano interface given by equation 4.09 and that which is commonly computed from equation 4.04 is

$$\begin{aligned} X_M - X_M' &= \frac{\langle A(t) \rangle_k \int_{x^-}^{x^+} C_k(x, t) dx}{(C_k^- - C_k^+) A_0} + \frac{(C_k^- x^- - C_k^+ x^+) A_0}{(C_k^- - C_k^+) A_0} \\ &- \frac{A_0 \int_{x^-}^{x^+} C(x, t) dx}{(C_k^- - C_k^+) A_0} + \frac{(C_k^- x^- - C_k^+ x^+) A_0}{(C_k^- - C_k^+) A_0} \end{aligned} \quad (4.10)$$

or

$$X_M' = X_M + \frac{\int_{x^-}^{x^+} C(x, t) dx}{(C_k^- - C_k^+)} \cdot \left[1 - \frac{\langle A(t) \rangle_k}{A_0} \right] \quad (4.11)$$

Thus, the incorrectly calculated X_M' differs from the rigorously calculated X_M by the second term in equation 4.11. Notice that this term disappears if the average cross-sectional area, $\langle A \rangle_k$, is not a function of time.

The Boltzman-Matano Analysis

By making a variable transformation of the x-axis (the diffusion direction), Matano¹ applied an earlier analysis of Boltzman² to Fick's second law and obtained (reproduced here without the details of the derivation)

$$D(C) = -\frac{1}{2} \cdot \left(\frac{d\lambda}{dC} \right)_C \cdot \int_{C^+}^C \lambda dC \quad (4.12)$$

Here the variable λ is time independent and is equal to $(x \cdot t^{1/2})$ and therefore,

$$D(C) = -\frac{1}{2t} \cdot \left(\frac{dx}{dC} \right)_C \cdot \int_{C^+}^C x dC \quad (4.13)$$

The index origin, i.e., the Matano interface is given by the equality

$$\int_{C^+}^{C^-} \lambda dC = 0 \quad (4.14)$$

or, at a fixed time t ,

$$\frac{1}{\sqrt{t}} \int_{C^+}^{C^-} x dC = 0 \quad (4.15)$$

where C^+ and C^- are the end-point compositions on the left and right sides of the semi-infinite couple respectively.

By graphically estimating the derivative and the integral in the right hand side of equation 4.13 from the experimental data, one can obtain D as a function of C .

Equation 4.13 has been extended by Kirkaldy²³ to multi-component systems, yielding the following result:

$$\frac{1}{2} \int_{c_i^-}^{c_i^+} \lambda dC_i = -2 \sum_j^{n-1} D_{ij}^k \left(\frac{dC_j}{d\lambda} \right)_C \quad \{i = 1, 2 \dots (n-1)\} \quad (4.16)$$

with the origin given by

$$\int_{c_i^-}^{c_i^+} \lambda dC_i = 0 \quad \{\text{for all } i\} \quad (4.17)$$

Equation 4.16 can be used to evaluate the two by two matrix of ternary diffusion coefficients by evaluating the required derivatives and integrals at the same value of C in the composition paths of two different couples which thereby yield two simultaneous equations in two unknowns. This analysis has been applied (with certain computational improvements) by Ziebold and Ogilvie,⁷ Vignes and Sabatier⁶ and Wan⁸ in their ternary diffusion studies which are discussed in chapter 8 of

this work.

As already pointed out, application of equation 4.16 to quaternary and higher order systems would require the unlikely event that the composition paths of *three couples intersect at the same point*.

The key point in the analysis is that the location of the origin given by equation 4.15 *must be the same* for all the components. Experimentally, this does not turn out to be the case¹⁴ and the discrepancy is usually credited to experimental error when, as we have shown above, it could be the result of asymmetric volumetric changes in the directions orthogonal to that of diffusion.

The Kirkendall Interface

Apart from the Matano interface which can be graphically or numerically identified from the concentration-penetration profiles, there is one other interface of interest in diffusion studies. If inert markers are placed at the original weld interface in a semi-infinite couple then, in general during diffusion, these markers move to a position not coincident with the Matano interface, and this position is called the Kirkendall interface.

The position of the Kirkendall interface (with respect to the Matano interface, under the assumption that the latter is fixed in the laboratory frame) is determined by the imbalances in the intrinsic fluxes/flows of the various atomic species.

These imbalances (and hence the consequent lattice velocities) are not the same at all points along the diffusion direction and tracking the position of the markers only tells one piece of the story regarding the intrinsic behavior of the atoms.

Darken²⁴ developed a scheme (see chapter 2) for relating the inter-diffusion coefficients, the intrinsic diffusivities and the tracer diffusivities for diffusion in binary systems. Using his relationships, two different strategies can be devised for the experimental evaluation of intrinsic diffusivities. One can either measure marker movements and the chemical diffusion coefficients or measure tracer diffusivities and the chemical diffusion coefficients. Either one of the above pairs of information can be related to the intrinsic diffusion coefficients via Darken's analysis except that the second one involves assumptions regarding the thermodynamics of the situation.

Kirkaldy and Young¹⁶ present an analysis similar to the one above for ternary systems. As these authors acknowledge, the task of evaluating the six independent intrinsic diffusion coefficients for ternary systems (one of the concentrations is considered dependent on the other two), using the marker movement information is a formidable one. They derive relationships expressing intrinsic diffusivities as a function of both the tracer and the interdiffusion coefficients and recommend, in view of the experimental and analytical difficulties involved in marker experiments, that these

relationships be used to estimate the intrinsic diffusivities. Nevertheless, as reviewed in the previous chapter (chapter 3), marker movements have been used, with a measured degree of success, in evaluating intrinsic behavior of ternary systems.

The Kirkendall interface, i.e., the plane containing (at the end of the diffusion experiment) the markers placed at the original weld interface has been studied by various researchers under certain assumptions regarding the intrinsic diffusivities and the thermodynamic solution model for the alloy system for diffusion in multi-component systems. For example, Adda and Philibert^{50,51} have shown that, in binary diffusion with constant intrinsic diffusivities (so that the interdiffusion coefficient is a linear function of composition), the Kirkendall interface *coincides with the inflection point* in the penetration curve. Subsequently, van Loo et al.⁵² have extended this reasoning to multi-component systems. Their strategy was to model the penetration curve as two error functions on either side of the Kirkendall interface with the same slope at this interface. From this model they were able to derive a relationship for the time-dependence of the marker position. Combining this approach with the assumption of constant intrinsic diffusivities and an ideal solution model for the alloys, they extended this approach to ternary systems.

Large Kirkendall movements are generally considered undesirable in practical applications because of the possible

generation of porosity, delamination of high temperature coatings etc., due to the coalescence of point defects. With this in mind, Morral et al.⁵³ attempt to relate the time dependence of marker position to the concentration difference between the terminal alloys. They arrive at a linear relationship between marker movement and the concentration differences which, they claim can be put to use in alloy design programs to reduce or eliminate marker movements.

Van Loo et al.^{54,55} have developed a theoretical basis for tackling marker movement in two-phase systems with a migrating planar interface. This work will be considered in greater detail in the chapter dealing with the moving phase boundary.

Diffusion Coefficients versus Jump Frequencies

The purpose of the above development is to demonstrate the difficulties associated with the *starting point* of the Matano analysis that would ultimately lead to the calculation of the kinetic descriptors in the traditional theory, namely the interdiffusion coefficients. On the other hand, the approach taken in this work, which will be detailed later, does not suffer from such a shortcoming. This is because the analysis assigns values to the kinetic descriptors (in this case the effective mean jump frequencies) *ab initio*, and then compares the computer generated concentration penetration profile and/or the composition paths to the experiments.

Furthermore, the kinetic descriptors obtained by the jump

frequency approach (JFA), are applicable to the *whole region of the phase diagram under study*, and there is no need to piece together a collection of matrices of diffusion coefficients obtained at specific and discrete compositions, as is done in the Boltzmann-Matano analysis.

Finally, the jump frequency approach yields results from the computer simulations that are far more intensive than the experimental results themselves. For instance, the *entire lattice velocity profile* is produced, not just at the marker plane, and this fact takes on a greater significance in multi-phase systems where there are discontinuities in the lattice velocity and the velocity of the Kirkendall markers, taken by itself, means very little.

The next chapter is a review of the relative penetration tendency (RPT) or the linear approximation approach (LAA), presented here as a prelude to the introduction of the jump frequency analysis (JFA) in chapter 6.

CHAPTER 5 THE RELATIVE PENETRATION TENDENCY (RPT) MODEL

Introduction

The development of the Relative Penetration Tendency (RPT) model, alternatively known as the Linear Approximation Approach (LAA), represents a novel point of view, inasmuch as it tackles the problem *directly in terms of intrinsic flows of atoms*, and not, as is traditionally done, in terms of quantities pertaining to interdiffusion. Because of this radical departure from the traditional viewpoint, this approach has not found widespread acceptance amongst diffusion researchers except for a handful of people.⁵² However, this conceptual leap is the inspiration behind the work presented in this dissertation and is therefore reviewed in this chapter in some detail.

The kinetic descriptors that are typically calculated in ternary diffusion studies consist of a matrix of interdiffusion coefficients D_{ij}^k , where the superscript k refers to the component whose composition is chosen as a dependent variable. By themselves, these diffusivities provide little insight into the actual intrinsic behavior of the atomic species since a different choice of k , for example, can alter

the hierarchy of their values. Therefore, DeHoff et al.⁴ embarked on an entirely new approach that is based on the analysis of the composition paths and the Kirkendall shift patterns rather than the concentration-penetration curves themselves, as is commonly done.

In this RPT model, the motion of each species is described in terms of its depth of penetration into the side of the couple where its concentration is low and the depth of its draw from the side where its concentration is high, rather than in terms of its flux, which is a function of the position in the couple. For the three species, these penetration/draws are expressed as ratios and hence the term, relative penetration tendency (RPT). In an actual couple, the imbalance in the flows of the three components is continually adjusted by the creation or annihilation of lattice sites. On the other hand, in the RPT approach, the flows occur in a *conceptual rigid lattice*, so that there is an accumulation or dearth of lattice sites at various positions in the couple. After the penetrations and draws are completed, the adjustment of the lattice is done in one step.

This procedure results in the generation of (a) concentration-penetration profiles, (b) the composition paths and (c) the kirkendall shift pattern. The latter two are used to compare theory with experiment and to predict patterns of behavior. The analysis is further kept simple by approximating the penetrations/draws in the rigid lattice as

straight lines and hence the name, linear approximation approach (LAA). This procedure is illustrated in the next section with the help of a 50-50 AB/BC ternary couple.

The Concept Illustrated with the 50-50 AB/BC Couple

The backbone of this approach is the concept of a *rigid* lattice. This is best illustrated by the example shown in figure 5.01. Consider a semi-infinite ternary diffusion couple between a 50-50 A-B alloy and a 50-50 B-C alloy, so that initially there is no gradient in the concentration of component B across the diffusion couple {see figure 5.01}. Now suppose we allow the three elements to redistribute themselves by penetrating into the region where their concentration is lower, *without maintaining a constant concentration of atoms per unit volume in the diffusion zone*, as illustrated in figure 5.01 (a, b, c,). Further assume, for the sake of illustration that the atoms of 'A' move with greater vigor and hence penetrate farther than the atoms of 'C' (in this particular example, the atoms of 'B' do not move because the concentration of B is the same on both sides, and hence their penetration depth is not of concern). Also, let these 'penetrations' be linear in this conceptual rigid lattice in order to facilitate mathematical manipulations (hence the phrase, Linear Approximation Approach). The

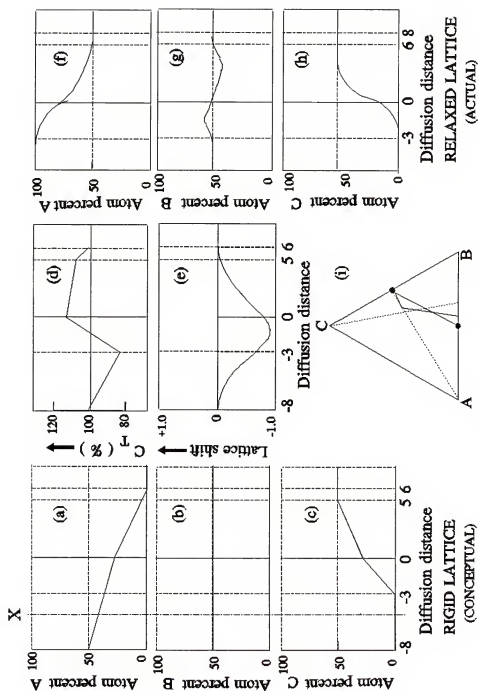


Figure 5.01: The relative penetration tendency (RPT) model for an AB/BC ternary diffusion couple. The distance units are arbitrary.

relative penetration tendencies (RPT's) of components is merely the 'depth' to which the concentration-distance line penetrates in figure 5.01 (a, b, c), with all these penetration tendencies expressed as a ratio.

Figure 5.01 (d) shows a graph of the total number of atoms, C_T , in the rigid lattice, subsequent to the flows of the various atomic species. {In this illustration, an arbitrary but constant cross-sectional area is assumed, so that there is a net accumulation/depletion of atoms on all planes normal to the diffusion axis}. In reality, during diffusion, the imbalance in the flows of 'A' and 'C' will result in the creation/annihilation of lattice sites all along the diffusion zone, giving rise to a lattice velocity associated with various points, which is the Kirkendall effect.

If we now allow the rigid lattice to relax, so that the number of lattice sites in any given plane is adjusted back to its normal value. In this particular example that is being considered, these planes will shift to the left (there is a deficiency of lattice sites on the A-B side of the couple and an excess on the B-C side). The extent to which any lattice plane shifts to the left or the right (a shift to the right being positive by convention), can be plotted against the distance in the diffusion direction. This produces a *Kirkendall shift profile*, as shown in figure 5.01 (e).

The end result of this thought experiment is shown as the

concentration-penetration profiles in Figure 5.01 (e, f, g). Using these profiles, one can obtain a composition path (sequence of compositions encountered in the penetration profile) and compare it with experiment. This path is shown on the Gibbs triangle in figure 5.01 (i). The other quantity of interest that comes out of this analysis, as already mentioned, is the Kirkendall shift profile, which at any given point is simply proportional to the area under the C_T curve to the left of this point. Usually, only the shift of the inert markers at the original weld interface is measured experimentally. This shift is simply the area under the C_T curve, to the left of the original marker plane.

The biggest surprise in the example given above is that component 'B' shows an undulation in its concentration-penetration profile {figure 5.01 (g)}, in spite of the assumption that there is no redistribution of 'B' at all in the rigid lattice for this particular couple in this model. This is merely a consequence of the way in which diffusion data is reported. Tracking the concentration (in atoms per unit volume) of any species in a volume element provides no clue as to whether this concentration is a consequence of the flux of this particular component, or is merely due to increase/decrease in the number of atoms of the other components due to *their* fluxes in and out of this volume element. Focus, for instance, on the plane marked 'X' in figure 5.01 (a, b, c). Here the atoms of component A have

moved out but the resulting vacant lattice sites stay vacant because there is no penetration of component *C* this far into the left hand side. As a result, expressed as a percentage of the total number of atoms, the concentration of component *B* exceeds its original value of 50%. Of course, this means that, in order to gain a clear picture, greater attention must be paid to the *intrinsic behavior* of the individual atoms, resulting in their fluxes, flows etc. than to the quantities pertaining to *interdiffusion*, which are the ones that are commonly reported.

In the above example, the RPT's of the various components are dependent on composition. The *composition dependence* of the penetration tendencies is taken into account by lengthening (or shortening) the depth of penetration/draw of the component of interest, depending on the *initial composition* of the alloy forming the couple. The primary effect of composition dependent penetration tendencies is, as will be shown later, to shift the *cross-over point*, i.e., the point at which the composition path crosses the line joining the end-point compositions, toward one end-point or the other. If the penetration tendencies were composition independent (that is the penetration *depth* of any species *k* into the *k*-poor side of the couple *is the same as* the draw of that species from the *k*-rich side), the cross-over point will bisect the line joining the end-point compositions.

Ternary Isomorphous Systems - Patterns of Behavior

As observed by Wan,⁸ in any arbitrary couple in the ternary system {see figure 5.02 (a)}, there are five segments in the composition path (here the penetration tendencies are in the ratio A:B:C::5:3:1), that are determined by the three diffusing components. The terminal segments QR and PU are controlled by 'A', the fast mover, with QR (the end with the higher 'A' content) pointing away from the A-corner of the Gibbs triangle, and PU (the lower 'A' concentration end) pointing toward the 'A' corner. The center portion ST intersects the line joining the end-point compositions and is rotated toward pointed toward the 'C' corner, which is the slow moving species. The remaining segments RS and TU are controlled by the behavior of all three components.

DeHoff⁴ proposed that, as shown in Figure 5.02 (b), the Gibbs triangle representing the high temperature isotherm can be divided qualitatively into eight regions of interest when exploring the behavior of the composition paths on the end-point compositions and the RPT's. In this representation, a ternary alloy of composition 'P' is coupled with various binary alloys on the sides of the Gibbs triangle. Choosing this point 'P' as being at the center of the Gibbs triangle, DeHoff et al.⁴ picked *sixteen couples* that spanned the entire triangle.

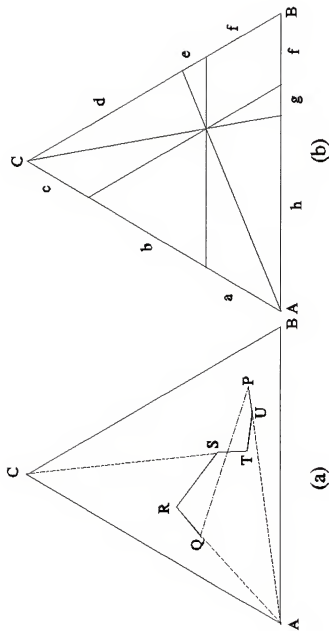


Figure 5.02: (a) Illustration of the composition path predicted by the RPT approach, with the five segments as explained in the text.
 (b) The division of the Gibbs triangle into 8 regions of interest for an arbitrary ternary composition 'p'. The other half of the couple, 'Q', should be selected along the binary lines bounding the triangle.

Using these sixteen compositions as one end-point of the couple and the 1/3-1/3-1/3 ternary alloy as the other, they calculated the concentration profiles and the composition paths for both the concentration independent and the concentration dependent penetration tendencies.

DeHoff and co-workers systematically explored the patterns of behavior for the various ratios of the penetration tendencies of the components, starting with the composition independent cases and culminating with the composition dependent ones. Their results are reproduced here {see figures 5.03 through 5.06} for comparison with the results of the jump frequency approach (JFA) which are presented in chapter 7. An explanation of these figures follows.

For the case of the concentration independent RPT's, they chose six sub-cases, with the RPT's of A, B and C in the following ratios:

- (1) A:B:C::5:5:5; (2) A:B:C::5:0:0; (3) A:B:C::5:5:0;
and (4) A:B:C::5:3:0.

The results from the above cases are presented in Figures 5.03 and 5.04. Detailed explanation of the way the various paths are curved is being reserved for the results of the JFA analysis, presented in chapter 7, which basically follow the same pattern as their results.

For the concentration dependent cases, they chose to represent the RPT's as a plane {see in Figure 5.05 (a)} for

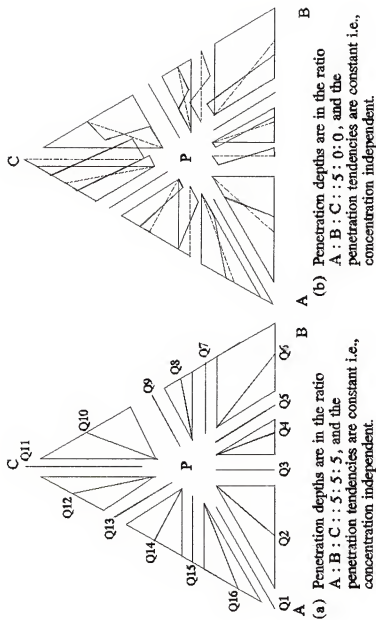


Figure 5.03: Exploded Gibbs triangles depicting the composition paths for concentration independent RPT's as indicated. The 16 couples chosen by DeHoff et al.⁴ are the central composition 'p' coupled with the unary/binary compositions 'Q'.

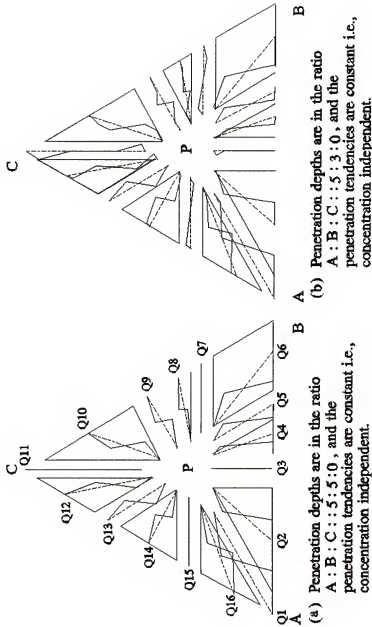


Figure 5.04: Exploded Gibbs triangles depicting the composition paths for concentration independent RPT's as indicated. The 16 couples chosen by DeHoff et al.⁴ are the central composition 'P' coupled with the unary/binary compositions 'Q'.

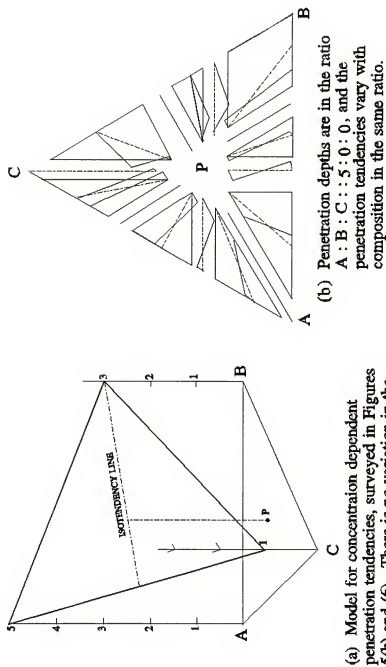


Figure 5.05: (a) a graphical representation of equation 5.01.
 (b) exploded Gibbs triangles showing the patterns of compositions for composition dependent RPT's in the ratio $A : B : C :: 5 : 0 : 0$.

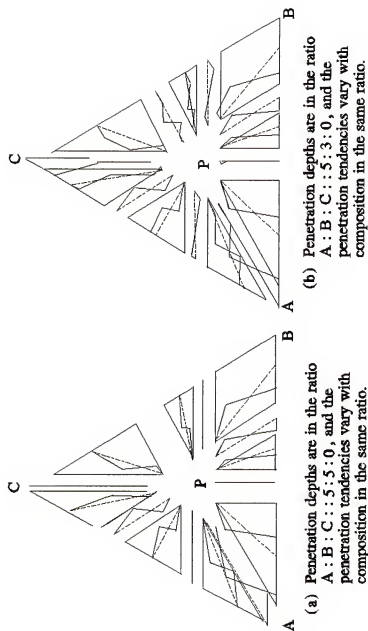


Figure 5.06: Exploded Gibbs triangles depicting the composition paths for concentration dependent RPT's as indicated. The 16 couples chosen by DeHoff et al.⁴ are the central composition 'p' coupled with the unary/binary compositions 'Q'.

the case where the RPT's are in the ratio 5:3:1, and their composition dependence is also in the same ratio. Thus, in all these cases, the penetration depth of species 'k' is given by

$$(RPD)_k = (RPT)_A \cdot N_A + (RPT)_B \cdot N_B + (RPT)_C \cdot N_C \quad (5.01)$$

where, $(RPT)_k$ is the relative penetration tendency of 'k', N_k is the mole fraction of 'k' in the starting alloy, and $(RPD)_k$ is the relative penetration depth of 'k'.

Their results for these concentration dependent RPT's is presented in figure 5.05 (b) as well as figure 5.06 (a & b). In these cases the ratio of the RPT's as well as their composition dependence are, in order, as follows: (1) A:B:C::5:0:0; (2) A:B:C::5:5:0 and (3) A:B:C::5:3:0. Once again, explanations for these observed paths are reserved for chapter 7, where similar cases are analyzed using the JFA approach. The primary effect of composition dependence is to affect the so called "cross-over point" which is the point where the composition path intersects the line joining the end-point compositions. In the case of composition independent RPT's, this point is the midpoint of that line. For the concentration dependent models, this cross-over point is shifted toward one end-point or the other, depending on the penetration/draws of all the components. For the simple case considered above, where the RPT's decreases monotonically from the A-corner of the phase diagram down to the C-corner, this cross-over shift will be toward the end-point composition

where all the species are *fast moving*.

DeHoff et al. have also presented patterns of Kirkendall shifts (in their case, *one value for X_K for each couple*, calculated for the point corresponding to the original weld interface). The results of the JFA, presented in chapter 7, show a *Kirkendall shift profile for the entire diffusion zone generated for each couple*. These results, as will be shown later, are consistent with the calculations made according to the RPT approach.

Comparison with Experimental Data

Wan³ applied the RPT approach to the data of Vignes and Sabatier⁵ on the Fe-Ni-Co ternary isotherm at 1315°C. Following the conclusion of these authors, Wan assumed that the mobilities of the three species is in the order Fe>Co=Ni. He applied a ratio of Fe:Co:Ni::5:3:3 to the RPT'S and also made them concentration dependent in the same ratio, so that

$$(RPD)_k = (RPT)_k \cdot (5N_{Fe} + 3N_{Co} + 3N_{Ni}) \quad (5.02)$$

The results of Wan's comparisons are presented in figure 5.07. In chapter 8, the same data will be reanalyzed using the JFA, and these figures compared to the results obtained there. The fit is remarkably good, especially considering the approximate nature of the analysis and the simplicity of the assumptions.

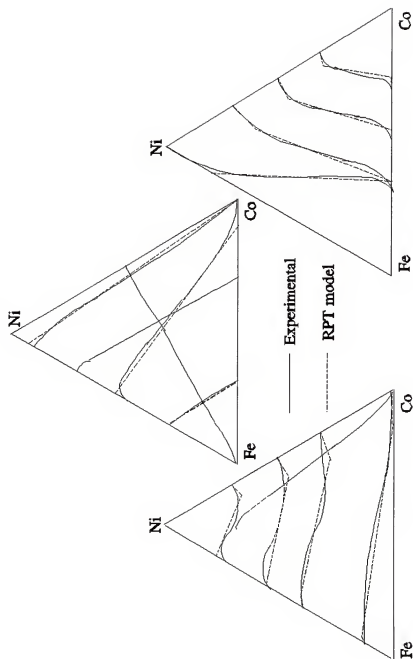


Figure 5.07: A comparison of Vignes and Sabatier's⁶ data on the Fe-Co-Ni system with Wan's⁸ relative penetration tendency (RPT) model.

Next, Wan examined the data of Ziebold and Ogilvie,⁶ on the Au-Cu-Ag system at 725°C. Except for a miscibility gap on the Ag-Cu side, this system is also isomorphous. In this system, for the couples whose composition paths did not cross the two-phase field on the Ag-Cu side, Wan used the relation

$$(RPD)_k = (RPT)_k \cdot (10 \cdot N_{Au} + 4 \cdot N_{Cu} + 1.5 N_{Ag}) \quad (5.03)$$

with the RPT's in the ratio Au:Cu:Ag::10:4:1.5. These results are reproduced from Wan's work also, in figure 5.08, with a view to comparing them to the consequences of the JFA analysis of the same data, presented in chapter 8.

Finally, Wan⁷ studied the composition paths of various ternary isomorphous couples at the copper-rich end of the Cu-Ni-Zn at around 900°C. He applied two different models for the RPT's to find agreement with the experiments. Figure 5.09 shows the model that Wan considered a better fit. In this model, the RPD's follow a relatively complicated helical surface. Equation 5.04 is an algebraic representation of these helical surfaces.

$$RPT(Zn) = 66.0X_{Zn}X_{Ni} + 41.0X_{Zn} - 22.5X_{Ni} + 10.0 \quad \dots (5.04a)$$

$$RPT(Cu) = 22.3X_{Zn}X_{Ni} + 32.7X_{Zn} - 16.0X_{Ni} + 6.5 \quad \dots (5.04b)$$

$$RPT(Ni) = 35.0X_{Zn}X_{Ni} + 18.7X_{Zn} - 11.7X_{Ni} + 4.4 \quad \dots (5.04c)$$

Figure 5.10 shows a comparison of this model to the experimental observations. These data are also reanalyzed in chapter 8.

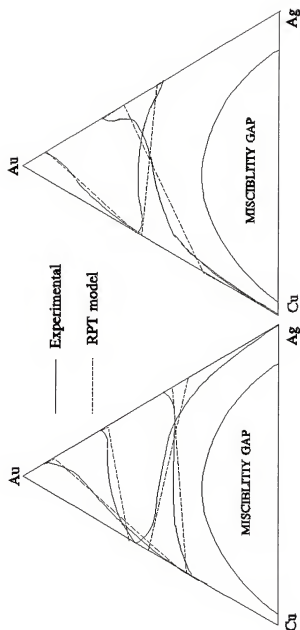


Figure 5.08: A comparison of Ziebold and Ogilvie's data on the Cu-Ag-Au system with Wan's⁸ relative penetration tendency (RPT) model. Couples with composition paths traversing the miscibility gap are not included here.

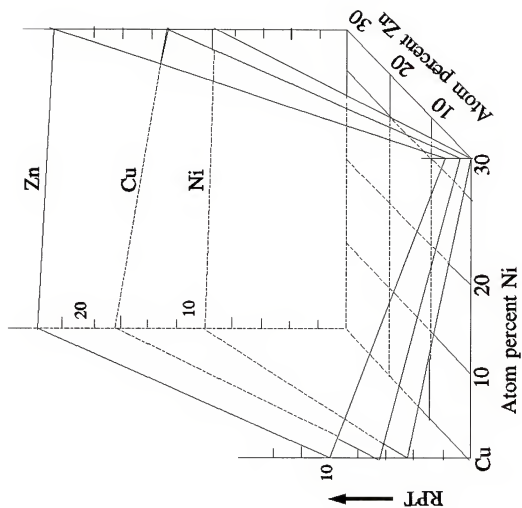


Figure 5.09: Helical surface representing the compositional dependence of the RPT's in the Cu-Ni-Zn system as modelled by Wan.⁸

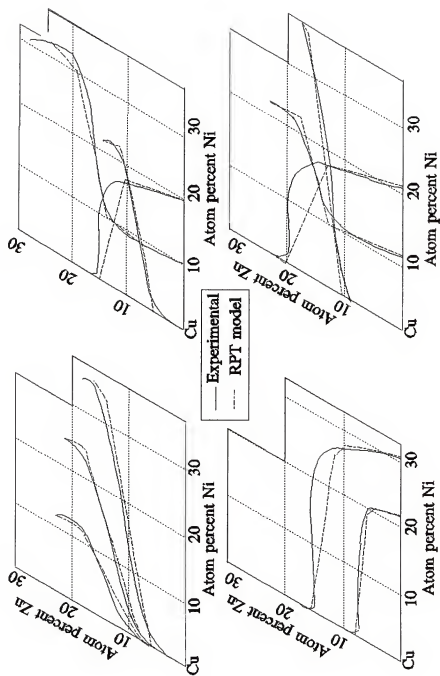


Figure 5.10: A comparison of Wan's⁸ experimental data in the Cu-Ni-Zn system with his helical model shown in figure 5.09.⁸

Concluding Remarks

As already noted, the purpose for reproducing the above results in this chapter is to enable a comparison with the analysis made using the JFA approach. This chapter is concluded with some remarks regarding the success of the RPT approach along with a comment on the improvements introduced by the JFA over this approach.

The biggest advantage of an approach such as the one based on penetration tendencies is its ability to *systematically survey patterns of behavior*. Despite the relative simplicity of its assumptions, and despite having to deal with the cumbersome abstraction of linear flows in fictitious spaces, the RPT approach has managed to produce tangible results that are consistent with experimental observations. This fact alone should clue the researcher that the study of the process of diffusion need not be as complicated as the Fickian approach seems to demand. The jump frequency approach (JFA), which is a refinement of the RPT approach, should (and does, as demonstrated in the later chapters) provide an equally good interpretation of the experiments, with the added advantage of not straying far from the physics of the process.

CHAPTER 6
THE JUMP FREQUENCY APPROACH (JFA) IN DIFFUSION STUDIES

Introduction

Diffusion in substitutional solid solutions takes place by vacancy atom interchanges. This fundamental mechanism is exploited in what follows in an attempt to apprehend a tractable kinetic description of isothermal diffusion processes in multicomponent multiphase alloy systems.

In any given volume element of the substitutional alloy, at any given temperature, there exists a concentration of vacant lattice sites. The atoms in near-neighbor positions are constantly exchanging places with the vacant sites. Each atomic species in this volume element has associated with it a *characteristic jump frequency* that depends on the environs (temperature, concentration etc.). In the absence of a gradient or driving force, these jumps are essentially non-productive in the sense of changing any of the properties of the volume element.

Not all atoms jump with the same vigor and further, some of these jumps are effectively annulled by the correlated jumping of the atom back into the same site that it left on the previous jump. Nevertheless, one can conceive of an "effective mean" jump frequency for a given atomic species in

a given volume element. This analysis will use this effective mean jump frequency, Γ_k , for atomic species k , as the kinetic parameter responsible for the rapidity with which diffusion takes place.

Preliminary Development

Consider two adjacent atom planes (a and b) that are separated by one diffusion jump distance, δ in a crystal structure.. Let the concentration (in atoms/cc) and the jump frequency of component k be C_k^a and Γ_k^a on plane a and C_k^b and Γ_k^b on plane b . For an arbitrary cross-sectional area, A , in time dt , the total number of atoms jumping from plane a to b is $(C_k^a \cdot A \cdot \delta \cdot \Gamma_k^a \cdot \alpha \cdot dt)$ where α is a factor that depends on the crystal structure and is $1/6$ for an isotropic material. There is a corresponding number for the jumps from plane b to a . The flux of atoms of k from plane a plane b is the difference between these two numbers divided by $(A \cdot dt)$. Thus the cross-sectional area as well as the time increment drop out. Based on this imagery of atoms jumping back and forth from an atom plane to an adjacent one, and applying the continuum approximation to the result, DeHoff⁵⁶ developed the following equation as an alternative reformulation of Fick's first law:

$$J_k = -\alpha \cdot \delta^2 \cdot \left(\frac{\partial C_k \Gamma_k}{\partial x} \right) \quad (6.01)$$

where,

J_k is the flux of component ' k ',

α is a function of crystal structure and is $1/6$ for an isotropic material,
 δ is the distance between the adjacent planes, i.e., the jump distance,
 C_k is the concentration of species 'k' at the point where the flux is evaluated,
 Γ_k is the effective mean jump frequency of 'k', and
 x is the measure of distance in the direction of diffusion.

In the above equation, the fluxes are *intrinsic*, i.e., they are evaluated for each component k , as its atoms respond to the non-uniformity of the jump frequency or concentration or both, *irrespective of other gradients*. This equation, therefore, is a description of what is actually happening in the system at a given point and involves no assumptions of the kind that are common to diffusion research. Whereas there are only $(n-1)$ independent interdiffusion fluxes in an n -component system, these intrinsic fluxes are all independent of each other. The intrinsic fluxes represent a *direct physical description* of atom motions during diffusion, whereas the interdiffusion fluxes are mathematical abstractions, whose meaning becomes more and more obscure as the complexity (multicomponent, multiphase) of the system, in which diffusion takes place, is increased.

Although equation 6.01 does not require it, all of the simulations that are presented in this work with jump frequency models carry with them the implicit assumption that the jump frequencies are strictly a function of the concentration of the various components in the volume element under consideration and do not depend on the gradient of these

concentrations. It appears, at this writing, that this assumption is a reasonable one. In the absence of this assumption the approach loses much of its elegant simplicity, and the meaning of the effective mean jump frequencies becomes abstruse and hence this complication is eschewed in what follows. However, it must be pointed out that, as the computer program developed in this work is concerned, the incorporation of additional terms involving gradients should pose no major problems.

DeHoff then goes on to outline a scheme for extracting the value of ' Γ_k ' at any point in the concentration penetration curve using a double integral of the experimentally measured curve. The advantage of this procedure over the traditional Matano analysis lies in the fact that less error accrues during integration than during the evaluation of slopes of experimental plots.

At the time DeHoff wrote his paper, fast computers with easy access as well as the development of convenient portable programming languages were still in the future. That situation has changed, and today we can actually write a relatively simple computer program based on a finite element analysis of the diffusion zone in a semi-infinite diffusion couple for simulating the process. Such a program has in fact been written and forms the foundation of this dissertation. The details of the set-up and execution of this program are described in what follows.

The Algorithm

The basic idea is to divide the material in the diffusion zone into a number of thin slices perpendicular to the direction of diffusion, with each slice identified by a slice number i . Throughout the simulation, the computer keeps track of these slices and the various quantities of interest associated with them. At the start of the simulation, initial position values, x_i , as well as initial concentration values, $(C_k)_i$, for each component 'k' are assigned to each of these slices. In addition, the program has built into it, a look-up table that tells the program the appropriate value of $(\Gamma_k)_i$, that corresponds to the various $(C_k)_i$ values. For the purpose of computer simulation, equation 6.01 is recast in the following finite difference form.

$$(J_k)_i = -\alpha \delta^2 \frac{((C_k)_{i+1} \cdot (\Gamma_k)_{i+1} - (C_k)_{i-1} \cdot (\Gamma_k)_{i-1})}{x_{i+1} - x_{i-1}} \quad (6.C)$$

Based on these initial values, one can now evaluate the flux, $(J_k)_i$, for all i and for each k . Consider a semi-infinite cylinder of unit cross-section that has been divided into these slices that are normal to the diffusion direction. We now pick a time interval Δt during which we let these fluxes operate, so that the accumulation/depletion of the various species of atoms in any slice i becomes $\Delta(J_k)_i \cdot \Delta t$,

where $\Delta(J_k)_i$ is the difference between the flux into and the flux out of slice i . For each slice i , the new number of atoms (per unit area of cross-section) of k can then be evaluated. Due to the potentially possible imbalance in intrinsic flows of the various components, the total number of atoms in any slice i (again, per unit area of cross-section) will, in general, be different from the available number of lattice sites as computed from the thickness of the slice before the fluxes were allowed to operate.

Therefore, the next step is to create/annihilate lattice sites in this slice to restore it to the original number of sites per unit volume. Since the cross-section is being held constant (at unity), this requires that we re-adjust the thicknesses of all the slices, so that their volume is altered to satisfy the requirement that we have the correct number of sites per unit volume¹. Having done this, we recalculate the concentration $(C_k)_i$ for all the components in all the slices.

¹ In this analysis it is assumed that in any given volume element, the creation or annihilation of point defects results in a corresponding lengthening or shortening of that element² and that this process takes care of all of the volume changes that are to be effected. If this is not the case and the volume change is distributed isotopically or is dependent on the composition of the volume element, the computer model would require a small modification to take this into account. However, the meaning of the Kirkendall shifts will become harder to interpret and so this complication is being avoided at this stage. It must be stressed that this assumption is not peculiar to this analysis and is, in fact, implicit in all analyses of the Kirkendall effect starting with that of Darken.¹⁹ Further, the assumption is not pivotal to this approach as it is in the traditional studies of diffusion.

This takes us back to the starting point where these new values are input again (looking up the new values of $(\Gamma_k)_i$, if necessary) into equation (7.2). The process is repeated for the desired number of iterations. At the end of each time step, the computer evaluates the concentration as a function of position for that time. The final values of the position of slice i (which allows us to calculate the Kirkendall Shift for that slice), as well as the concentration of the various components at this point (which allows us to draw the concentration-penetration profiles, as well as, if we so choose, the composition paths of the couple) are the output of the program in a tabular form. In this study these tables were imported into Lotus 1-2-3[®] for the purpose of generating graphical representations.

The Input

Basically, there are three different kinds of input, and these are discussed below.

Material Parameters

Before setting up the problem, one has to choose suitable values for (1) the jump distance, δ , (2) the anisotropy factor, α , and (3) the atomic volume, ω . This last piece of information is used to convert the atom fractions to concentration (atoms per unit volume) and vice versa. With trivial adjustments in the program, the simulation can accept

variable values for these parameters. However, as stated elsewhere, the purpose of this study is not to ask complicated questions, but to set up a suitable forum where such questions may be asked. Consequently, throughout this study, 'typical' values were assigned to these parameters, which are as follows. The material is assumed to be isotropic so that α is $1/6$; the jump distance is a typical lattice parameter value, namely 3 angstrom units or $3 \times 10^{-4} \mu\text{m}$; and the atomic volume is taken to be $(3 \text{ \AA})^3$ or $2.7 \times 10^{-11} (\mu\text{m})^3$.

Experimental Design Parameters

Within the constraints presented by the choice of the material parameters above, after playing around with various numbers, it was decided that the semi-infinite couple be sliced into 120 slices on each side of the original weld interface, each with a thickness of $2 \mu\text{m}$. The original weld interface also serves as the origin of the x-axis, with all x's to the left being negative and those to the right being positive. There are certain exceptions to this setup, particularly regarding the number of slices, and these will be pointed out as they are discussed. It was also determined from these preliminary runs that a time increment of 10 seconds was compatible with the rest of the choices. Finally, the jump frequencies, which really belong to the third category of input described below, have to be in the range of 10^5 to 10^7 jumps/second. Once again there is nothing

sacrosanct about these numbers and they can be varied within wide limits. The reason for the existence of these limits is apparent when one considers the fact that for the continuum approximation to apply, the jump distances have to be small compared to the slice widths, but not so small that the process is too slow. Similarly the time increment values are tied to the order of magnitude of the jump frequencies. For a given application, where the correct figures are known for the material parameters, these experimental parameters can be appropriately adjusted to produce a viable algorithm for generating simulated diffusion data.

Run Specific Parameters

Finally we come to the parameters that are specific to the particular simulation run. In principle, as far as the program is concerned, one could input any arbitrarily chosen initial distribution of the atoms of the various species. However, except for the very first simulation presented in this chapter, the following strategy has been adopted. All diffusion couples are made up of two cylindrical pieces of two different alloys, welded together at one of their flat faces prior to the diffusion anneal. In this case, in order to generate the initial concentration profiles, the input consists of the atom fractions of the species at the start for both sides of the couple (i.e., the terminal compositions) which are then converted by the program into concentrations;

and the jump frequencies along with their concentration dependence, if any. The concentration dependence of the Γ 's can be input either in the form of an algebraic relationship or in the form of a look-up table.

The Setup

Armed with the algorithm and the input parameters, we are now in a position to set up the simulation problem, along the lines described above, starting with the simple case of self-diffusion of tracer atoms followed by binary isomorphous diffusion, the ternary couple AB-BC, that was discussed in chapter 5 and, finally, an example of "uphill" diffusion in a system involving dilute solutions of two alloying elements, one substitutional and one interstitial. This last simulation is modelled after the famous Darken's experiment²⁴ involving the diffusion of carbon in austenitic steels.

The Simulation of Tracer Diffusion

One of the simplest cases of diffusion study is tracer diffusion. In this experiment, a wafer of the radioisotope of the same atomic species (whose tracer diffusivity is desired) is sandwiched between two slabs of the non-radioactive material. During the diffusion anneal, the tracer atoms will jump (i.e., undergo vacancy-atom interchanges), exchange places with the normal atoms and, in consequence, will redistribute themselves after the diffusion anneal. By way of

illustrating the efficacy of the computer simulation program, this problem was studied as a preliminary to the more complex cases to follow. The PASCAL program used in this case is presented in the appendix, and the results of the simulation are presented in figure 6.01.

In this particular simulation, a thin layer (2 slices or 4 μm wide) of a high concentration of tracer atoms (3.7×10^{22} atoms per cubic centimeter) is sandwiched between two slabs (each 100 slices or 200 μm thick) of pure metal consisting of the non-radioactive isotope. Thus, the tracer concentration starts out as a step function, and after diffusion for 10000 seconds (1000 iterations) assumes the bell-shaped distribution as shown in figure 6.01. The tracer atom concentration is more than a magnitude lower at its original position and the profile exhibits a Gaussian functional form on either side of this maximum.

The Kirkendall Effect in Binary Isomorphous Diffusion

As discussed earlier in this chapter, when there is an imbalance in the fluxes into and out of a given slice (volume element), there will be a volume change associated with this slice. In the case of the tracer diffusion experiment described above, the jump frequencies, and hence the fluxes were the same for both the tracer and normal atoms. In such a situation no lattice adjustments due to flux imbalances are involved.

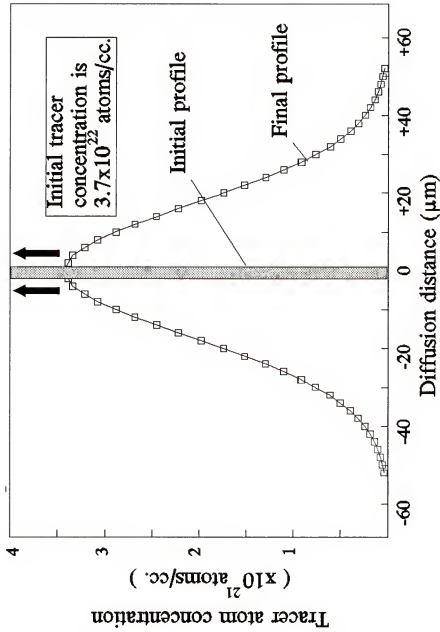


Figure 6.01: The redistribution of tracer atoms after a simulated diffusion anneal for 10000 seconds. The tracer atoms, whose jump frequency is 10^6 jumps/sec, were originally placed as a thin film between two slabs of pure metal.

Let us now consider a case where the jump frequencies of the diffusing species are not equal. Imagine a simple binary diffusion couple of pure 'A' (on the left hand side of the couple) versus pure 'B' (on the right hand side). Further, let the A-B alloy system be isomorphous, i.e., there are no limits on the solubility of A in B or vice versa. Also, let 'A' move faster than 'B' ($\Gamma = 10^7$ versus 10^6 sec^{-1}). In this case, more 'A' crosses the initial boundary (the original weld interface where the inert markers are located) than 'B'. Consequently the markers would be expected to move to the left. The program used for this simulation is presented in the appendix.

During the course of the simulation, the thickness of the slices is adjusted at the end of each time step. In consequence, the *position of any given slice also changes*, since this position for any given slice i is calculated as the sum of the thicknesses of all the slices up to and including this slice i , as measured from either end of the couple, outside the diffusion zone. In these simulations, the distances are by convention measured from left to the right, with the origin located at the original weld interface. Note that this origin is coincident with the Matano interface, discussed in chapter 3, as long as there are no volume changes due to mixing. Thus, the x_i of the first half of the slices (whose initial concentrations are that of the left hand side alloy, in this case pure A) are negative, while those of the

second half are positive. These x_i values change as diffusion progresses, and at the conclusion of the simulation, a Δx_i value can be extracted for each slice i . By convention, these Δx_i values are taken to be positive if the shift is to the right of the initial position of the slice and negative otherwise. These Δx_i values are the *Kirkendall shifts* for the various slices. The entire list of the values of these shifts constitutes the *Kirkendall shift profile*. This profile can be graphed against the final position of the slices.

The simulation was carried out for a total of 1024 iterations (10240 seconds), with the quantities of interest extracted at the end of 8, 16, 32, 64, 128, 256, 512 and 1024 iterative steps. These quantities are:

- (i) the current values of x_i corresponding to each slice i ,
- (ii) the concentration values as a function of these x_i values,
- and (iii) the difference Δx_i , between the current and the initial value of x_i which is the Kirkendall shift associated with the slice i .

Figures 6.02 and 6.03 show the concentration-penetration profiles, plotted as atom percent component A versus the diffusion distance, i.e., the current values of x_i . The maximum depth of penetration, in these figures that contain curves for eight different annealing times, progressively increases with time.

Figure 6.04 and 6.05 show the corresponding Kirkendall shift profiles, once again plotted for the various annealing times, against the current values of x_i . Notice that this

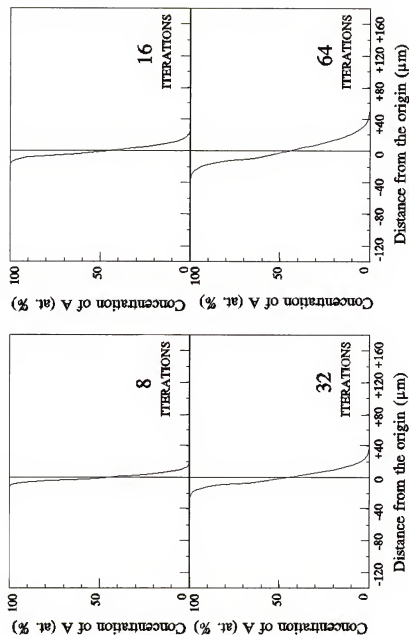


Figure 6.02: The concentration-penetration profiles as a function of iterative steps in simulation, for a pure A-B couple, with $\Gamma_A = 10^6$ and $\Gamma_B = 10^5$ jumps/sec. These profiles coincide when the x-axis is suitably normalized (see figure 6.06).

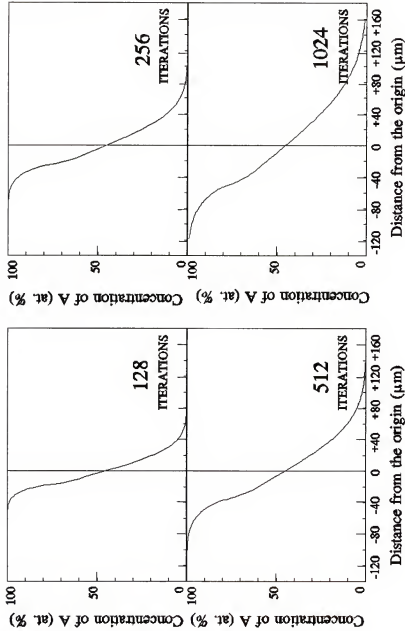


Figure 6.03: The concentration-penetration profiles as a function of iterative steps in simulation, for a pure A-B couple, with $\Gamma_A = 10^6$ and $\Gamma_B = 10^5$ jumps/sec. These profiles coincide when the x-axis is suitably normalized (see figure 6.07).

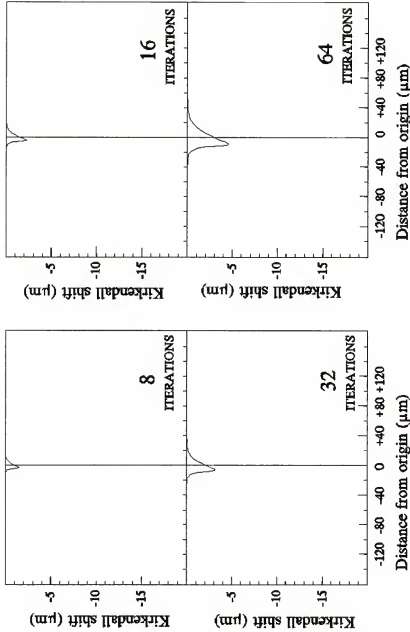


Figure 6.04: The Kirkendall shift patterns as a function of iterative steps in simulation, for a pure A-B couple, with $\Gamma_A = 10^6$ and $\Gamma_B = 10^5$ jumps/sec. These profiles coincide when both axes are suitably normalized (see figure 6.08).

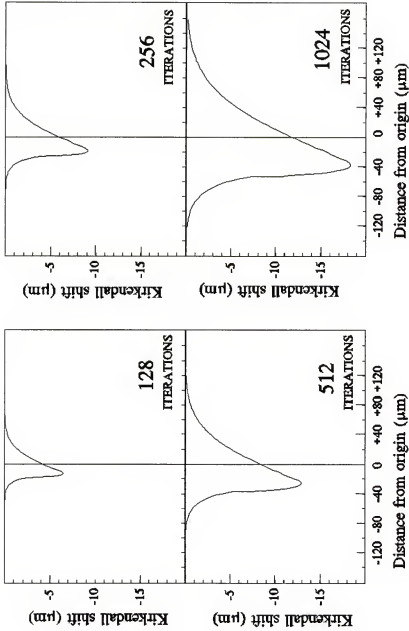


Figure 6.05: The Kirkendall shift patterns as a function of iterative steps in simulation, for a pure A-B couple, with $\Gamma_A = 10^6$ and $\Gamma_B = 10^5$ jumps/sec. These profiles coincide when the x-axis is suitably normalized (see figure 6.09).

shift starts out at zero on the left, becoming more negative toward the center of the couple, until it reaches a maximum negative value. It then once again decreases in magnitude until it vanishes at the far right of the couple. Throughout this work, a shift to the right will be regarded as positive by convention. In this particular case, the shifts are negative simply because the A atoms, which diffuse from the left hand side to the right hand side of the couple, have a higher jump frequency than the B atoms, and leave behind a greater number of unoccupied lattice sites that have to be adjusted for by shrinking the lattice toward the A-rich side. As would be expected, the lattice shifts are confined to the diffusion zone and progressively increase in magnitude as the annealing time increases.

Due to the nature of the problem, since accumulation or depletion in any given volume element is controlled by the divergence of the flux in that element, it is possible to *normalize* the x-axis so as to make all the penetration profiles coincide. To accomplish this, invoke a variable $\lambda = x/t^{1/2}$, where x is the distance from the origin and t is the annealing time. When the concentrations are plotted against λ , *all the profiles are identical, regardless of annealing time*, after a brief transient portion. This fact is graphically illustrated in figures 6.06 and 6.07. The obvious advantage of such a representation of the data is that it allows the researcher to compare the profiles from different

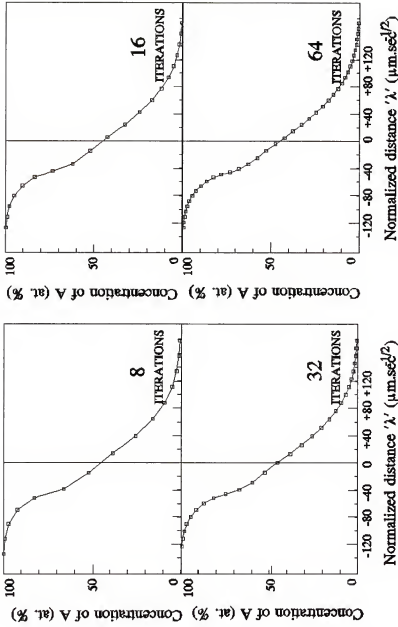


Figure 6.06: The penetration profiles plotted against normalized diffusion distance (distance over the square root of annealing time), for the same data as figure 6.02. Note that the curves are coincident and that the number of points increases with annealing time.

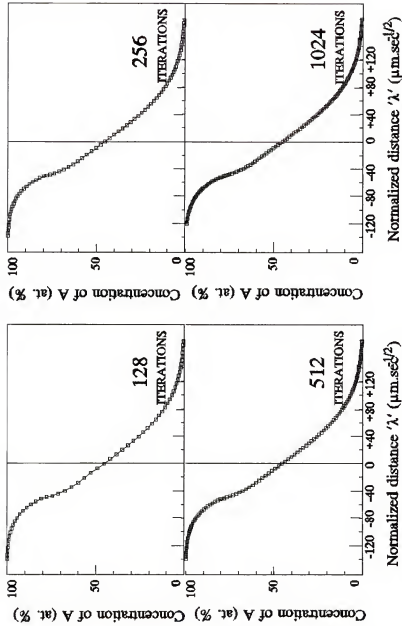


Figure 6.07: The penetration profiles plotted against normalized diffusion distance (distance over the square root of annealing time), for the same data as figure 6.03. Note that the curves are coincident and that the number of points increases with annealing time.

annealing times without having to contend with the latter as a variable. Incidentally, these figures also serve to demonstrate that the transition time (i.e., the number of iterations) required for the computer program to settle down to a reliable pattern seems to be fairly short (fewer than eight iterations!) for this particular simulation.

In the case of the Kirkendall shift profiles, the y-axis, which is also a distance measure, must be divided by the square root of time as well, in order to produce a time-invariant profile. This is illustrated in figures 6.08 and 6.09. Several conclusions were reached by studying this simulation. These conclusions, which are enumerated below, will serve as guidelines in all the other simulation programs studied from this point on.

(1) The transient portion of the simulation is short-lived and therefore an annealing time of 6000 seconds (which corresponds to 600 iterations) has been chosen as optimum. Actually, the longevity of the transient portion is sensitive to the *total number of jumps*, (Γ_{xt}), and the values of Γ 's in the simulations to follow are in the range of 10^5 to 10^7 jumps per second.

(2) Since the time-invariance of the profiles is apparent, all concentration-penetration profiles presented from here on will be plotted against the parameter λ rather than x .

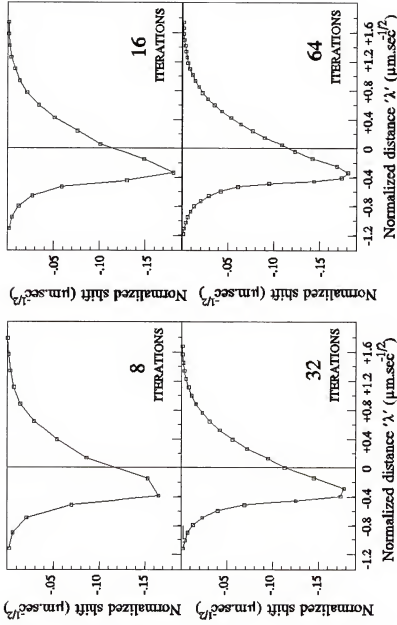


Figure 6.08: A replot of figure 6.04, except that both axes are normalized by dividing by the square root of time. Note that the number of points increases with iterations, smoothing out the otherwise coincident curves.

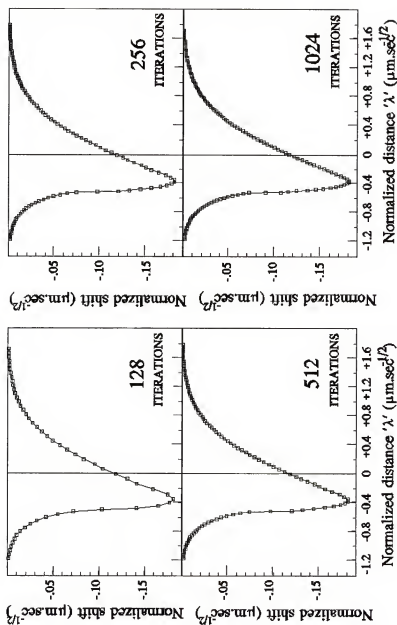


Figure 6.09: A replot of figure 6.05, except that both axes are normalized by dividing by the square root of time. Note that the number of points increases with iterations, smoothing out the otherwise coincident curves.

(3) In the case of the Kirkendall shift profiles, *both axes are normalized* in order to yield a time-invariant pattern.

(4) Conclusions (2) and (3) imply that when expressed in terms of λ , any given relative lattice velocity is tied to a particular composition value in the couple.

Simulation of Diffusion in Ternary Isomorphous Systems

We now extend the capabilities of the computer simulation program to ternary isomorphous systems. The major difference between this and the binary system is that the program output now contains, in addition to the concentration-penetration profiles, the *composition path* traversed by the couple across the Gibbs triangle representing the ternary isotherm. This path is simply the *sequence of concentrations* found in the penetration profiles. Although it suppresses information, this representation of the diffusion data in terms of the composition path is compact, useful and instructive as already pointed out in chapter 5 and as will become evident in the later chapters.

The 50-50 AB/BC Couple

The interesting case of a diffusion sandwich made with a 50-50 alloy of components A and B, coupled with a 50-50 alloy of B and a third component C, in a ternary isomorphous system, was discussed at some length in chapter 5. There, an RPT

model was used to simulate diffusion and generate profiles and paths. Here, we use the same couple to illustrate the JFA modelling technique. For this simulation, A was chosen as the fast-moving species ($\Gamma = 10^7 \text{ sec}^{-1}$), C as the slow moving species ($\Gamma = 10^6 \text{ sec}^{-1}$) and B as being intermediate ($\Gamma = 5 \times 10^6 \text{ sec}^{-1}$).

Figure 6.10 is the time-invariant concentration penetration profile for the three components plotted together. Notice that the profile for component B undulates, even though there was no gradient in B initially. Furthermore, the penetration of A is greater than that of C, as would be expected from the input values of Γ .

Figure 6.11 shows the Kirkendall shift of the lattice. Since the time-invariant profile is obtained, as explained earlier, by dividing both axes by the square root of time, the shape of the curve remains unaffected. Therefore, this figure shows both the raw output of the computer, which is easier to read, and the time-invariant profile by the simple expedient of relabelling the axes of the same graph. In future, whenever the lattice shift profiles are plotted, only the time-invariant axes will be used. These Kirkendall shifts, as already noted, are the result of imbalances in intrinsic fluxes/flows.

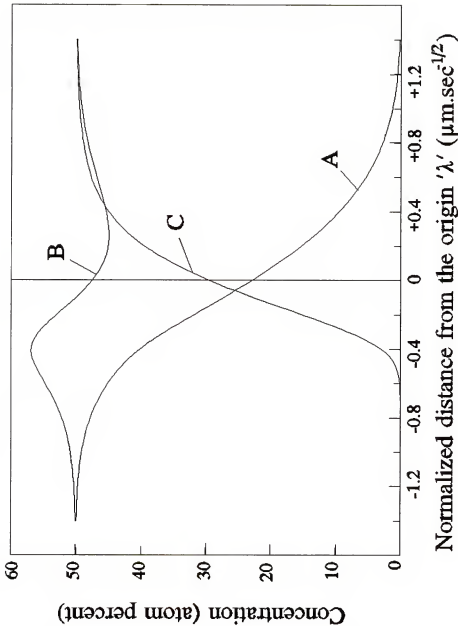


Figure 6.10: Concentration penetration profiles obtained by computer simulation of diffusion in a AB/BC ternary diffusion couple. Note the undulation in the profile of component B, even though there was no gradient in its concentration, across the two sides of the couple, at the outset.

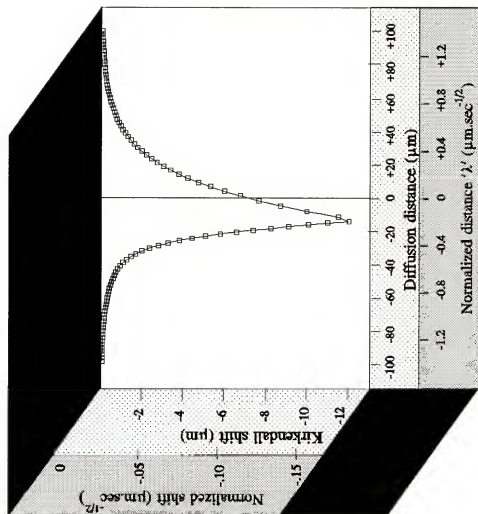


Figure 6.11: The Kirkendall shift pattern for the AB/BC couple. The axes labelled in the inside boxes are the raw data from the simulation, while the axes labelled outside are the normalized values, obtained by dividing the distance measures by the square root of time.

Figure 6.12 is a plot of the *composition path*. As was explained in chapter 5, it is seen that the atoms of species B have redistributed themselves, despite starting with no gradient in their concentration from one side of the couple to the other. Further, all the qualitative observations made by Wan⁸ for his RPT model also hold true in the JFA model. These observations include the fact that the composition path points away from the fast moving species at the end where that species is rich, and points toward that same species at the other end of the couple. The middle segment of the path is controlled by the slow mover and is rotated toward that corner. The main difference between this composition path and the one generated by the RPT model is that the JFA path is continuous and was generated from simulated concentration penetration profiles that are also continuous.

One other point of interest is that the *cross-over point*, i.e., the point at which the composition path crosses the line joining the end-point compositions. In the RPT model, when the penetration tendencies are composition independent, by virtue of the geometry of the setup, this cross-over point bisects the line joining the end-point compositions. This is not precisely true in the JFA, because of the continuous nature of the simulation program; as soon as a gradient is established in the concentration of B, the atoms of B start diffusing to counter this gradient. Therefore, except in the

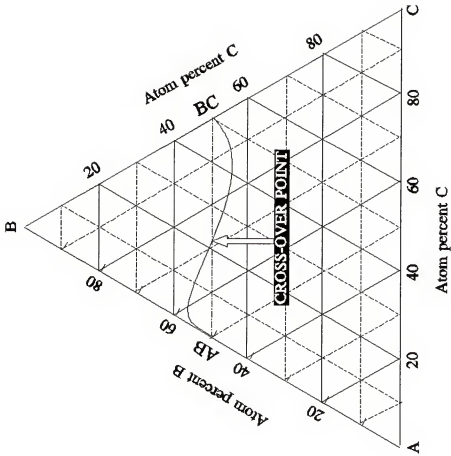


Figure 6.12: The composition path in the AB/BC couple, plotted on the Gibbs triangle representing the isotherm. A is the fast mover ($\Gamma_A = 10^7 \text{ sec}^{-1}$), C is the slow mover ($\Gamma_C = 10^6 \text{ sec}^{-1}$) with B intermediate ($\Gamma_B = 5 \times 10^6 \text{ sec}^{-1}$). As a result, the path points away from the A-corner of the triangle at the AB end of the couple and toward the A-corner at the BC end.

unrealistic scenario where $\Gamma_B = 0$, the cross-over point will not coincide with the mid-point mentioned above. However, when a composition dependence is introduced, this point will *shift toward the fast corner*, i.e., where all the components are faster than they are elsewhere. Figure 6.13 illustrates this point. For the purpose of generating this figure, a composition dependence of Γ 's as illustrated in figure 6.13 (a) was input. In chapter 9, where comparisons of the JFA model are made with experimental data, these Γ 's are modelled as being concentration dependent. Consequently, the cross-over point shifts from the mid-point. The study of these *cross-over shifts* is potentially a valuable clue to understanding the composition dependence of the kinetic parameters.

The program used for this simulation run is presented in the appendix. With minor modifications (such as the elimination or inclusion of some READ/WRITE statements), this program is essentially the same as the one used to study patterns of behavior in isomorphous systems, presented in chapter 8.

"Uphill" Diffusion - Darken's Experiment

In 1949, shortly after his famous analysis of the Kirkendall effect, Darken²⁴ published the results of a remarkable experiment in which he demonstrated that diffusion can occur *against* a concentration gradient in apparent

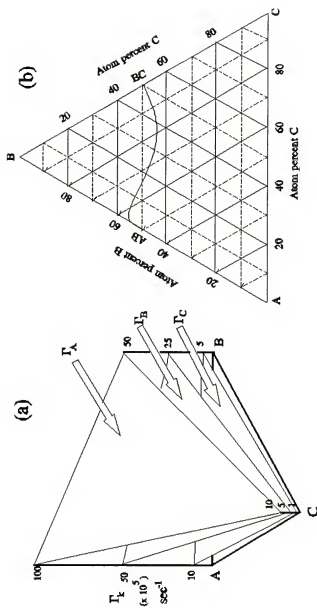


Figure 6.13:

Illustration of the shift in the cross-over point due to the composition dependence of the jump frequencies. The Γ 's of the three components vary along the planes shown in (a), so that all species move the fastest in the A-corner and the slowest in the C-corner. As a result, the cross-over point (where the path intersects the line joining the end-point compositions), shifts toward the A-rich (AB) end of the couple. Compare with figure 6.12.

violation of Fick's first law. This paper represents a milestone in diffusion research, both because of the startling nature of the experimental results and because of the elegance of Darken's explanation for them.

Darken studied diffusion of interstitial carbon in a semi-infinite couple made of two steels with approximately the same carbon content but containing significantly different amounts of a substitutional alloying element, namely silicon. After an anneal for 1050°C for two weeks, during which time there is practically no diffusion of silicon, he observed a sharp decrease in carbon content close to the original weld on the silicon-rich side and a corresponding hump in the carbon profile on the silicon-poor side. Apparently, carbon had diffused "uphill", i.e., from a region of low carbon content to a region with more carbon.

Darken attributed his results to the higher thermodynamic activity of carbon in the presence of silicon. Using thermodynamic data in the literature, he demonstrated that after diffusion, the chemical potential of carbon was indeed uniform throughout the diffusion zone. Thus, the following equation better describes the carbon flux than Fick's first law.

$$J = -M \cdot \frac{\partial u}{\partial x} \quad (6.03)$$

Here the flux is proportional to the mobility, M , times the chemical potential gradient.

While the validity of Darken's analysis is beyond reproach and has therefore withstood the test of time, the question arises as to whether or not it is possible for a system that obeys equation (6.01) to behave as carbon does in Darken's experiment. In other words, if the jump frequency of carbon is made to depend on the silicon concentration, is it conceivable that the second term in the derivative $[\partial(C.F)/\partial x]$ will be large enough to cause the carbon flux to go against the concentration gradient?

The results of a simulation program designed to test the above question are presented in figure 6.14, along with the original experimental data points of Darken and the curve calculated by Kirkaldy and Young.¹⁶ Since carbon is an interstitial, its contribution to the volume changes were deemed negligible in this particular simulation. Other details of the program are also presented in figure 6.14. A copy of the program can be found in the appendix. Although a quantitative agreement is still being sought at this writing, it is obvious from figure 6.14 that carbon does diffuse "uphill" in the computer model. Thus, even though Darken's results invalidate the application of Fick's first law to this experimental situation, Dehoff's reformulation (equation 6.01) remains viable.

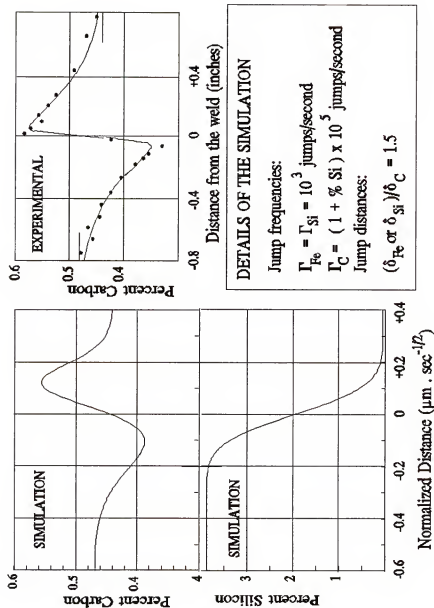


Figure 6.14: Jump frequency model for the uphill diffusion of carbon in steel containing silicon. The top right figure shows the data points obtained by Darken¹⁶ as well as the curve calculated by Kirkaldy and Young.²⁴

Computer Modelling of Diffusion

The difficulties encountered in making finite difference calculations based on the Traditional Fickian Approach (TFA) are perhaps best expressed by Chow and Houska, who comment:

Finite difference calculations have been the only means of obtaining profiles for this more general case of both a time dependent surface and a diffusion coefficient that varies with concentration. Although this approach is capable of giving numerical results, *the computer time can approach actual diffusion times* [italics added]. These excessive computer times are required to assure that the calculations converge to the proper values and are stable.³⁷

Many researchers make various simplifying assumptions before venturing into a computer simulation of the diffusion process. Often, while these assumptions serve to simplify the mathematics, they are a far cry from reality. For instance, it is often assumed that the intrinsic diffusion coefficients are constant. Anusavice's work²² on tracer diffusion in the Cu-Ni-Zn system is just one example that serves to invalidate the constant diffusivity assumption. He found that the tracer diffusivities varied by *several orders of magnitude* across the composition range studied by him. By contrast, the starting assumptions of the JFA model are straightforward, with only one kinetic descriptor for each component at each composition as opposed to the menacing matrices of diffusivities that are sought by the researchers using the traditional Fickian Approach (TFA). Perhaps, in

this consequence, the JFA might be able to, as DeHoff⁵⁶ notes, "provide a springboard to a detailed and sophisticated statistical description of diffusion in flowing systems" {page 611}.

The JFA Versus the TFA

The traditional Fickian approach (TFA) suffers from the many failings already discussed in the previous chapters. In addition to all those shortcomings, it seems a ridiculous waste for the researcher to produce the entire concentration profile, only to use a few points in it (where its composition is the same as that of another diffusion couple, the rest of whose concentration profile is also thrown away). It is a much better idea to compare the entire concentration profile generated in the JFA approach to the actual experimental profile. This situation is somewhat reminiscent of studies in the kinetics of coarsening, where the researchers produce histograms of particle size distribution, and then proceed to use only the average value to compare experiment to theory, as, for example, in the classic work of Ardell and Nicholson.⁵⁸ Once again, it must be emphasized that the JFA approach enables studies of *patterns of behavior in a compositional region of interest*, while the TFA produces a matrix of *diffusion coefficients at specific points that cannot even be preselected*. Furthermore, the kinetic descriptors generated by JFA are the 'effective mean jump frequencies' which have a

straightforward physical basis, while, except in the simplest cases, the matrix of diffusion coefficients are quantities whose relevance to the physical world is less obvious.

Another point worth noting is that the approach presented in this chapter can easily be extended to isomorphous systems with four or more components. All that is required is a slight modification in the computer program. This situation is in sharp contrast with the traditional approach where the reconciliation of theory with experiment is all but impossible when there are four or more components in the system. By way of illustrating this point, a simulation program was written (see appendix) for the 50-50 AB/CD quaternary couple. The composition path obtained as a result of this program, shown in figure 6.15, is a space curve in the isotherm which is now a tetrahedron.

The JFA versus the RPT modelling

The jump frequency approach has several advantages over the relative penetration tendency approach. For one thing, the model does not conjure up flows approximated as being linear in a concocted rigid lattice space. Instead, the quantities and the processes involved in the modelling are physical meaningful entities. For another, the JFA model produces, as output, the entire concentration penetration profile along with the lattice velocity profile throughout the diffusion zone, from which other quantities may be derived for

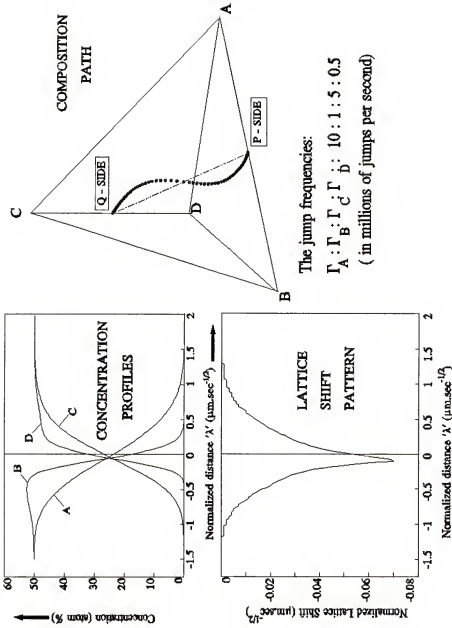


Figure 6.15:

Computer simulated diffusion in a quaternary isomorphous system. This example shows the concentration profiles, the Kirkendall shift pattern and the composition path for a diffusion couple made of the 50-50 A/B binary alloy on one side and a 50-50 C/D binary alloy on the other. The composition path is a space curve in the quaternary isotherm, which is a tetrahedron.

all annealing times. On the other hand, the RPT model only reports these derived quantities, namely the composition paths, the crossover shifts, the Kirkendall shifts etc., for a particular time in the diffusion process (although it is possible to recast the RPT's in terms of λ). Finally, the kinetic descriptors that arise from the JFA model can be related, hopefully directly, to the vigor with which atoms of a given species jump in their environs. On the other hand, the relative penetration tendencies, which are the end-product of the RPT analysis, have no such obvious connection to the physics of the process.

Concluding Remarks

In summary, although the RPT approach is novel and in many ways useful, the JFA modelling represents a quantum improvement and deserves closer scrutiny by the community conducting diffusion research.

Having established the viability and robustness of the computer simulation programs using the JFA, we are now in a position to systematically explore patterns of diffusion behavior in ternary isomorphous systems. This is done in the next chapter.

CHAPTER 7
DIFFUSION IN ISOMORPHOUS SYSTEMS - A SURVEY USING THE JFA

Introduction

The efficacy of the jump frequency analysis (JFA) in simulating diffusion behavior in semi-infinite systems was demonstrated in the previous chapter. This chapter seeks to make a systematic survey of *patterns of behavior* in ternary isomorphous systems for various input jump frequencies of the three elements together with their compositional dependence in a manner similar to the work of DeHoff, Anusavice and Wan⁴ based on the relative penetration tendency (RPT) model that was presented in chapter 5.

Following a strategy very similar to the RPT approach, the Gibbs triangle representing the ternary isotherm at the temperature of the diffusion anneal is divided into 8 regions and the diffusion couples are chosen so that the left hand side (P-side) is the $1/3 - 1/3 - 1/3$ ternary alloy and the right hand side (Q-side) is the unary/binary alloy that represents eighteen couples, chosen in the middle of these regions and the boundaries between them. Figure 7.01 illustrates the isotherm divided into the eight regions along

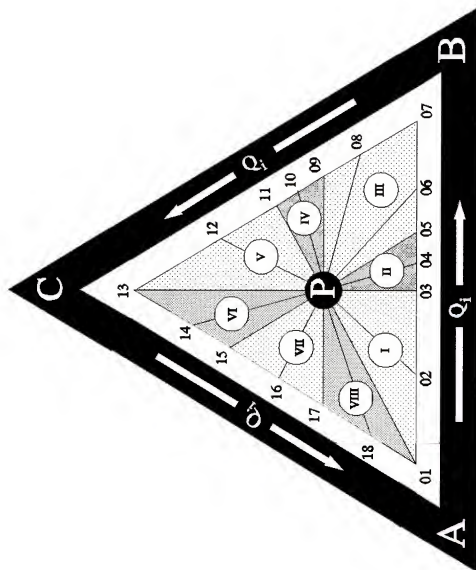


Figure 7.01: The ternary isotherm for the isomorphous system A-B-C, divided into 8 regions (roman numerals) for the purpose of surveying diffusion behavior by simulation. The 18 end-point compositions (Q_i) around the triangle are coupled with the 1/3-1/3-1/3 alloy (P) in the middle.

with the eighteen couples chosen for the survey, with the appropriate couple number designation, while table 7.01 lists the compositions of the right hand side (Q-side) of the couples involved.

The two key factors that affect the output of the simulation are: (A) the ratio of the jump frequencies of the three components, i.e., $\Gamma_A : \Gamma_B : \Gamma_C$ and (B) the manner in which these Γ 's vary with composition. For the purposes of the survey, three different values of Γ 's were chosen as representing *Fast* (10^7 jumps/sec), *Medium* (5×10^6 jumps/sec) and *Slow* (10^6 jumps/sec). This leads to the following four sub-cases as far as the ratio of the three Γ 's is concerned - *Case A*: All Γ 's are equal, $\Gamma_A = \Gamma_B = \Gamma_C = 10^7$ jumps/sec; *Case B*: $\Gamma_A : \Gamma_B : \Gamma_C :: \text{Fast} : \text{Fast} : \text{Slow} :: 10^7 : 10^7 : 10^6$ jumps/sec; *Case C*: $\Gamma_A : \Gamma_B : \Gamma_C :: \text{Fast} : \text{Slow} : \text{Slow} :: 10^7 : 10^6 : 10^6$ jumps/sec; and *Case D*: $\Gamma_A : \Gamma_B : \Gamma_C :: \text{Fast} : \text{Medium} : \text{Slow} :: 10^7 : 5 \times 10^6 : 10^6$ jumps/sec.

The composition dependence of jump frequencies can be introduced in a number of different ways. Here, the strategy adopted is the same as the one used by Wan in his RPT models. If the specifics of a particular alloy system are known, then an appropriate composition dependence can be introduced in the model. The next chapter, where comparison is made with experimental data, utilizes this scheme.

Except for Case (A), the composition dependence of the Γ 's are modelled as being in the same ratio as the Γ 's themselves. That is, all components jump an order of

Table 7.01 : The composition of the Q-side, i.e., the right hand side of the semi-infinite diffusion couples surveyed, spanning the ternary isotherm in the system A-B-C. The P-side, i.e., the left hand side of all these couples is the 1/3-1/3-1/3 ternary alloy. For a graphical representation, see figure 7.01.

Couple #	Atom % A	Atom % B	Atom % C
01	100	0	0
12	75	25	0
03	80	50	0
04	42	58	0
05	33	67	0
16	80	80	0
07	0	100	0
08	0	80	20
09	0	67	12
10	0	58	42
11	0	50	50
12	0	30	70
13	0	0	100
14	20	0	80
15	33	0	67
16	50	0	50
17	67	0	33
18	80	0	20

magnitude more frequently at the fast corner than at the slow corner. This leads to two sub-cases each for the composition-dependence of Γ_k for the cases (B), (C) and (D), and these are designated cases (B_1) , (B_2) , (C_1) , (C_2) , (D_1) , and (D_2) . The subscript '1' is for composition independent Γ 's while the subscript '2' denotes a composition dependence. The composition dependence of the Γ 's for the three sub-cases (B_2) , (C_2) and (D_2) are illustrated graphically in figures 7.02, 7.03 and 7.04 respectively. .

There are thus eighteen simulation runs for case (A) and thirty six simulation runs each for cases (B), (C) and (D). In what follows, case (A) is dealt with first, as there are no complications in this case, such as Kirkendall shifts. The composition paths (in the Gibbs triangle) are presented for this case, followed by the concentration-penetration profiles for all eighteen couples.

Cases (B), (C) and (D) are dealt with by first discussing their composition paths, followed by a *couple by couple* analysis of the concentration profiles and the shift patterns, going from couple # 01 through couple # 18. The discussion that follows deals with points of interest in each of these simulations.

Two computer programs, one written for constant jump frequencies and the other for the case where the jump frequencies are composition dependent are presented in the appendix. All of the simulations presented in this chapter,

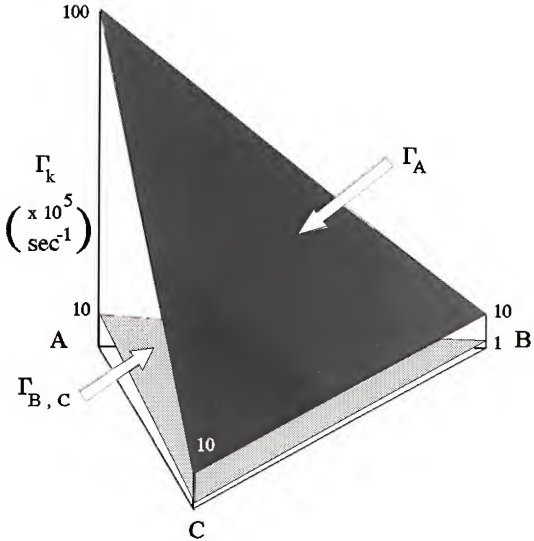


Figure 7.02: Illustration of the composition dependence of the jump frequencies of A, B and C for the case where $\Gamma_A : \Gamma_B : \Gamma_C :: \text{Fast} : \text{Slow} : \text{Slow}$. Γ_A (the top plane) starts out at 10^7 at the A-corner, gradually decreasing to 10^6 at the B-C binary. Γ_B and Γ_C (the lower plane) start at 10^6 at the A-corner, dropping to 10^5 at the B-C binary.

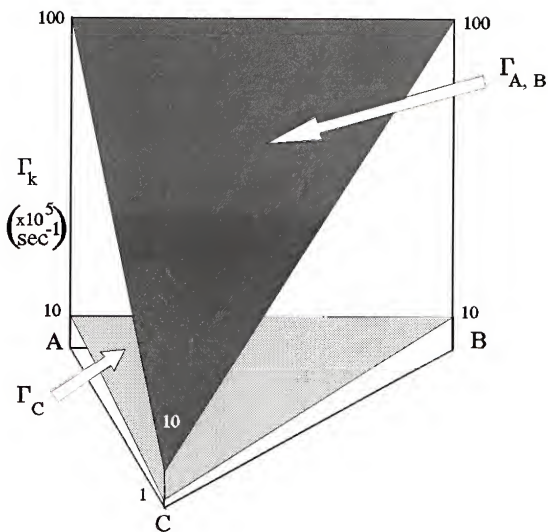


Figure 7.03: Illustration of the composition dependence of the jump frequencies of A, B and C for the case where $\Gamma_A : \Gamma_B : \Gamma_C :: \text{Fast} : \text{Fast} : \text{Slow}$. Γ_A and Γ_B (the top plane) start out at 10^7 at the A-B binary, gradually decreasing to 10^6 at the C-corner. Γ_C (the lower plane) starts at 10^6 at the A-B binary, dropping to 10^5 at the C-corner.

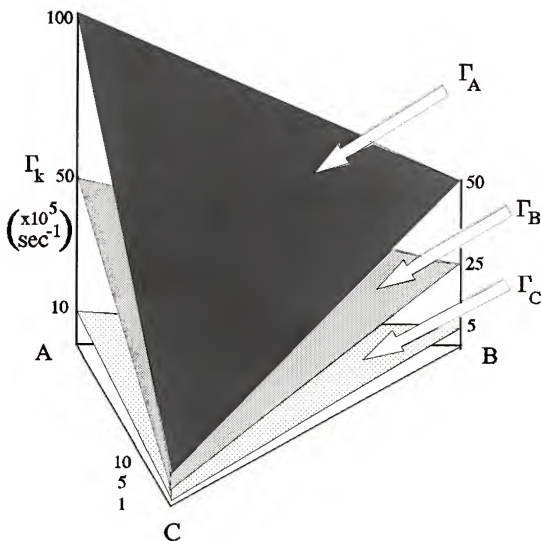


Figure 7.04: Illustration of the composition dependence of the jump frequencies of A, B and C for the case where $\Gamma_A : \Gamma_B : \Gamma_C :: \text{Fast} : \text{Medium} : \text{Slow}$. All three Γ 's (indicated by the three planes) have their highest value at the A-corner, reach an intermediate value at the B-corner and, finally, reach their lowest value at the C-corner.

as well as the next (chapter 8), where comparison is made with published experimental data, are variations of these two programs.

Case (A): All Γ 's Equal and Independent of Composition

As there are no imbalances in the flows of the three components, there is no net lattice velocity and hence no Kirkendall shifts in this case. Further, in the same consequence, the composition paths do not deviate from the line joining the end-point composition. This is evident from the results of the simulation run as depicted in figure 7.05. The concentration-penetration profiles for these eighteen couples are presented in figures 7.06 through 7.08. In these figures, as well as in all other figures that involve diffusion distances and/or lattice shifts in the diffusion direction, these distances/shifts are represented in terms of the parameter λ , which is the distance/shift divided by the square root of time. As noted in Chapter 6, these distances/shifts become proportional to the square root of annealing time so that the concentration-penetration and the Kirkendall shift profiles are time-invariant when expressed in terms of λ . This facilitates comparison between any two profiles regardless of the time of diffusion anneal.

The concentration-penetration profiles presented in figures 7.06 through 7.08 offer no hidden surprises, such as undulations in the concentration of one of the components.

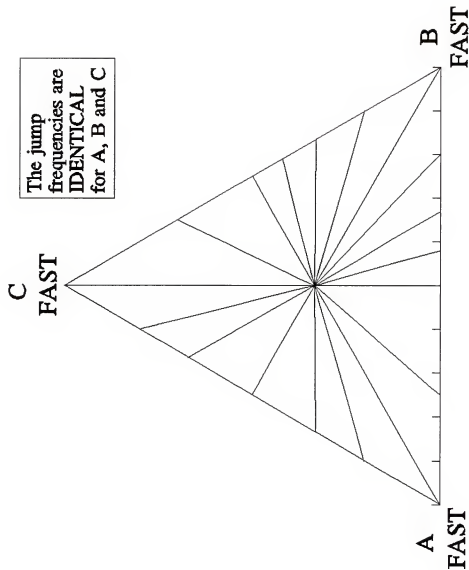


Figure 7.05: The composition paths of the 18 couples simulated, with the Γ 's of A, B and C the same at all compositions. The paths are the same as the line joining the end-point compositions.

Case A (All jump frequencies are identical)
{There is no lattice shift}

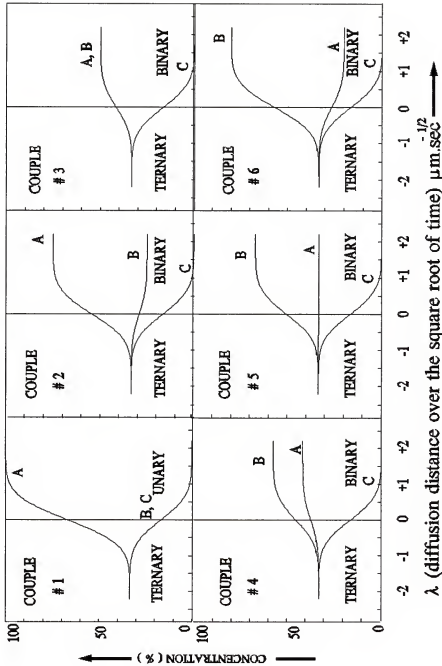


Figure 7.06: The concentration profiles for couples 1 - 6, for the case where the jump frequencies of all three components are the same and independent of compositions {there is no Kirkendall shift}.

Case A (All jump frequencies are identical)

{There is no lattice shift}

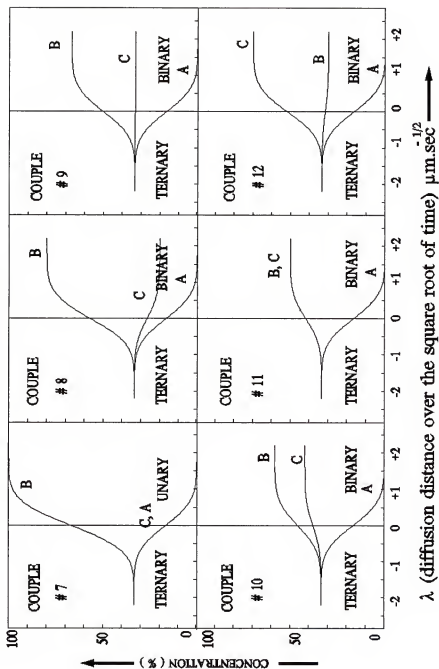


Figure 7.07: The concentration profiles for couples 7 - 12, for the case where the jump frequencies of all three components are the same and independent of compositions {there is no Kirkendall shift}.

Case A (All jump frequencies are identical)

{There is no lattice shift}

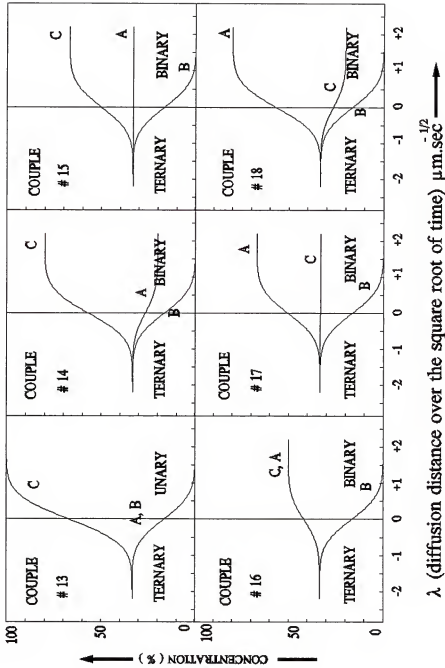


Figure 7.08: The concentration profiles for couples 13 - 18, for the case where the jump frequencies of all three components are the same and independent of compositions {there is no Kirkendall shift}.

However, as will be seen, this is not the case when the Γ 's are different for the three components. Even more interesting things happen when the Γ 's are made to depend on the composition.

Cases (B), (C) and (D)

Composition paths

The next six figures (figures 7.09 through 7.14) are the composition paths for the eighteen couples, first for concentration independent and then for concentration dependent Γ 's, for each of the above cases. The salient features of each of these figures is described below.

Figure 7.09. Here, components A and B are the fast movers and C is slow. As a result, the ends of the composition paths tend to point *toward or away from* the A and B corners, depending upon whether the end-point compositions are *rich or poor* in the fast moving species. This fact is consistent with and gives credibility to the same observation in the RPT approach developed by DeHoff¹ which was presented in an earlier chapter {chapter 5}.

For the sake of clarity, the lines joining the end-point compositions has been omitted in these six figures. However, an inspection reveals that the so called 'cross-over point', i.e., the point at which the composition path crosses the line joining the end-point compositions is closer to the mid-point

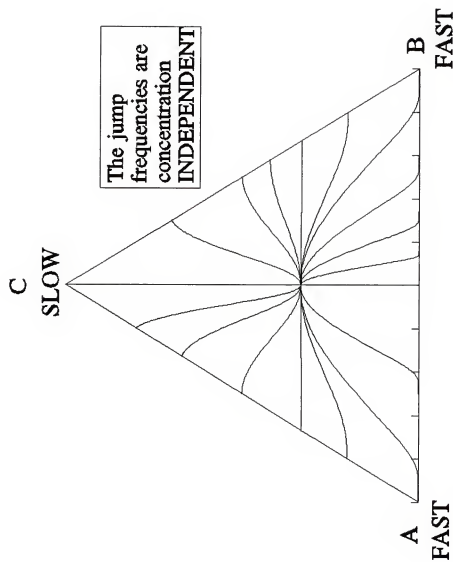


Figure 7.09: The composition paths of the 18 couples simulated, where the jump frequencies are composition independent and are in the ratio $\Gamma_A : \Gamma_B : \Gamma_C :: \text{Fast} : \text{Fast} : \text{Slow}$.

of the latter in this case where the Γ 's are composition independent than for the concentration dependent cases.

Figure 7.10. Once again *A* and *B* are the fast movers compared to *C*, but this time the Γ 's are concentration dependent so that all species move faster at compositions rich in *A* or *B* than at compositions rich in *C*. The same effect as mentioned in figure 7.09 can be seen here, namely that the ends of the composition paths swing away from or toward the fast moving species depending on its concentration at that point.

The cross-over point is shifted away from the midpoint of the line joining the end-point compositions and toward the end-point composition that is rich in the fast moving species. It is the behavior of this cross-over point taken together with the Kirkendall shift data (when available) that gives a valuable clue in modelling the hierarchy of jump frequencies and their composition dependence.

Figures 7.11 and 7.12. In these two cases, component *A* is the only fast moving species. In consequence, there is a pronounced effect on the composition paths which now tend to point toward the *A* corner. Once again, the primary difference between figure 7.11 and figure 7.12 is that in the latter figure, the cross-over point in each composition path is shifted toward the *A*-rich end of the couple.

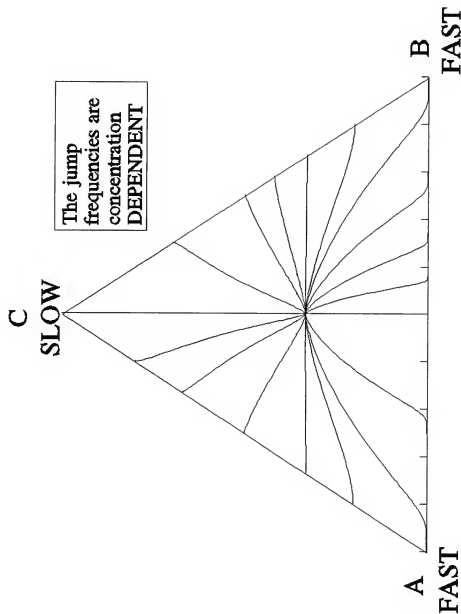


Figure 7.10: The composition paths of the 18 couples simulated, where the jump frequencies are composition dependent and are in the ratio $\Gamma_A : \Gamma_B : \Gamma_C :: \text{Fast} : \text{Fast} : \text{Slow}$.

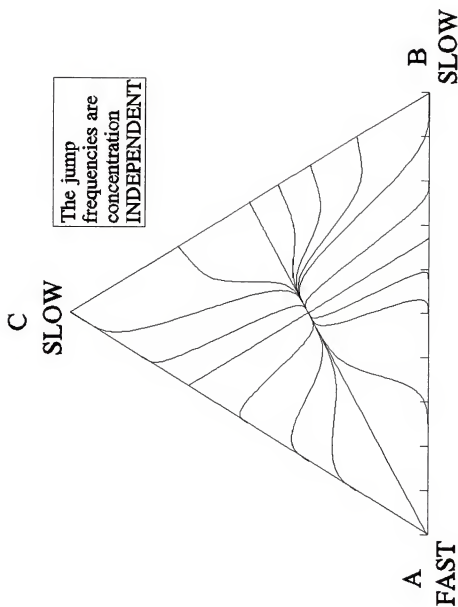


Figure 7.11: The composition paths of the 18 couples simulated, where the jump frequencies are composition independent and are in the ratio $\Gamma_A : \Gamma_B : \Gamma_C :: \text{Fast} : \text{Slow} : \text{Slow}$.

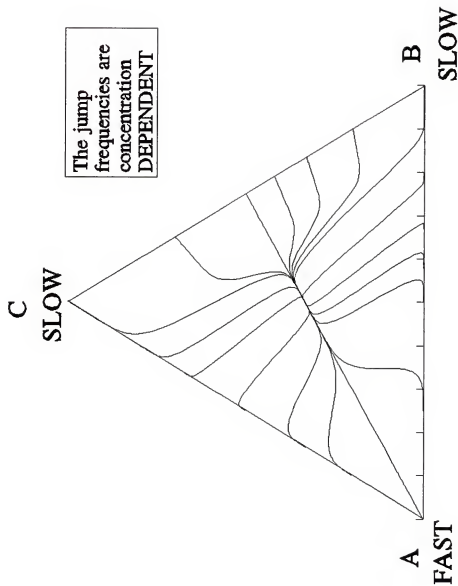


Figure 7.12: The composition paths of the 18 couples simulated, where the jump frequencies are composition dependent and are in the ratio $\Gamma_A : \Gamma_B : \Gamma_C :: \text{Fast} : \text{Slow} : \text{Slow}$.

Figures 7.13 and 7.14. These cases are relatively more complicated in the sense that since all three of the Γ 's are different, the shape of any composition path will depend upon where it is located in the Gibbs triangle. For instance, couple # 1 points directly at the A corner in figures 7.11 and 7.12, whereas in figures 7.13 and 7.14 it bends toward the A-B binary while still pointing toward the A corner. Figures 7.13 and 7.14 are qualitatively the same, except that the cross-over points in figure 7.14 is shifted in the direction of the fast moving species.

Penetration Profiles and Lattice Shifts - The Setup

When the jump frequencies are not all the same, then in general, there will be lattice shifts in the couple to accommodate the imbalances in the intrinsic fluxes of the component species. Therefore, in the above cases, in addition to the concentration profiles, the model also generates a pattern of Kirkendall shifts. For the sake of clarity as well as ease of comparison, these profiles and patterns are produced and discussed below for each of the eighteen couples surveyed taken one at a time. Each figure discussed below represents the results of the simulation runs for one of the eighteen couples and one of the three cases under consideration. Thus there are fifty four figures in all.

Each of the figures 7.15 through 7.68 is subdivided into four figures, with the two sub-figures on the left hand side

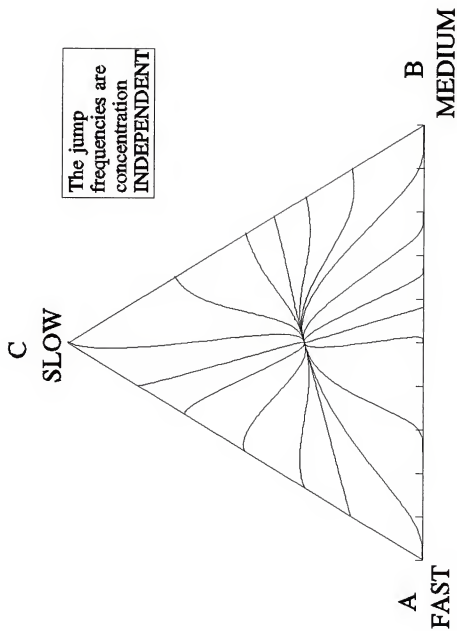


Figure 7.13: The composition paths of the 18 couples simulated, where the jump frequencies are composition independent and are in the ratio $\Gamma_A : \Gamma_B : \Gamma_C :: \text{Fast} : \text{Medium} : \text{Slow}$.

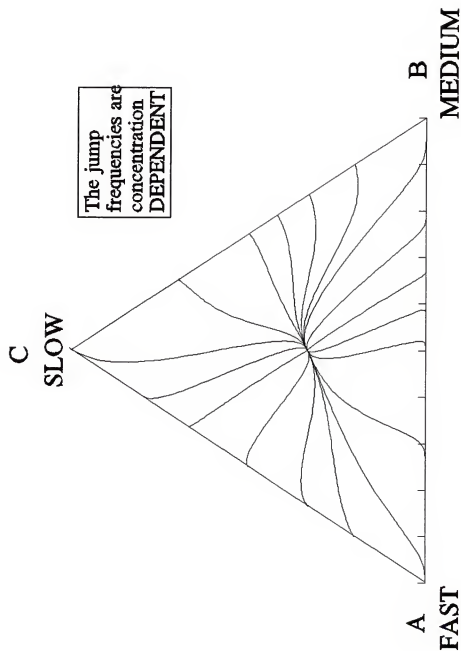


Figure 7.14: The composition paths of the 18 couples simulated, where the jump frequencies are composition dependent and are in the ratio $\Gamma_A : \Gamma_B : \Gamma_C :: \text{Fast} : \text{Medium} : \text{Slow}$.

for constant jump frequencies and the other two sub-figures on the right for the composition dependent jump frequencies. Since each of these figures is for a particular case (B, C or D), every set of three figures depicts the six simulation runs made for a given couple #. In the discussion that follows, these figures are discussed couple by couple, i.e, in sets of three.

While comparing the Kirkendall shift patterns in figures 7.15 through 7.68, it must be noted that the scale of the ordinate changes from figure to figure, depending on the magnitude of the shifts involved. When these Kirkendall shift patterns are all drawn to the same scale, a definite pattern is discernable as one scans around the Gibbs triangle from couple #1 to #18. These shift profiles are presented in the last six figures (figures 7.69 through 7.74) and are discussed towards the end of this chapter.

Concentration Profiles and Kirkendall Shift Patterns

Couple #1 (figures 7.15 through 7.17). It can be seen that in Case (C) [figure 7.16], that the profiles for components B and C are identical. This is due to the fact that B and C are both slow-moving in this model and their mole fractions are the same at the end-point compositions. On the other hand, for case (B₁), where C is the only slow-mover, the profile of C lags behind that of B [figure 8.15]. Case (D), where all three mobilities are different, falls somewhere in

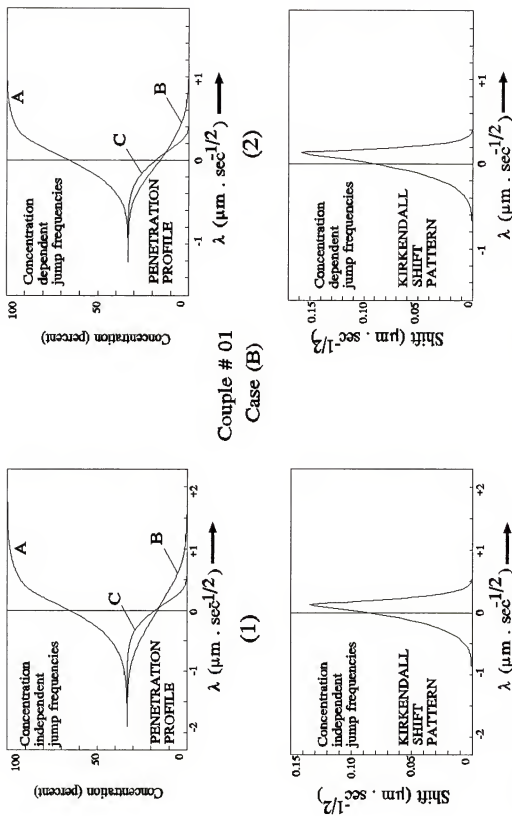


Figure 7.15: The concentration penetration profile and the Kirkendall shift pattern for couple # 01, Case (B), with $\Gamma_A : \Gamma_B : \Gamma_C :: \text{Fast} : \text{Fast} : \text{Slow}$.

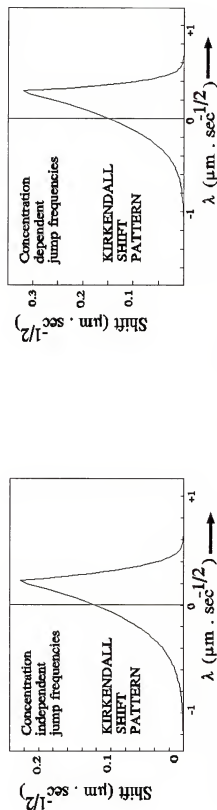
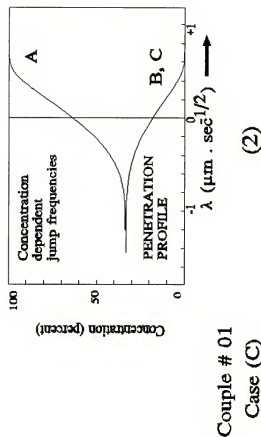


Figure 7.16: The concentration penetration profile and the Kirkendall shift pattern for couple # 01, Case (C), with $\Gamma_A : \Gamma_B : \Gamma_C :: \text{Fast} : \text{Slow} : \text{Slow}$.

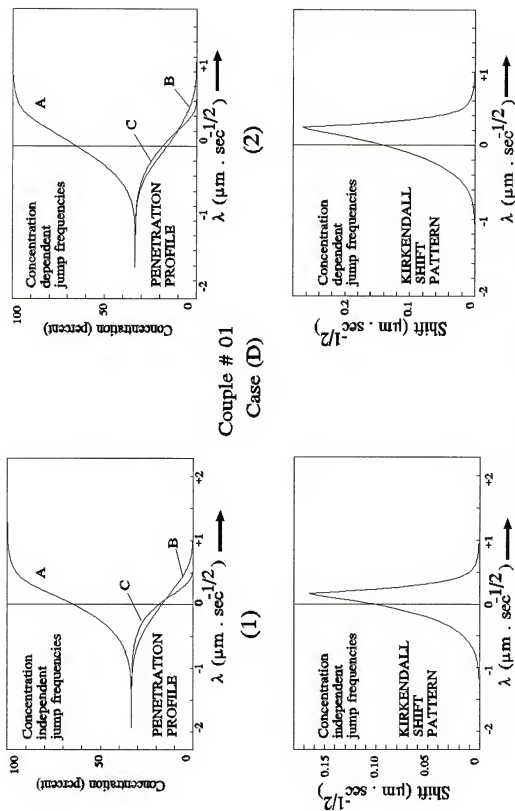


Figure 7.17: The concentration penetration profile and the Kirkendall shift pattern for couple # 01, Case (D), with $\Gamma_A : \Gamma_B : \Gamma_C$:: Fast : Medium : Slow.

between these cases. Regarding the Kirkendall shift profiles in this couple, as well as all the other couples, the shifts are larger (meaning the lattice velocities are faster) for the concentration dependent cases in comparison to the concentration independent cases. Presumably, this is due to the larger changes in the Γ 's due to changes in composition along the diffusion direction.

Couple # 02 (figures 7.18 through 7.20). Here, the profile of B shows an undulation (a wavy part) in all of the cases and is particularly pronounced in case (C_2) [figure 8.19]. This peculiarity is strictly in consequence of the fact that the slow-mover, C , is required to vanish at the Q -side (right hand side of the couple) and is not able to accomplish this as efficiently as the fast-moving species. As a result, the lattice shifts are significant enough to produce the undulation in the profile of B . Translated into the composition path description, this undulation (which can also be seen to a lesser extent in the profile of A) in case C_2 leads to a region where the composition of the fast moving species is nearly constant. In chapter 8, this phenomenon is noted in the behavior of Zn in the $Cu-Ni-Zn$ system⁸.

Couple # 03 (figures 7.21 through 7.23). For case (B), the A and B profiles are identical. This is similar to case (C) in couple # 01. As explained earlier, the profiles are the same because the mobilities are not any different and the end-point compositions are the same for both of these

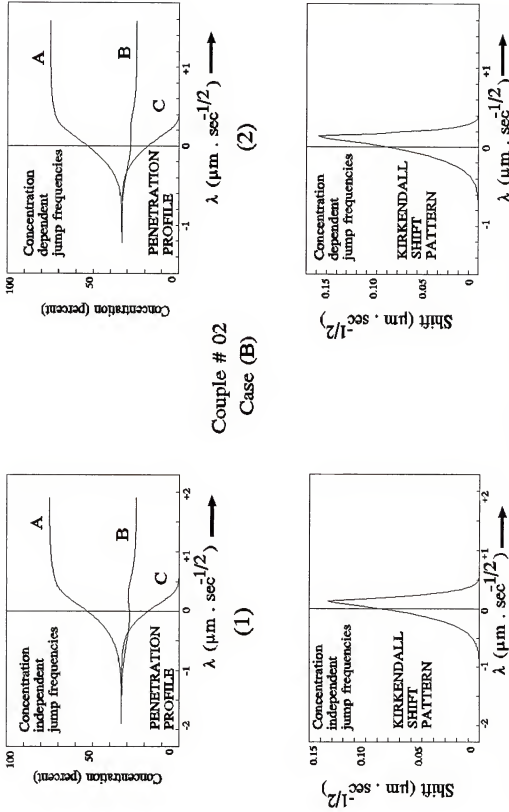
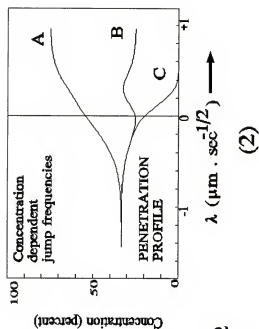


Figure 7.18: The concentration penetration profile and the Kirkendall shift pattern for couple # 02, Case (B), with Γ_A ; Γ_B ; Γ_C : Fast; Fast; Slow.



Couple # 02
Case (C)

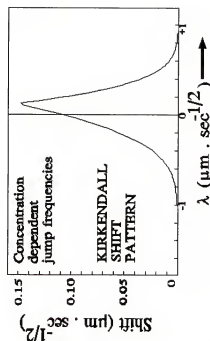


Figure 7.19: The concentration penetration profile and the Kirkendall shift pattern for couple # 02, Case (C), with Γ_A : Γ_B : Γ_C : Fast : Slow : Slow.

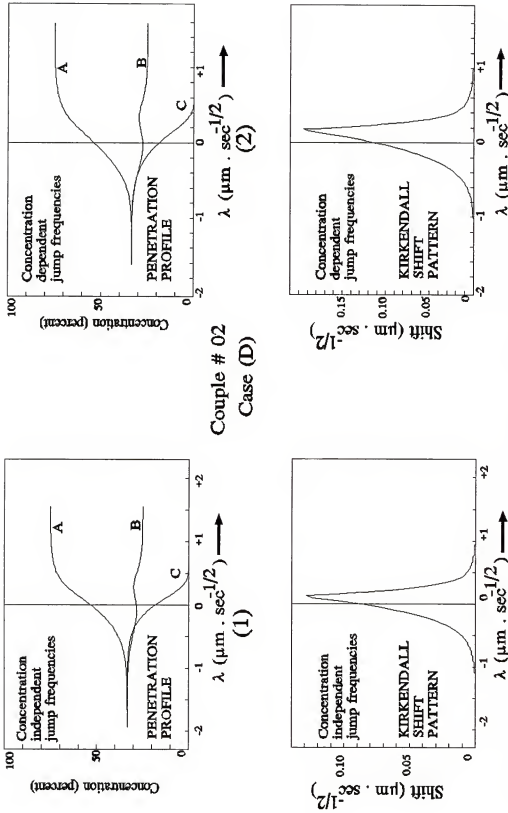
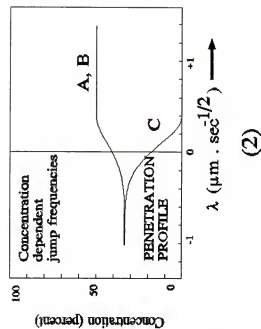


Figure 7.20: The concentration penetration profile and the Kirkendall shift pattern for couple # 02, Case (D), with $\Gamma_A : \Gamma_B : \Gamma_C$:: Fast : Medium : Slow.



Couple # 03
Case (B)

(1)

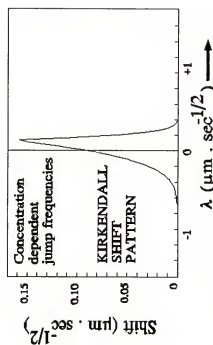
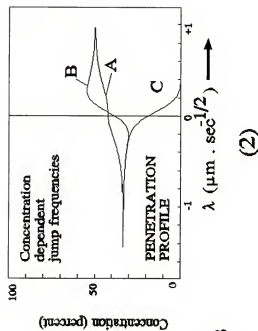


Figure 7.21: The concentration penetration profile and the Kirkendall shift pattern for couple # 03, Case (B), with $\Gamma_A : \Gamma_B : \Gamma_C$: Fast : Fast : Slow.



Couple # 03
Case (C)

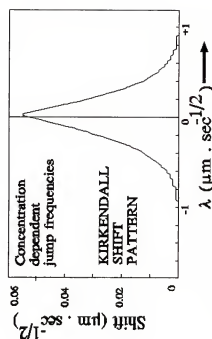


Figure 7.22: The concentration penetration profile and the Kirkendall shift pattern for couple # 03, Case (C), with Γ_A : Γ_B : Γ_C :: Fast : Slow : Slow.

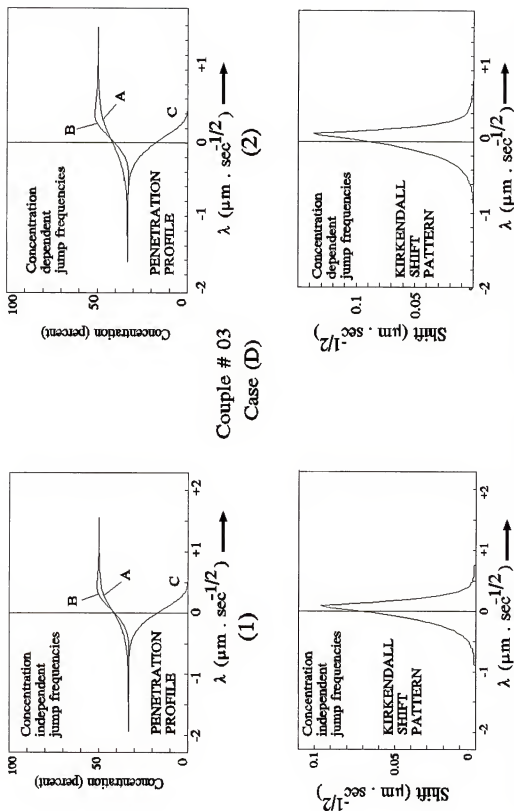


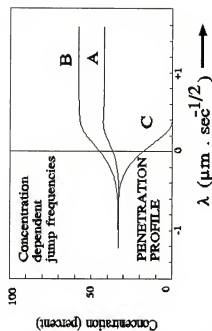
Figure 7.23: The concentration penetration profile and the Kirkendall shift pattern for couple # 03, Case (D), with Γ_A : Γ_B : Γ_C :: Fast : Medium : Slow.

components. In case (C) and to a lesser extent in case (D), there is a region where the outflow of A, the fast mover, increases the percentage of B, the slow-mover, causing a "hump" in the profile of the latter near the Q-end of the couple.

Couple # 04 (figures 7.24 through 7.26). Again, as in couple #2 and #3, there is an undulation in the profile of A (fast-mover) accompanied by a hump in the profile of B (slow-mover) in case (C). So far, the maximum in the Kirkendall shift profile is changing as one goes from couple to couple for cases (C) and (D), but not for case (B). The reason for this behavior is discussed later in this chapter.

Couple # 05 (figures 7.27 through 7.29). As already pointed out, the ordinate in the graphs depicting the Kirkendall shift profile is changing from figure to figure. For instance, note that in case (C) [figure 7.28], the shift is zero for all practical purposes for both the concentration independent and dependent cases ($\Delta\lambda < 0.01 \mu\text{m}$), although there is considerable structure to the profile as drawn for a highly refined ordinate scale.

Couple # 06 (figures 7.30 through 7.32). As can be seen from the Kirkendall shift profiles for case (D) [figure 7.32], the lattice velocities are *not always in the one direction in a given couple*. {Note: In all of these simulations, a shift to the right is considered positive}. As one traverses from the left hand side end-point composition to the right hand side,



Couple # 04
Case (B)

(1)

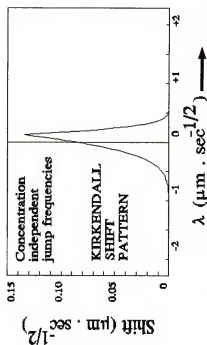


Figure 7.24: The concentration penetration profile and the Kirkendall shift pattern for couple # 04, Case (B), with $\Gamma_A : \Gamma_B : \Gamma_C :: \text{Fast} : \text{Fast} : \text{Slow}$.

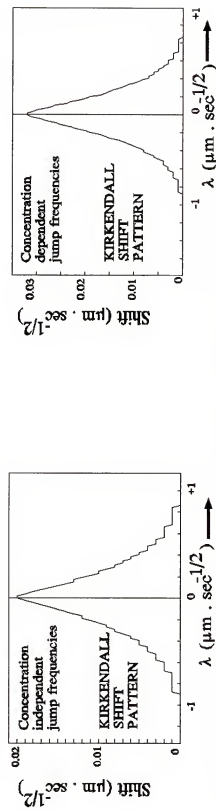
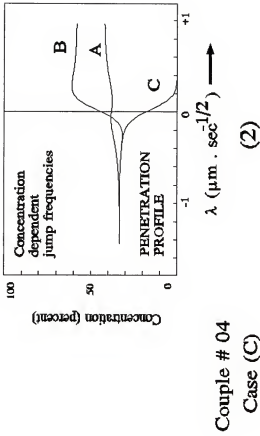


Figure 7.25: The concentration penetration profile and the Kirkendall shift pattern for couple # 04, Case (C), with Γ_A : Γ_B : Γ_C :: Fast : Slow : Slow.

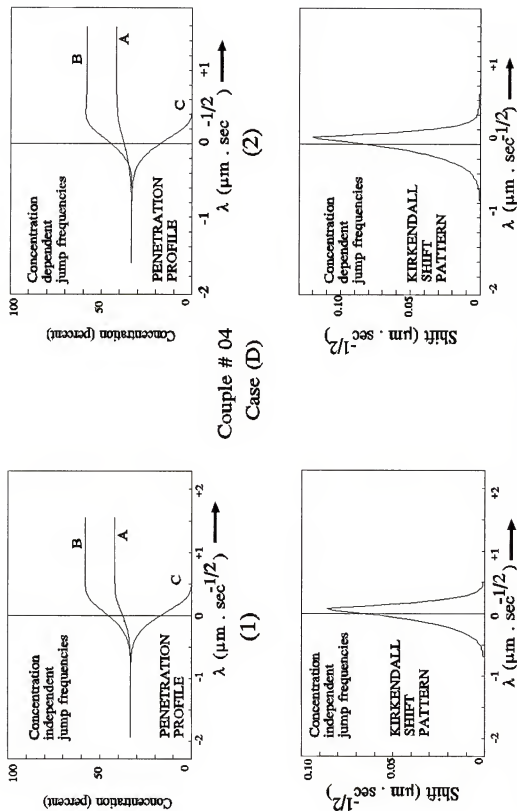


Figure 7.26: The concentration penetration profile and the Kirkendall shift pattern for couple # 04, Case (D), with Γ_A : Γ_B : Γ_C :: Fast : Medium : Slow.

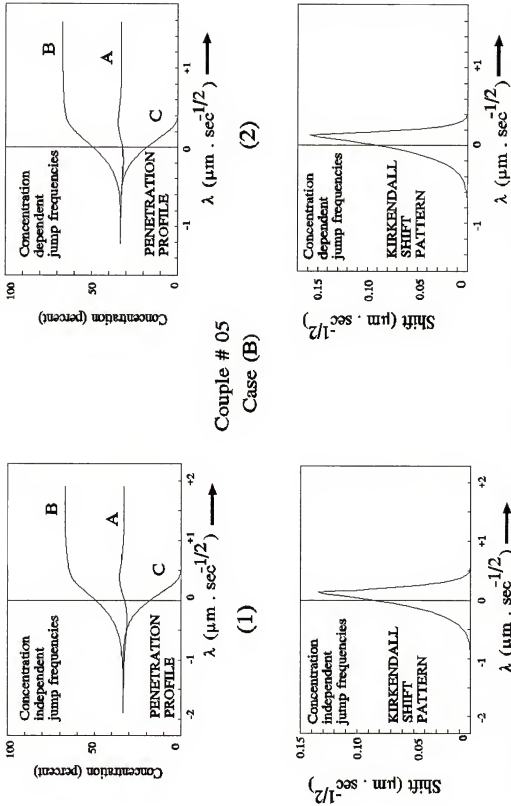


Figure 7.27: The concentration penetration profile and the Kirkendall shift pattern for couple # 05, Case (B), with Γ_A : Γ_B : Γ_C :: Fast : Fast : Slow.

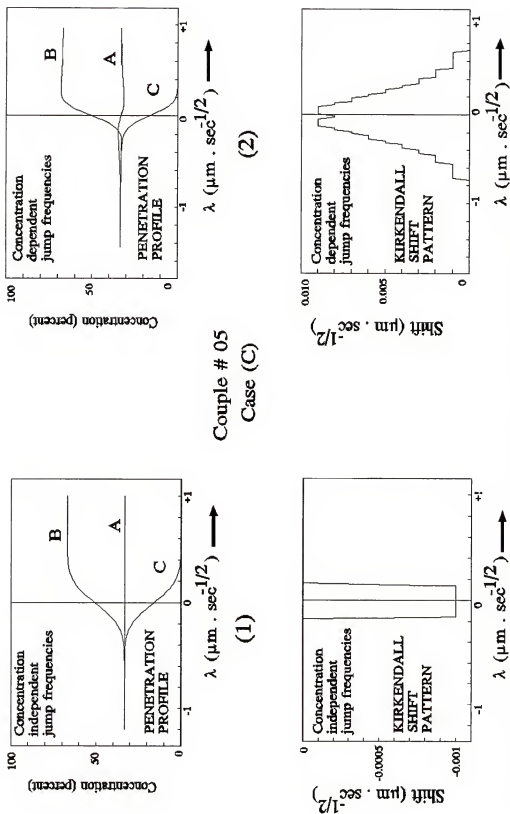


Figure 7.28: The concentration penetration profile and the Kirkendall shift pattern for couple # 05, Case (C), with $\Gamma_A : \Gamma_B : \Gamma_C :: \text{Fast} : \text{Slow} : \text{Slow}$.

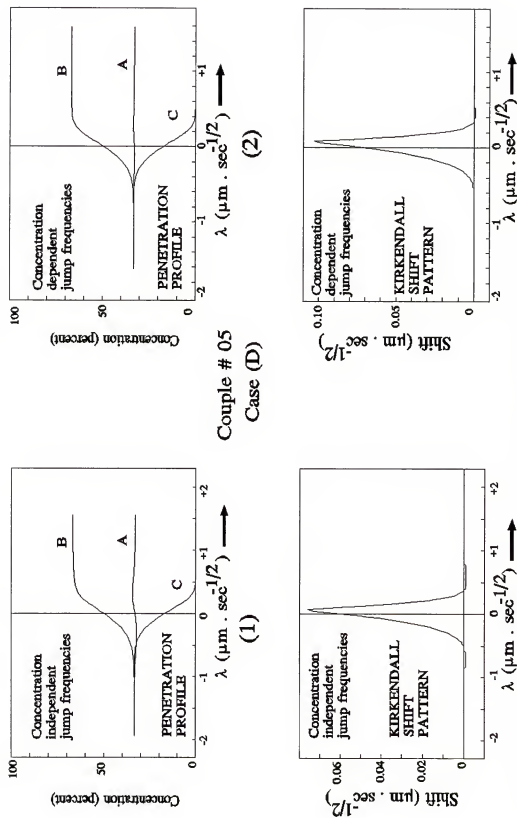


Figure 7.29: The concentration penetration profile and the Kirkendall shift pattern for couple # 05, Case (D), with $\Gamma_A : \Gamma_B : \Gamma_C$:: Fast : Medium : Slow.

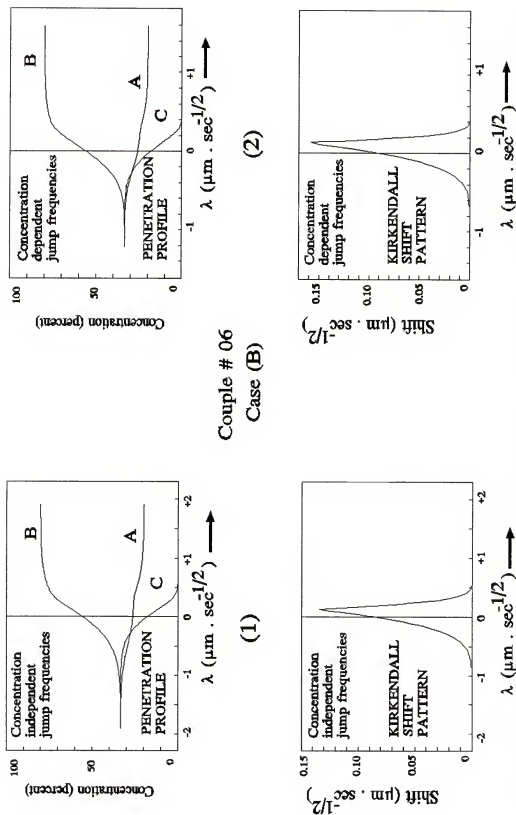


Figure 7.30: The concentration penetration profile and the Kirkendall shift pattern for couple # 06, Case (B), with $\Gamma_A : \Gamma_B : \Gamma_C :: \text{Fast} : \text{Fast} : \text{Slow}$.

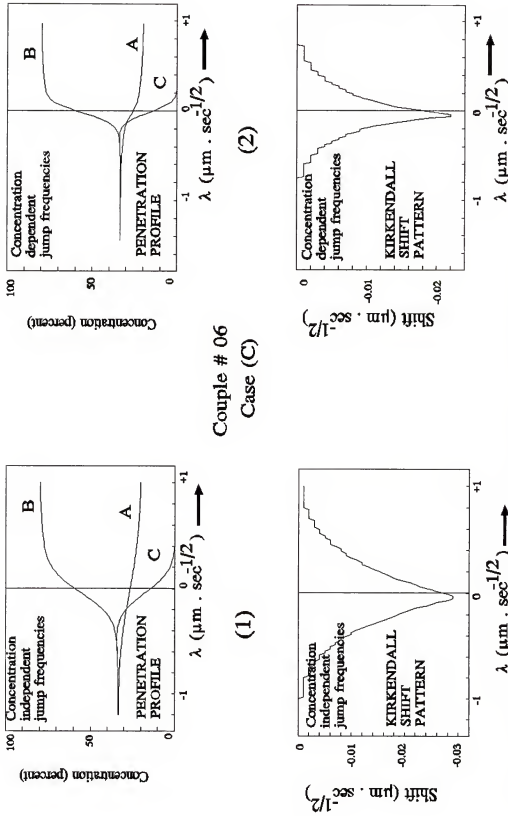


Figure 7.31: The concentration penetration profile and the Kirkendall shift pattern for couple # 06, Case (C), with Γ_A : Γ_B : Γ_C :: Fast : Slow : Slow.

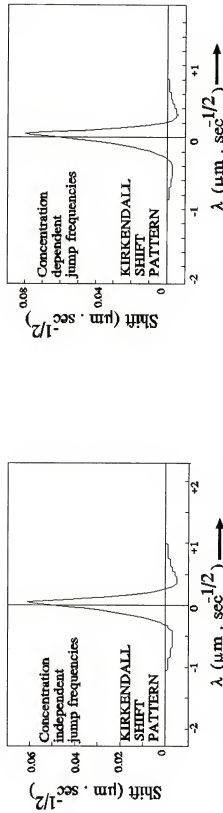
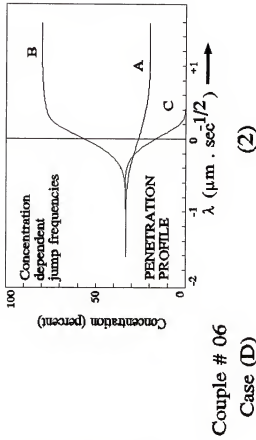


Figure 7.32: The concentration penetration profile and the Kirkendall shift pattern for couple # 06, Case (D), with $\Gamma_A : \Gamma_B : \Gamma_C :: \text{Fast} : \text{Medium} : \text{Slow}$.

in the direction of diffusion, this shift starts out at zero, becomes increasingly negative (meaning the shift is to the left), reaches a maximum negative value, decreases (in magnitude) to zero, becomes positive (meaning the shift is to the right), reaches a maximum positive value, decreases to zero, once again becomes negative, reaches a maximum negative value and decreases (in magnitude) back down to zero at the right hand side of the couple. This profile makes it evident that the measurement of the shift of the inert markers, placed at the original weld interface, at the end of the diffusion anneal does not tell the whole story about the lattice velocities. One must, in fact, put this "Kirkendall shift" measurement to good use with a careful examination of the "humps", "hollows" and "undulations" in the concentration profile in order to be able to make an educated guess regarding the behavior of the Γ 's in the couple.

Couple # 08 (figures 7.36 through 7.38). The Kirkendall shift profile for case (D) [figure 7.38] shows a peculiar shape. While this may be significant, it probably is once again an artifact of the highly refined ordinate scale.

Couples # 7, 9-13 and 16. These couples exhibit various phenomena already discussed for the other cases. For example, in couple #13, case (B) [figure 7.51], the profiles of A and B coincide, because both of these components move equally fast and have the same end-point composition.

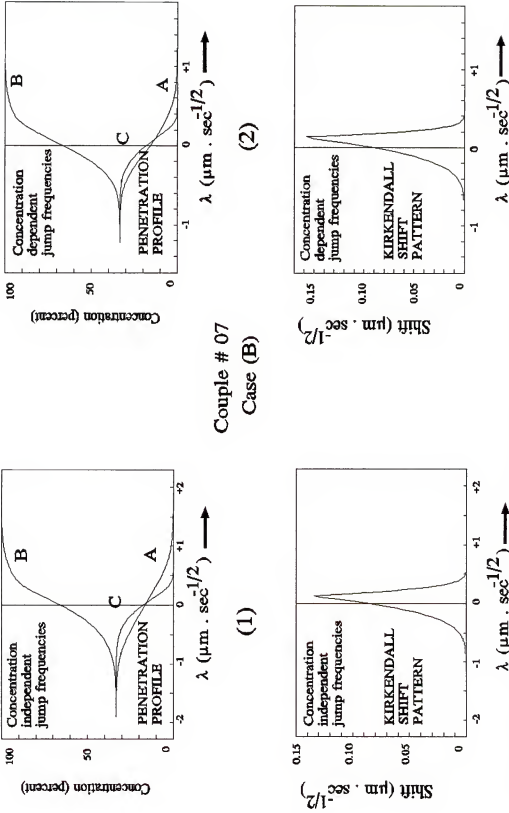


Figure 7.33: The concentration penetration profile and the Kirkendall shift pattern for couple # 07, Case (B), with Γ_A : Γ_B : Γ_C :: Fast : Fast : Slow.

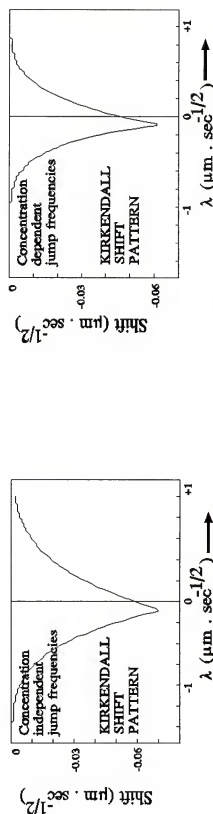
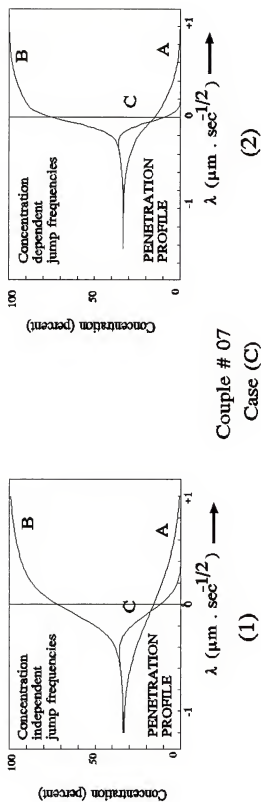


Figure 7.34: The concentration penetration profile and the Kirkendall shift pattern for couple # 07, Case (C), with $\Gamma_A : \Gamma_B : \Gamma_C :: \text{Fast} : \text{Slow} : \text{Slow}$.

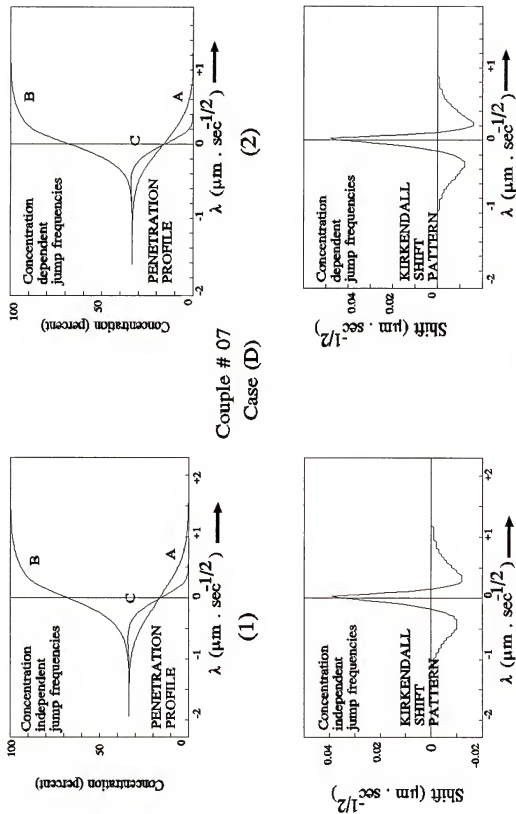
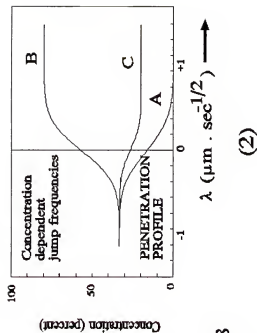


Figure 7.35: The concentration penetration profile and the Kirkendall shift pattern for couple # 07, Case (D), with Γ_A : Γ_B : Γ_C :: Fast : Medium : Slow.



Couple # 08
Case (B)

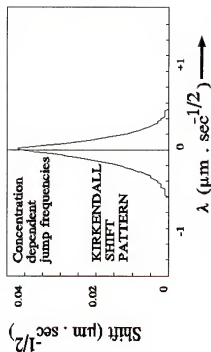
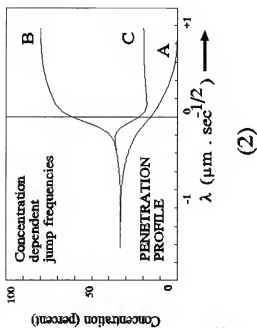


Figure 7.36: The concentration penetration profile and the Kirkendall shift pattern for couple # 08, Case (B), with $\Gamma_A : \Gamma_B : \Gamma_C :: \text{Fast} : \text{Fast} : \text{Slow}$.



Couple # 08
Case (C)

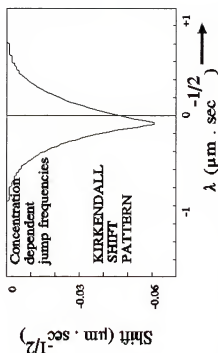
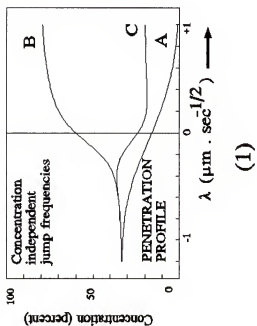


Figure 7.37: The concentration penetration profile and the Kirkendall shift pattern for couple # 08, Case (C), with Γ_A : Γ_B : Γ_C :: Fast : Slow : Slow.

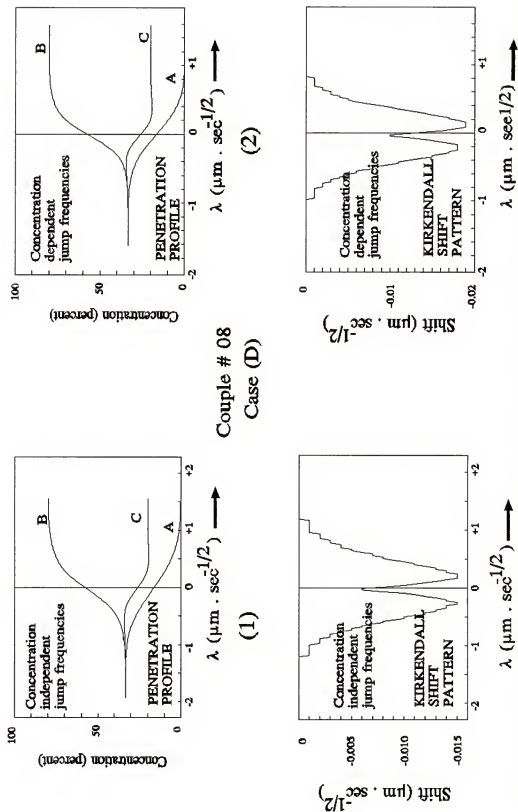
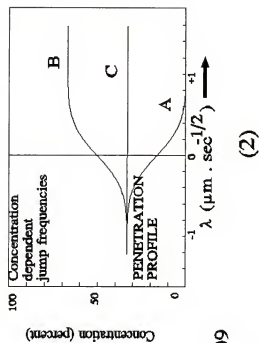


Figure 7.38: The concentration penetration profile and the Kirkendall shift pattern for couple # 08, Case (D), with Γ_A : Γ_B : Γ_C :: Fast : Medium : Slow.



Couple # 09
Case (B)

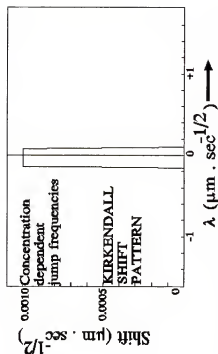


Figure 7.39: The concentration penetration profile and the Kirkendall shift pattern for couple # 09, Case (B), with Γ_A : Γ_B : Γ_C :: Fast : Fast : Slow.

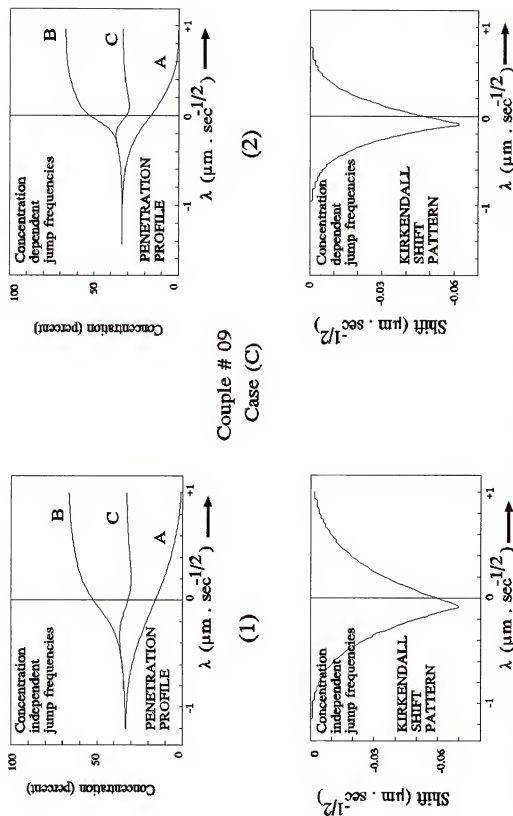


Figure 7.40: The concentration penetration profile and the Kirkendall shift pattern for couple # 09, Case (C), with Γ_A : Γ_B : Γ_C :: Fast : Slow : Slow.

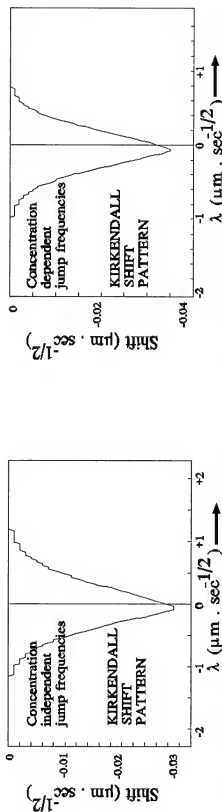
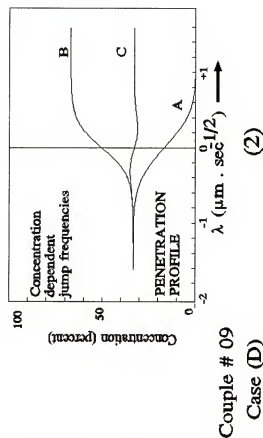


Figure 7.41: The concentration penetration profile and the Kirkendall shift pattern for couple # 09, Case (D), with Γ_A : Γ_B : Γ_C :: Fast : Medium : Slow.

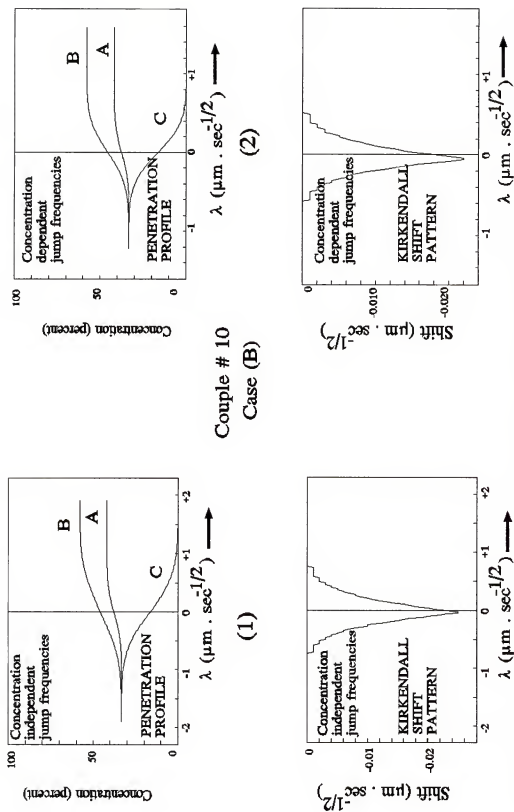


Figure 7.42: The concentration penetration profile and the Kirkendall shift pattern for couple # 10, Case (B), with Γ_A : Γ_B : Γ_C :: Fast : Fast : Slow.

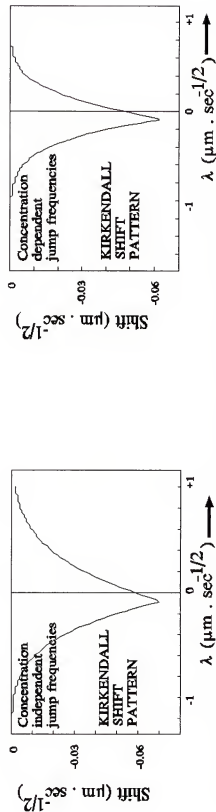
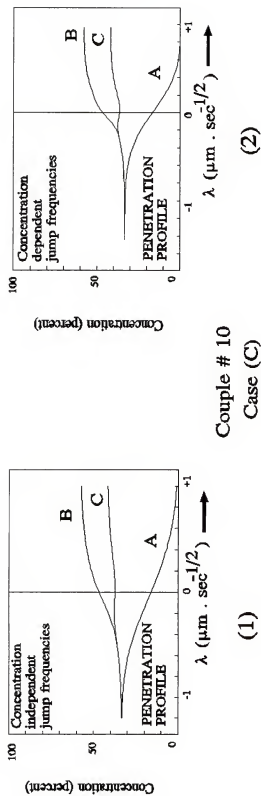
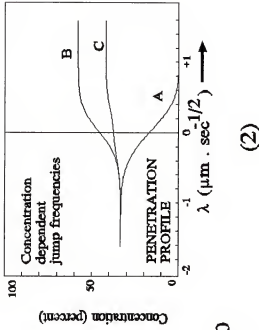


Figure 7.43: The concentration penetration profile and the Kirkendall shift pattern for couple # 10, Case (C), with $\Gamma_A : \Gamma_B : \Gamma_C$:: Fast : Slow : Slow.



Couple # 10
Case (D)

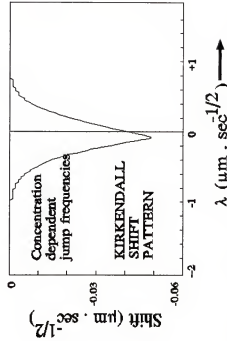
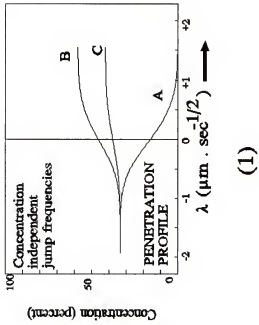


Figure 7.44: The concentration penetration profile and the Kirkendall shift pattern for couple # 10, Case (D), with $\Gamma_A : \Gamma_B : \Gamma_C$:: Fast : Medium : Slow.

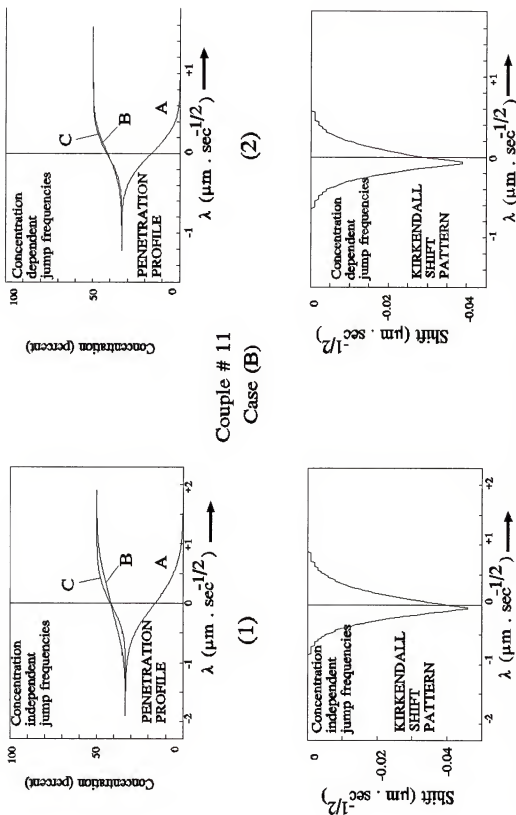
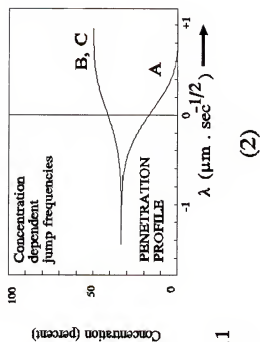


Figure 7.45: The concentration penetration profile and the Kirkendall shift pattern for couple # 11, Case (B), with Γ_A : Γ_B : Γ_C :: Fast : Fast : Slow.



Couple # 11
Case (C)

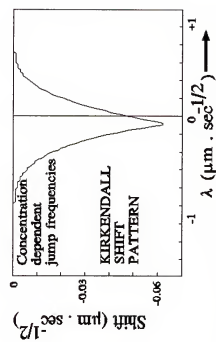


Figure 7.46: The concentration penetration profile and the Kirkendall shift pattern for couple # 11, Case (C), with $\Gamma_A : \Gamma_B : \Gamma_C :: \text{Fast} : \text{Slow} : \text{Slow}$.

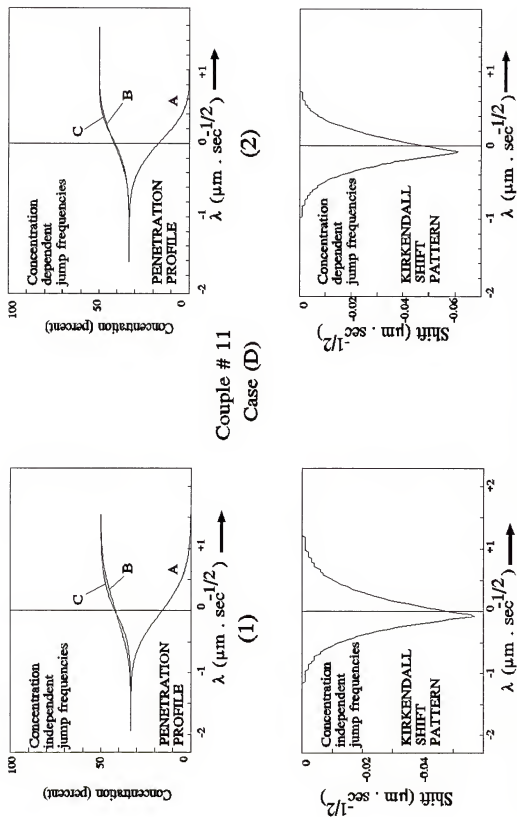


Figure 7.47: The concentration penetration profile and the Kirkendall shift pattern for couple # 11, Case (D), with Γ_A : Γ_B : Γ_C :: Fast : Medium : Slow.

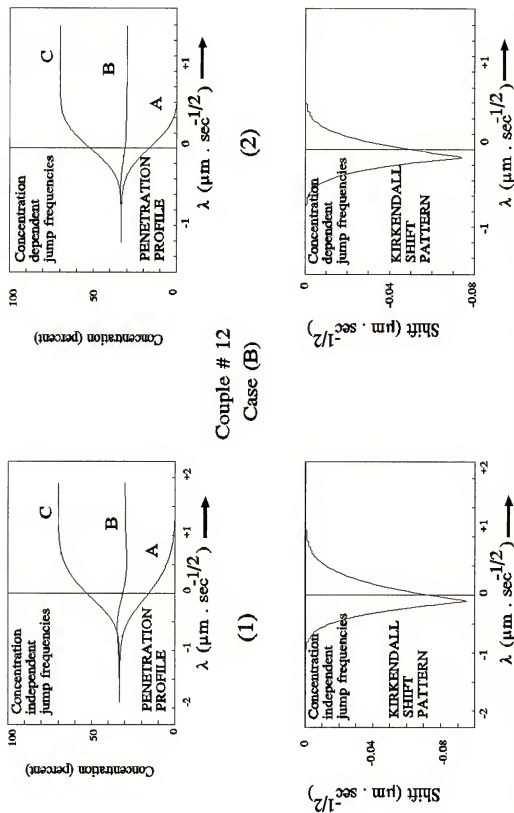


Figure 7.48: The concentration penetration profile and the Kirkendall shift pattern for couple # 12, Case (B), with Γ_A : Γ_B : Γ_C :: Fast : Fast : Slow.

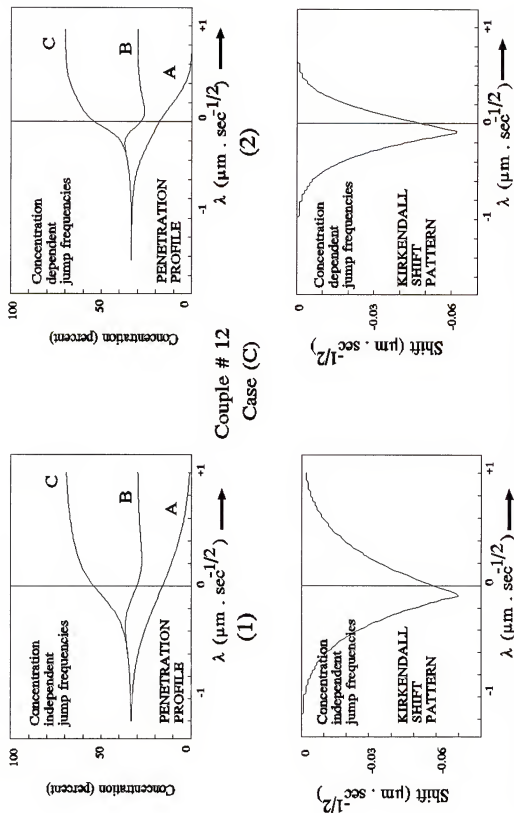


Figure 7.49: The concentration penetration profile and the Kirkendall shift pattern for couple # 12, Case (C), with Γ_A : Γ_B : Γ_C :: Fast : Slow : Slow.

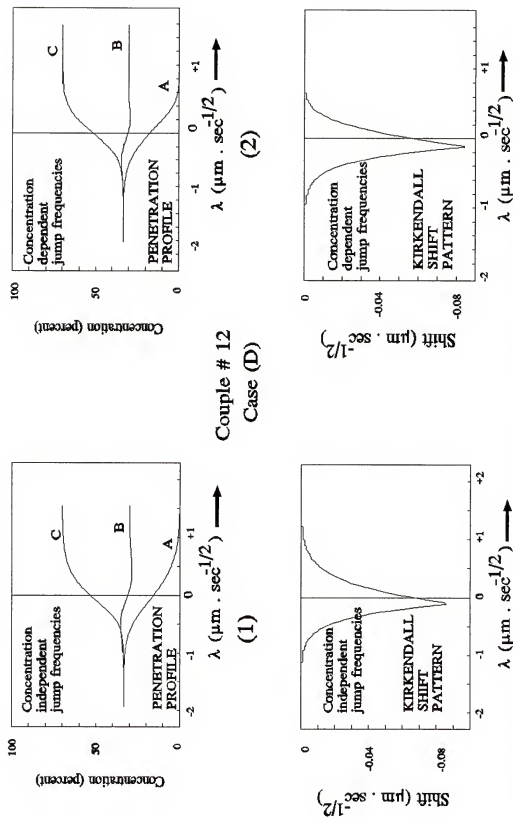


Figure 7.50: The concentration penetration profile and the Kirkendall shift pattern for couple # 12, Case (D), with Γ_A : Γ_B : Γ_C :: Fast : Medium : Slow.

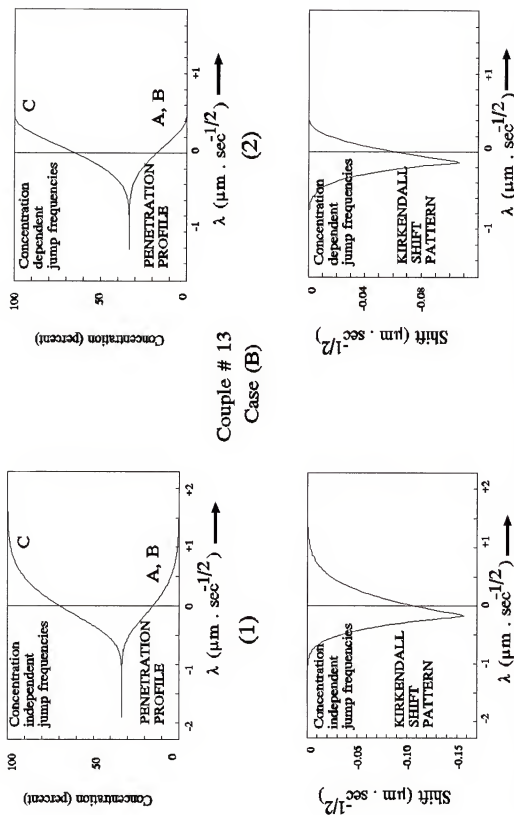


Figure 7.51: The concentration penetration profile and the Kirkendall shift pattern for couple # 13, Case (B), with $\Gamma_A : \Gamma_B : \Gamma_C :: \text{Fast} : \text{Fast} : \text{Slow}$.

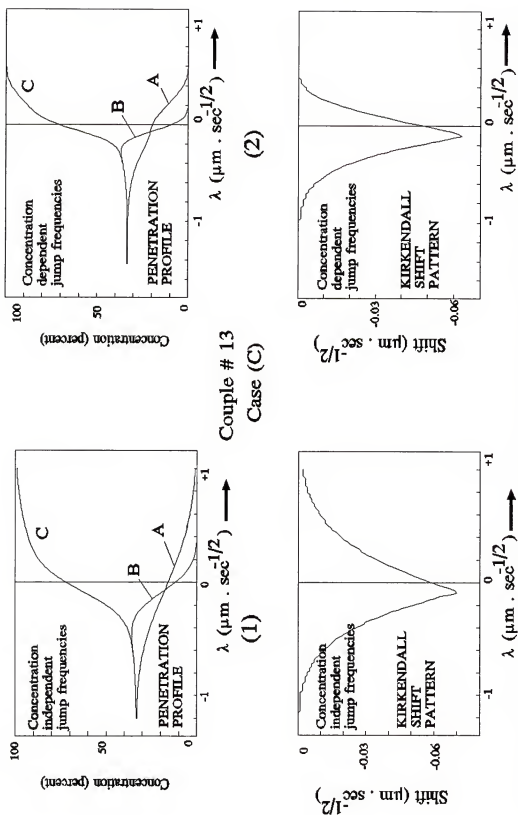
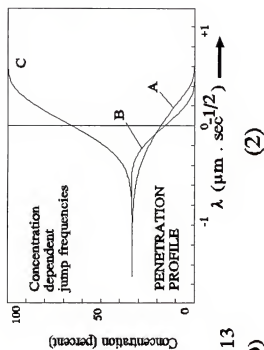


Figure 7.52: The concentration penetration profile and the Kirkendall shift pattern for couple # 13, Case (C), with Γ_A : Γ_B : Γ_C :: Fast : Slow : Slow.



Couple # 13
Case (D)

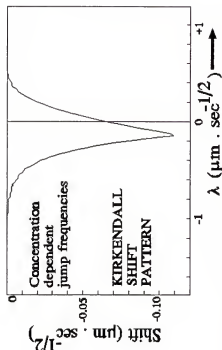


Figure 7.53: The concentration penetration profile and the Kirkendall shift pattern for couple # 13, Case (D), with $\Gamma_A : \Gamma_B : \Gamma_C$:: Fast : Medium : Slow.

Couples # 14 and 15 (figures 7.54 through 7.59). There is a very interesting feature for case (C_2) [figures 7.55 and 7.58] in these two couples. Whereas in the previously discussed cases the undulation in the fast-mover consisted of an accumulation toward the end rich in that component and a depletion toward the other end, in these two couples component A shows a *reverse undulation*. The reason for this is not immediately obvious and the phenomenon merits further scrutiny.

Couples # 17 and 18 (figures 7.63 through 7.68). In these couples, the *slow moving species*, C, shows the same kind of reverse undulations for case (C_2) [figures 7.64 and 7.67]. Once again, this phenomenon is due to the peculiarities involved in the lattice velocity profiles.

The Kirkendall Shift Patterns

Figures 7.69 through 7.74 represent the *pattern of Kirkendall shifts* for all eighteen couples for the cases (B_1) , (B_2) , (C_1) , (C_2) , (D_1) , and (D_2) respectively. In these figures, as opposed to figures 7.15 through 7.68, these shifts are plotted on the same scale in order to highlight any systematic variations in the pattern going around the Gibbs triangle from couple #1 to couple #18. These figures are discussed below.

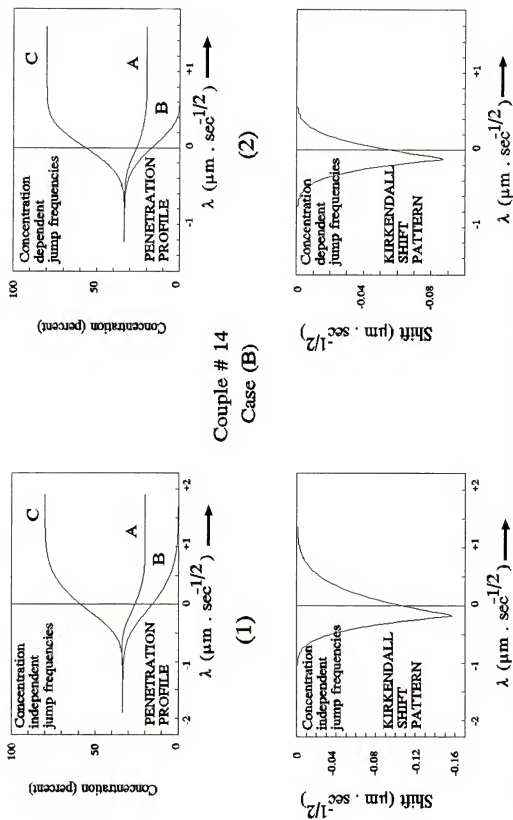


Figure 7.54: The concentration penetration profile and the Kirkendall shift pattern for couple # 14, Case (B), with $\Gamma_A : \Gamma_B : \Gamma_C :: \text{Fast} : \text{Fast} : \text{Slow}$.

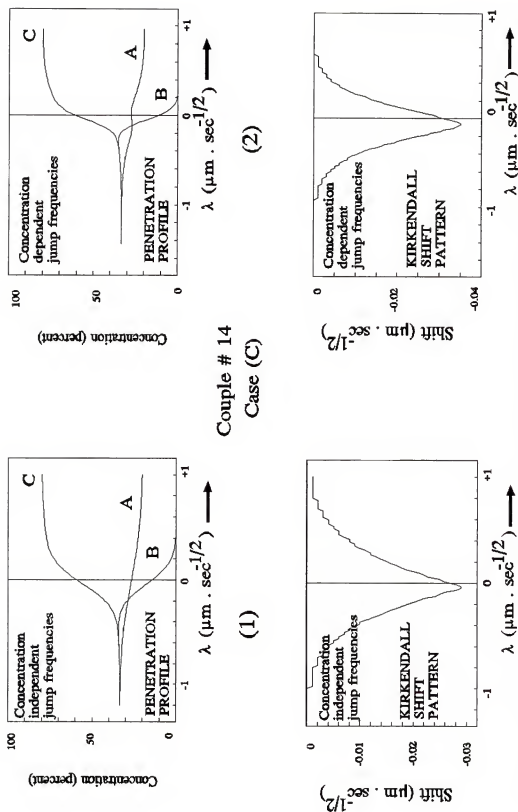


Figure 7.55: The concentration penetration profile and the Kirkendall shift pattern for couple # 14, Case (C), with Γ_A : Γ_B : Γ_C :: Fast : Slow : Slow.

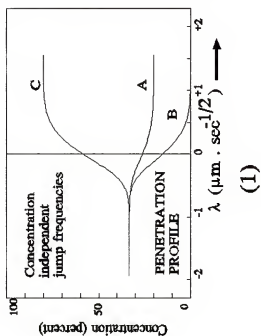
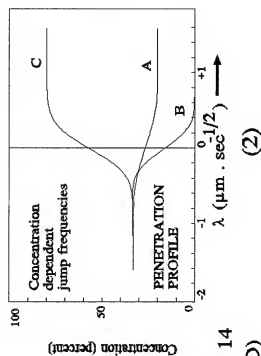
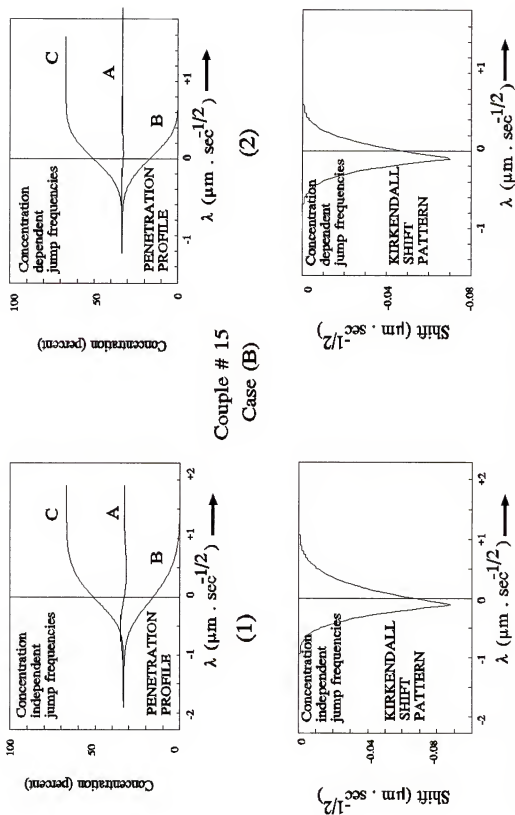


Figure 7.56: The concentration penetration profile and the Kirkendall shift pattern for couple # 14, Case (D), with $\Gamma_A : \Gamma_B : \Gamma_C :: \text{Fast} : \text{Medium} : \text{Slow}$.



Couple # 15
Case (B)

Figure 7.57: The concentration penetration profile and the Kirkendall shift pattern for couple # 15, Case (B), with $\Gamma_A : \Gamma_B : \Gamma_C :: \text{Fast} : \text{Fast} : \text{Slow}$.

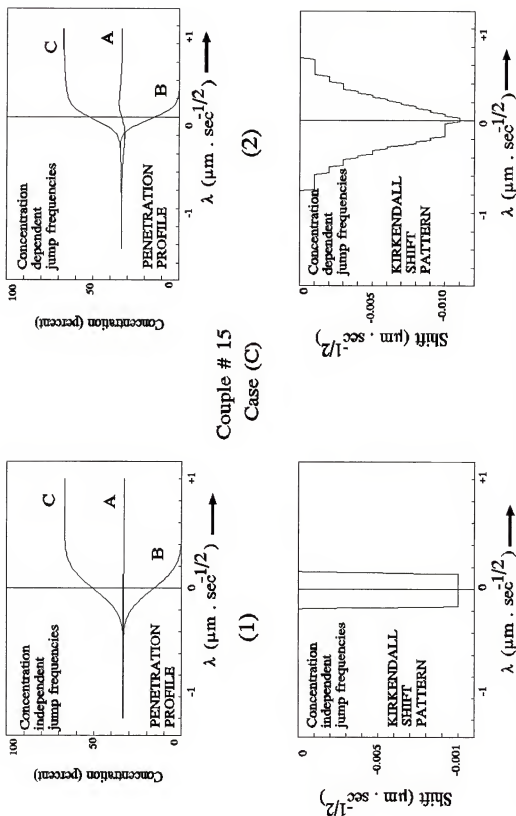


Figure 7.58: The concentration penetration profile and the Kirkendall shift pattern for couple # 15, Case (C), with Γ_A : Γ_B : Γ_C :: Fast : Slow : Slow.

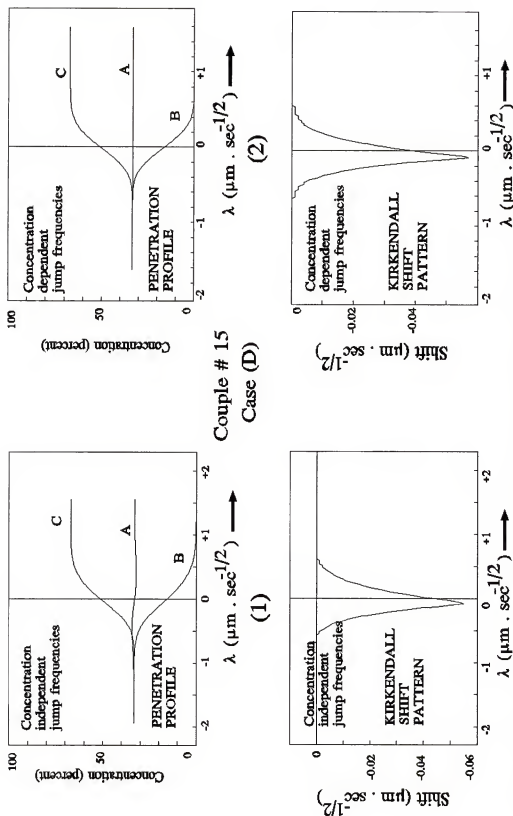
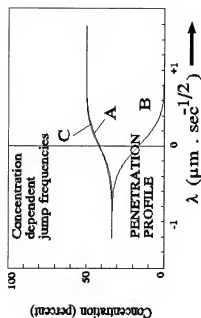
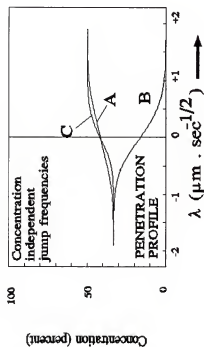


Figure 7.59: The concentration penetration profile and the Kirkendall shift pattern for couple # 15, Case (D), with $\Gamma_A : \Gamma_B : \Gamma_C :: \text{Fast} : \text{Medium} : \text{Slow}$.



Couple # 16
Case (B)

(1)



(2)

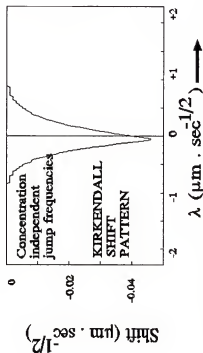
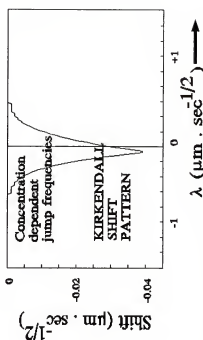


Figure 7.60: The concentration penetration profile and the Kirkendall shift pattern for couple # 16, Case (B), with Γ_A : Γ_B : Γ_C : Fast : Fast : Slow.

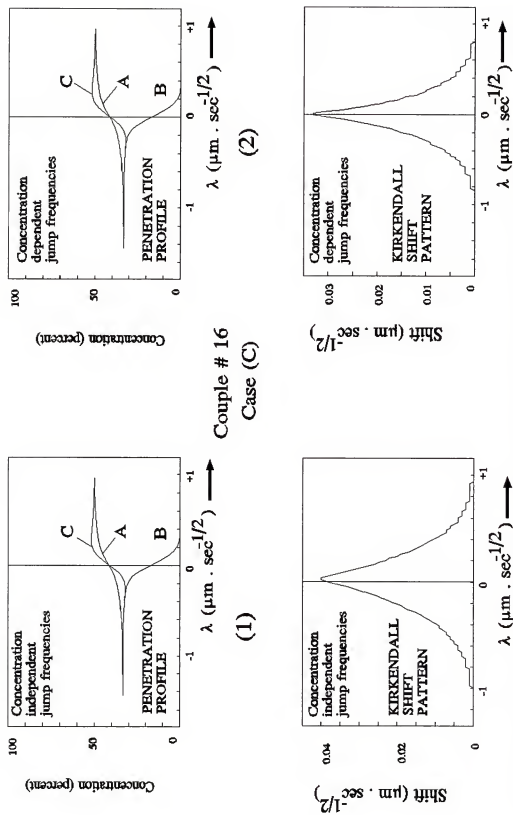


Figure 7.61: The concentration penetration profile and the Kirkendall shift pattern for couple # 16, Case (C), with Γ_A : Γ_B : Γ_C : Fast: Slow: Slow.

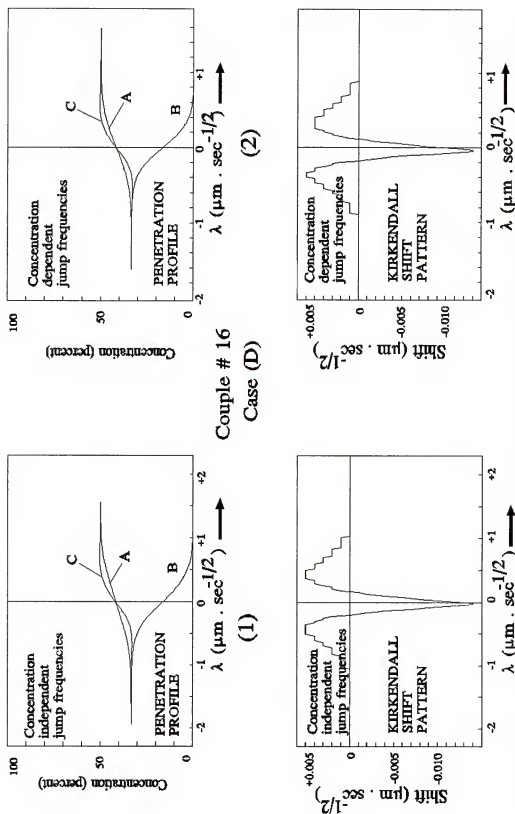


Figure 7.62: The concentration penetration profile and the Kirkendall shift pattern for couple # 16, Case (D), with $\Gamma_A : \Gamma_B : \Gamma_C$:: Fast : Medium : Slow.

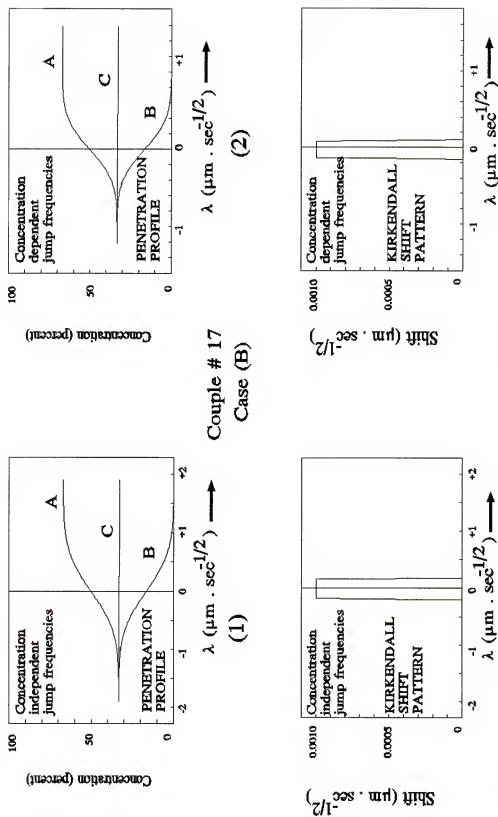


Figure 7.63: The concentration penetration profile and the Kirkendall shift pattern for couple # 17, Case (B), with $\Gamma_A : \Gamma_B : \Gamma_C :: \text{Fast} : \text{Fast} : \text{Slow}$.

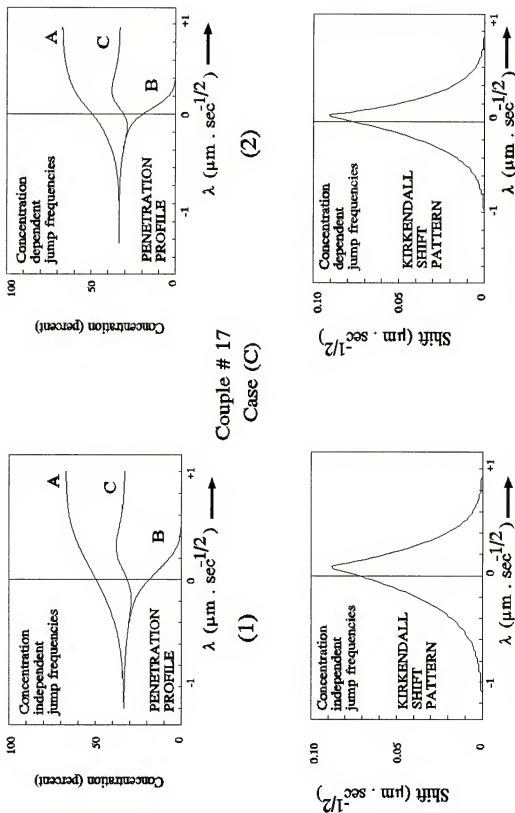


Figure 7.64: The concentration penetration profile and the Kirkendall shift pattern for couple # 17, Case (C), with $\Gamma_A : \Gamma_B : \Gamma_C :: \text{Fast} : \text{Slow} : \text{Slow}$.

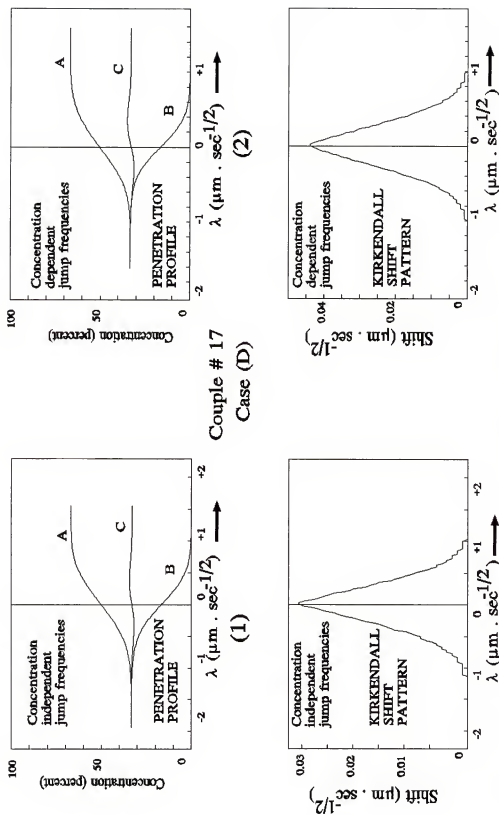


Figure 7.65: The concentration penetration profile and the Kirkendall shift pattern for couple # 17, Case (D), with $\Gamma_A : \Gamma_B : \Gamma_C ::$ Fast : Medium : Slow.

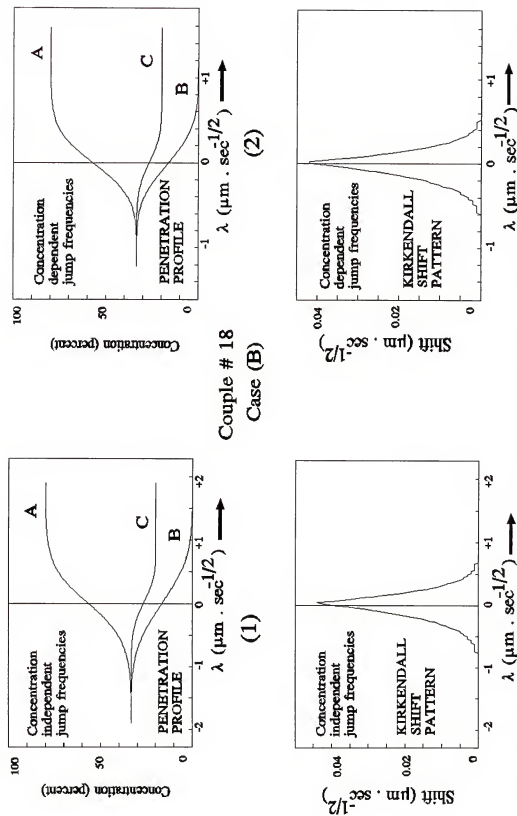
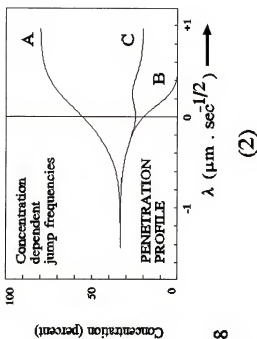


Figure 7.66: The concentration penetration profile and the Kirkendall shift pattern for couple # 18, Case (B), with $\Gamma_A : \Gamma_B : \Gamma_C :: \text{Fast} : \text{Fast} : \text{Slow}$.



Couple # 18
Case (C)

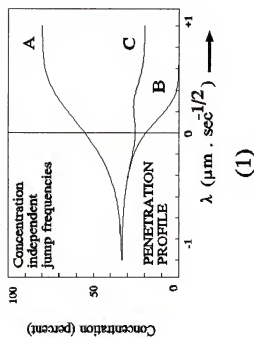


Figure 7.67: The concentration penetration profile and the Kirkendall shift pattern for couple # 18, Case (C), with $\Gamma_A : \Gamma_B : \Gamma_C :: \text{Fast} : \text{Slow} : \text{Slow}$.

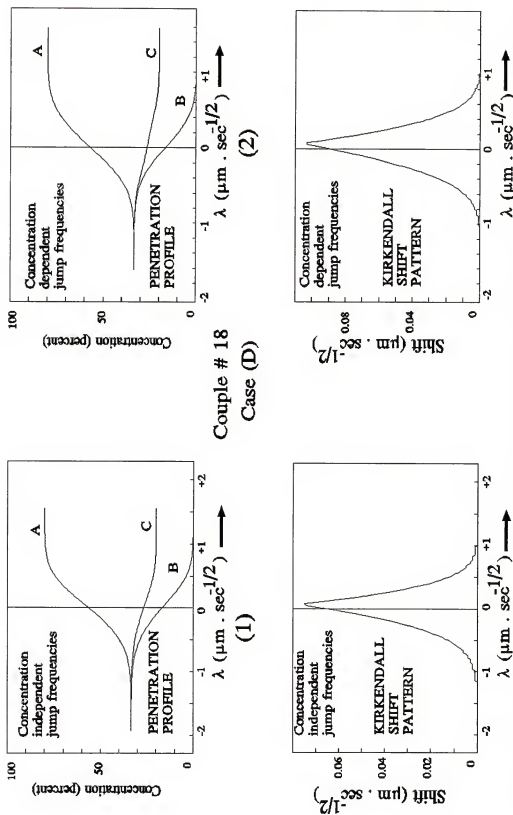


Figure 7.68: The concentration penetration profile and the Kirkendall shift pattern for couple # 18, Case (D), with $\Gamma_A : \Gamma_B : \Gamma_C ::$ Fast : Medium : Slow.

Case (B) - (figures 7.69 and 7.70). From these figures it can be seen that the couples along the A-B binary, including the pure A and pure B couples (couple # 1 through 7), have identical Kirkendall shift patterns. This observation is due to the fact that A and B are equally fast movers in this case so that any composition on the A-B binary has the same effect on lattice motion. In this respect, the ternary couple acts as if it is a *pseudo-binary system (AB) versus C*.

Case (C) - (figures 7.71 and 7.72). In this case, A is the only fast mover and B and C are equally slow. As a consequence, the shift patterns on the B-C binary are now identical. Thus, for couples whose end-point composition on the Q-side is on the B-C binary, the system behaves as if it is a *pseud-binary of A versus (BC)*. Again, the magnitude of the shifts are higher for the concentration dependent case (C_2).

Case (D) - (figures 8.73 and 8.74). Since all three Γ 's are different in this case, there is no particularly startling pattern as observed in cases (B) and (C).

In all of the above cases, the Kirkendall shift profile goes through two *sign reversals* as one scans through couples 1 through 18. These sign reversals occur as the end-point composition on the Q-side goes from a high concentration of the fast moving species to a high concentration of the slow mover. In the RPT work discussed in chapter 5, this reversal

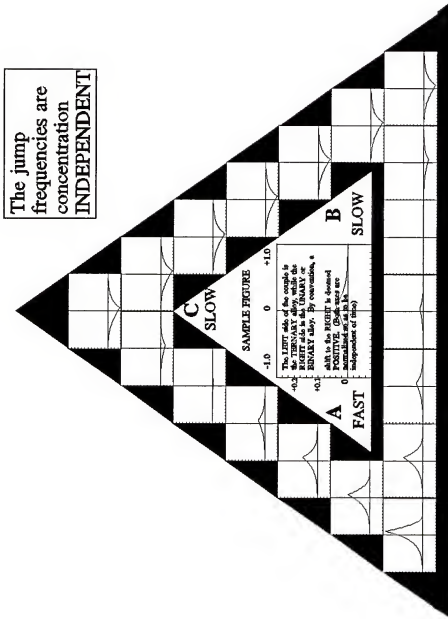


Figure 7.71: A survey of the change in Kirkendall shift patterns as a function of the end-point composition, for the 18 couples simulated. The left hand side of all the couples is the 1/3-1/3-1/3 alloy, and the right hand side compositions are varied along the sides of the Gibbs triangle. Case $C_1: \Gamma_A : \Gamma_B : \Gamma_C :: \text{Fast} : \text{Slow} : \text{Slow}$ (composition independent).

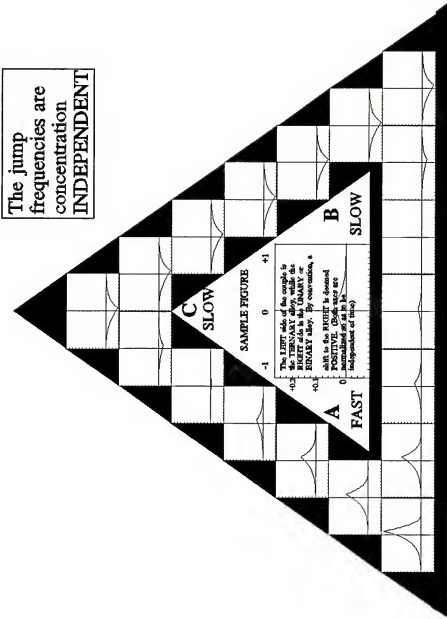


Figure 7.71: A survey of the change in Kirkendall shift patterns as a function of the end-point composition, for the 18 couples simulated. The left hand side of all the couples is the 1/3-1/3-1/3 alloy, and the right hand side compositions are varied along the sides of the Gibbs triangle. Case C₁: $\Gamma_A : \Gamma_B : \Gamma_C :: \text{Fast} : \text{Slow} : \text{Slow (composition independent)}$.

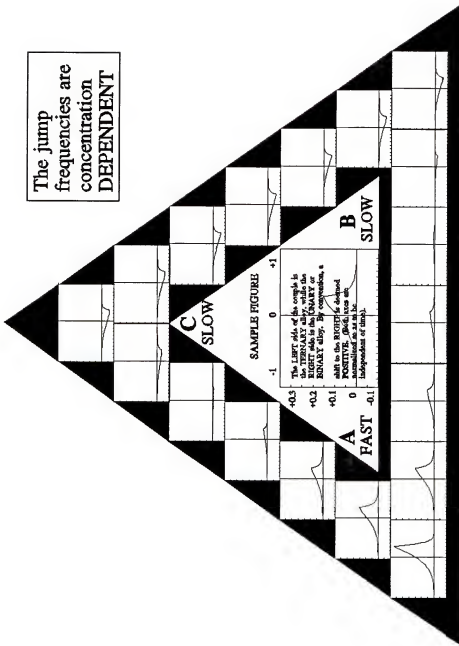


Figure 7.72: A survey of the change in Kirkendall shift patterns as a function of the end-point composition, for the 18 couples simulated. The left hand side of all the couples is the 1/3-1/3-1/3 alloy, and the right hand side compositions are varied along the sides of the Gibbs triangle. Case C₂: $\Gamma_A : \Gamma_B : \Gamma_C :: \text{Fast} : \text{Slow} : \text{Slow}$ (composition dependent).

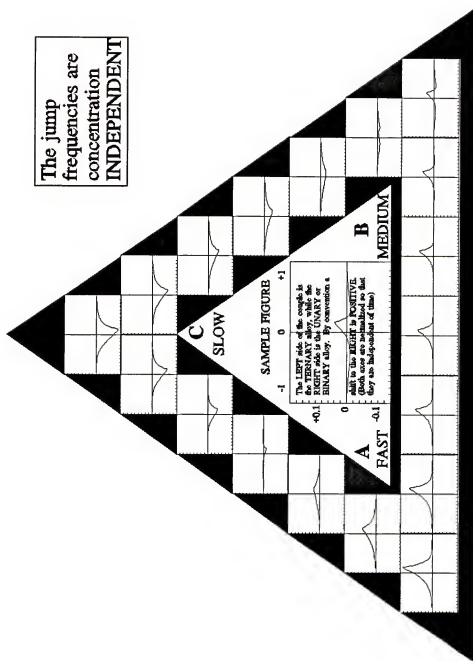


Figure 7.73: A survey of the change in Kirkendall shift patterns as a function of the end-point composition, for the 18 couples simulated. The left hand side of all the couples is the 1/3-1/3-1/3 alloy, and the right hand side compositions are varied along the sides of the Gibbs triangle. Case D_1 : $\Gamma_A : \Gamma_B : \Gamma_C ::$ Fast : Medium : Slow (composition independent).

was attributed to the place where the line joining the end-point compositions crosses an *isotendency* line. In the case of JFA, such a distinction is not so obvious, although the same observation still holds in a qualitative sense.

Concluding Comments

It must be emphasized that the survey of ternary isomorphous diffusion presented above is only one of many ways of tackling this task. Depending on the specifics of the diffusion problem confronted by the researcher, one can custom design such surveys so that they are pertinent to the conditions that obtain. In the next chapter, experimental diffusion data in three different isomorphous systems are analyzed in just such a fashion.

CHAPTER 8
JFA MODELS FOR EXPERIMENTAL DATA IN ISOMORPHOUS SYSTEMS

Introduction

An exploratory survey of the concentration-penetration profiles, composition paths and Kirkendall shift patterns in ternary isomorphous systems with concentration independent as well as concentration dependent jump frequencies as input was presented in the previous chapter. However, the usefulness of a computational construct such as the jump frequency approach is best measured by its ability to predict experimentally measured paths and profiles in diffusion studies. In this chapter, an attempt is made to model the jump frequency as a function of composition in three different ternary isomorphous systems, with a view to obtaining a match with published experimental results.

Experimental results on a number of diffusion couples spanning a range of compositions along the ternary isotherm were obtained by Vignes and Sabatier⁶ for the Fe-Co-Ni system, by Ziebold and Ogilvie⁷ for the Cu-Ag-Au system, and by Wan⁸ for the Cu-Ni-Zn system. These results consist of the composition paths in the diffusion zone and, in the case of Wan's work, the shift of the Kirkendall markers placed at the

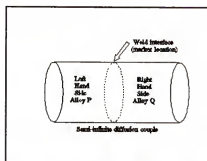
original weld interface. These diffusion studies were simulated with the jump frequency approach. The computer models use the same end-point compositions as those in the experiments and invoke a set of jump frequencies, together with their compositional dependence. The computer runs yield not only the composition paths but also the concentration-penetration profiles and the lattice velocity patterns. The results of these simulations are described below and compared with the experiments.

The Iron-Cobalt-Nickel System

Vignes and Sabatier surveyed the diffusion paths spanning the entire Gibbs triangle in the Fe-Co-Ni system at 1315°C. They diffusion annealed sandwiches made of two different alloys at this temperature for periods ranging from 16 to 24 hours. They then generated concentration-penetration profiles using the microprobe and , from this information, produced composition paths. The compositions of the fourteen couples studied by them are listed in Table 8.01.

The composition paths generated by the above authors can be seen in figure 8.02. Following the conclusion of the authors themselves, who state that their findings are compatible with the assumption that the mobilities of the three species are such that Fe is the fast mover, with Co and

Table 8.01: The end-point compositions of the alloys studied by Vignes and Sabatier⁶ in their work on diffusion in the Fe-Co-Ni ternary system. These same compositions were used for the computer simulations for comparison with experiment.



Couple #	Composition of alloy P (LHS) in atom percent			Composition of alloy Q (RHS) in atom percent		
	Fe	Co	Ni	Fe	Co	Ni
1	89.0	11.0	0	0	0	100.0
2	68.4	0	31.6	0	70.0	30.0
3	64.0	36.0	0	0	31.0	69.0
4	28.6	71.4	0	30.0	0	70.0
5	60.4	50.0	0	0	50.0	50.0
6	28.6	71.4	0	0	70.0	30.0
7	9.5	90.5	0	0	0	100.0
8	50.0	0	50.0	0	50.0	50.0
9	30.0	0	70.0	0	31.0	69.0
10	68.4	0	31.6	9.5	90.5	0
11	68.4	0	31.6	69.5	30.5	0
12	0	0	100.0	50.0	50.0	0
13	0	0	100.0	17.5	67.8	14.7
14	100.0	0	0	0	50.0	50.0

Ni nearly equally slow by comparison, as well as Wan's RPT model for these results, a model for the composition dependence of the jump frequencies was chosen as depicted in figure 8.01. In this model the jump frequencies are in the same ratio as their composition dependence so that all species are fast movers at the Fe end of the Gibbs triangle, and slow at the Co and Ni ends. Applying this model to a computer simulation resulted in the computer generated paths shown in figure 8.02. The experimental and the simulated paths are nearly identical and the agreement is excellent.

In addition to the composition path, the JFA also produces concentration-penetration and Kirkendall shift profiles for each of the fourteen couples. In their paper, Vignes and Sabatier only produce some sample profiles obtained by microprobe. Figure 8.03 is a comparison of one of these samples with the profile generated by computer simulation. In this case, the computer-generated profile was 'corrected' to the appropriate annealing time (24 hours) used by the authors for this particular couple. This was achieved by the simple expedient of multiplying the normalized distance axis by the square root of the annealing time, expressed in seconds. Once again, there is satisfactory agreement between experiment and prediction.

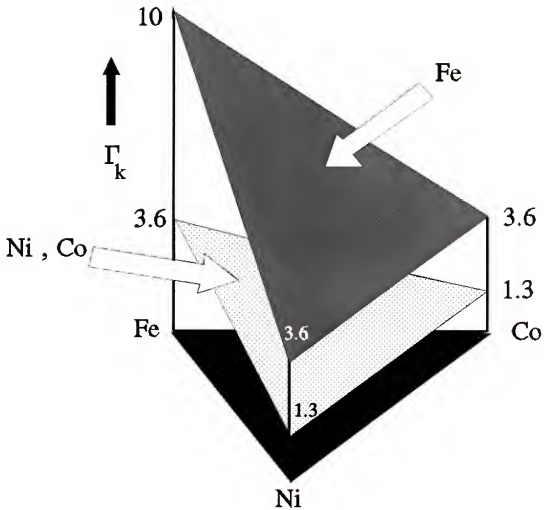


Figure 8.01: Composition dependence of the jump frequencies in the Fe-Co-Ni system according to the model used in the simulation. The top plane represents the variation of Γ_{Fe} across the phase diagram. The plane immediately below it is for Γ_{Co} and Γ_{Ni} , which have the same value at any given compositions. All jump frequencies are in millions of jumps per second.

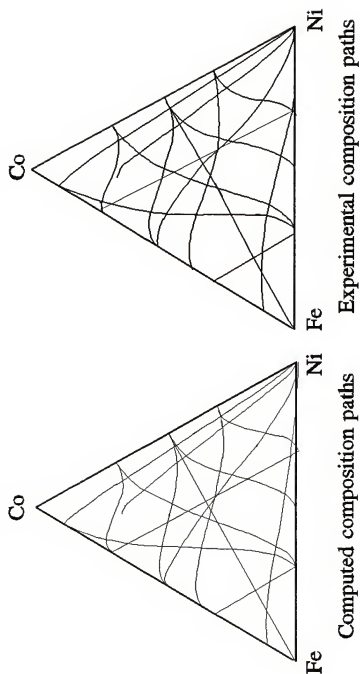


Figure 8.02: A comparison of the composition paths obtained experimentally by Vignes and Sabatier⁶ with the paths computed by simulation using the model in figure 8.01.

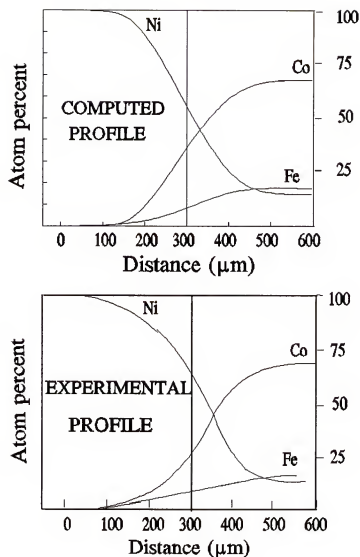


Figure 8.03: A comparison between the computed and experimentally measured concentration profiles for couple # 13 (see table 8.01) in the Fe-Co-Ni system. The computer generated graph has been adjusted for the experimental annealing time, which is 24 hours.

Another important feature of this particular series of simulations is the lattice velocity profile. Whereas with the models presented in Chapter 7, the Kirkendall shift profile was relatively simple in form, in this simulation we see that lattice velocity can indeed change signs in the middle of the diffusion zone and thus be considerably more complicated. Figure 8.04 illustrates this point. The marker plane, whose position corresponds to the origin of the x-axis in figure 8.04, has a shift very close to zero, despite the fact that significant lattice shifts in both directions occur elsewhere in the diffusion zone. Of course, this means that in order to conduct a thorough investigation of diffusion, one cannot be content with the movement of "inert markers" placed at the *original weld interface*. Instead, it would be preferable to have a series of markers, placed all along the diffusion direction so that the lattice velocity at each of these points can be monitored.

Vignes and Sabatier did not make any Kirkendall shift measurements, which is unfortunate as a comparison between the computer generated shift profile and the actual shifts would have been most instructive in this case, given the excellent quantitative agreement in the composition paths.

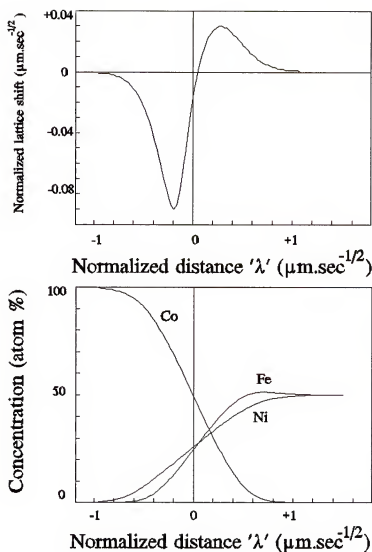


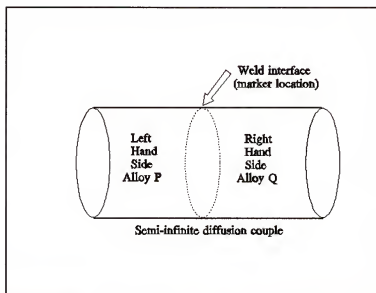
Figure 8.04: An example of the Kirkendall shift pattern and the concentration profiles in the Fe-Co-Ni system (couple # 12, see table 8.01), generated by computer simulation. Vignes and Sabatier did not present any Kirkendall shift data.

The Copper-Silver-Gold System

Ziebold and Ogilvie made an in depth investigation of the Cu-Ag-Au ternary isotherm at 725°C. At this temperature the system is isomorphous except for a miscibility gap on the Cu-Ag binary which extends into the ternary to about 30% Au. About half of the 17 couples studied by these authors have composition paths intersecting the two-phase field. At this writing, the JFA is not capable of handling this situation {see chapter 9}. Therefore, only eight of the couples were selected for the simulation studies. Table 8.02 lists the terminal composition of these couples.

The model chosen for the concentration dependence of jump frequencies is sketched in figure 8.05. This model is not as simple as the ones devised hitherto, in the sense that the concentration dependence of the jump frequencies does not follow the same quantitative pattern as the ratio of the jump frequencies themselves. These numbers were arrived at by Wan⁸ through trial and error {bracketing and laddering} so that the voluptuous curves that represent the composition paths in these couples can be best duplicated through simulation. The agreement between the model and the experiment that has been obtained in this case is not necessarily the best that could be achieved; in fact this particular model was chosen to provide a correspondence of the JFA model with the RPT model

Table 8.02: The end-point compositions of the alloys studied by Ziebold and Ogilvie in their work on diffusion in the Cu-Ag-Au ternary system⁷. These same compositions were used for the computer simulations for comparison with experiment.



Couple Number	Composition of alloy P (LHS) in atom %			Composition of alloy Q (RHS) in atom %		
	Cu	Ag	Au	Cu	Ag	Au
1	100.0	0	0	0	8.65	91.35
2	100.0	0	0	0	30.9	69.1
3	44.0	0	56.0	0	100.0	0
4	67.4	0	32.6	0	55.4	44.6
5	44.0	0	56.0	0	30.9	69.1
6	92.3	0	7.7	0	55.4	44.6
7	44.0	0	56.0	0	55.4	44.6
8	44.0	0	56.0	0	8.65	91.35

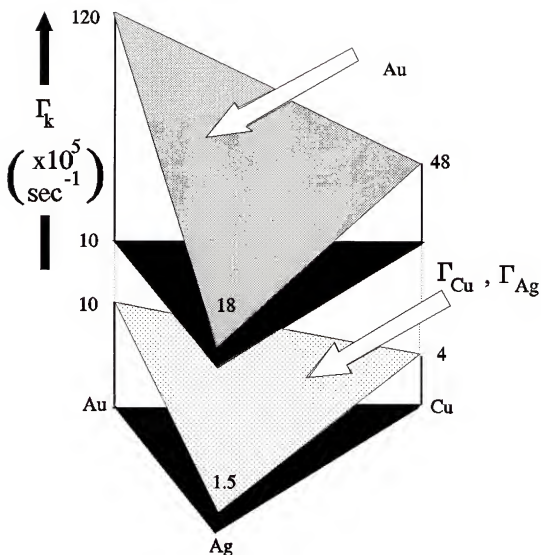


Figure 8.05: The model used for the composition dependence of the jump frequencies in the Cu-Ag-Au system studied by Ziebold and Ogilvie.⁷ Since gold diffuses much faster than silver and copper, the bottom portion of the figure has an expanded ordinate scale for the sake of clarity.

presented in chapter 5. The jump frequencies themselves are in the ratio $\Gamma_{Au}:\Gamma_{Ag}:\Gamma_{Cu} :: 12:1:1$, while their composition dependence at any point is given by the expression $[10X_{Au} + 4X_{Cu} + 1.5X_{Ag}]$, where the X_k 's are the mole fractions.

Figure 8.06 is a portrayal of the simulation results in comparison with the experimentally measured paths. The agreement is good, though not as satisfying as that in the Fe-Co-Ni system. Figure 8.07 shows the concentration-penetration and Kirkendall shift profiles for a typical couple. Once again, these authors did not do any measurements of marker movements so that this additional information obtained in the simulation run cannot be compared with any experiment.

An interesting feature of this system is the startling rapidity with which gold diffuses, in spite of its high melting point. In addition, the jump frequencies of all components are higher in gold-rich regions.

In both this system and the Fe-Co-Ni system discussed earlier, the researchers determined a matrix of chemical diffusion coefficients. They also presented the compositional dependence of the four diffusion coefficients involved. In principle, this result allows one to predict the composition of *any other arbitrary couple in the isotherm*. In practice, however, the procedure is tedious. On the other hand, armed with the composition dependence of the jump frequencies one can, with relative ease, run the simulation for any couple in the isotherm in a matter of seconds and predict the system's

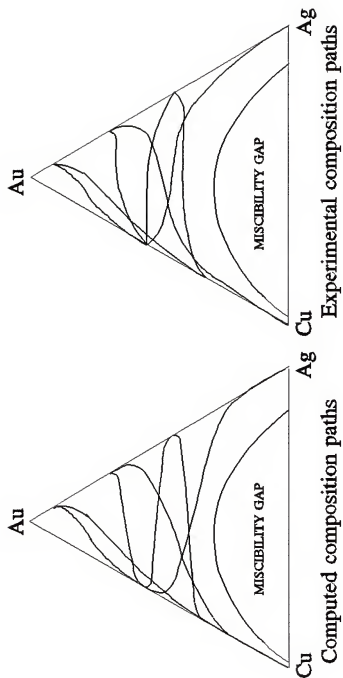


Figure 8.06: A comparison of the composition paths obtained experimentally by Ziebold and Ogilvie⁷ with the paths computed by simulation using the model in figure 8.05.

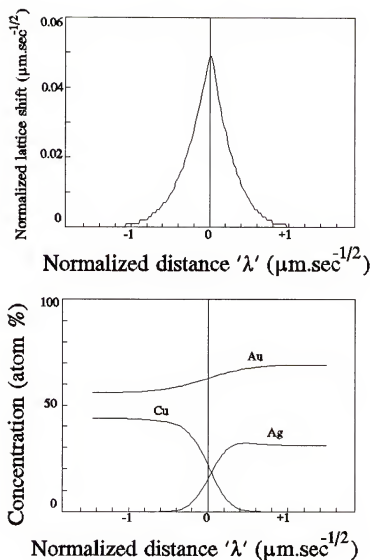


Figure 8.07: An example of the Kirkendall shift and concentration profiles in the Cu-Ag-Au system (couple # 5, see table 8.02), generated by computer simulation. Ziebold and Ogilvie⁷ did not present any Kirkendall shift information.

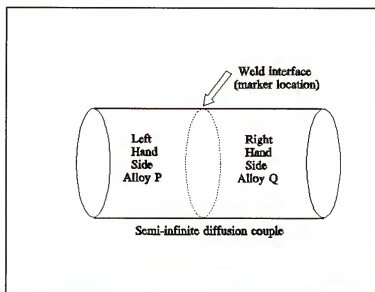
behavior. Furthermore, as already pointed out, the JFA can easily be extended to isomorphous systems of four or more components, a feat that is impossible to accomplish with the traditional Fickian analysis.

The Copper-Nickel-Zinc system

Wan conducted an extensive study on the copper corner of the Cu-Ni-Zn system, with semi-infinite diffusion couples that were annealed at 900°C for four days. In addition to the concentration-penetration profiles which he measured with the microprobe, Wan also reported the shift of the Kirkendall markers (5 μ m alumina powder) that were placed at the original weld interface. The end-point compositions of the alloys used in Wan's study are enumerated in Table 8.03.

Starting with a simple model, which assumed that the relative penetration depths and the tendencies (these are analogous to the jump frequencies and their compositional dependence) of the elements Cu, Ni and Zn are directly related to the tracer diffusivity data of (sic) the system, Wan came up with a relatively complicated 'helical' model for the penetration tendencies and their compositional dependence. The jump frequency 'analog' of this model is presented in figure 8.08. The key features of this model are that the concentration dependence of Γ_{Cu} and Γ_{Ni} have a higher ratio

Table 8.03: The end-point compositions of the alloys studied by Wan in his work on diffusion in the Cu-Ni-Zn ternary system. These same compositions were used for the computer simulations for comparison with experiment.



Couple Number	Composition of alloy P (LHS) in atom percent			Composition of alloy Q (RHS) in atom percent		
	Cu	Ni	Zn	Cu	Ni	Zn
1	76.7	0	23.3	78.7	21.3	0
2	54.2	22.6	23.2	90.1	10.9	0
3	91.5	0	8.5	45.3	36.8	17.9
4	82.0	0	18.0	90.1	19.9	0
5	41.1	30.6	28.3	90.1	9.9	0
6	100.0	0	0	63.7	21.5	14.8
7	65.4	11.6	23.2	100.0	0	0
8	54.5	24.0	21.5	100.0	0	0
9	100.0	0	0	47.0	34.5	18.5
10	82.0	0	17.6	69.3	30.7	0
11	89.6	0	10.4	78.5	21.5	0

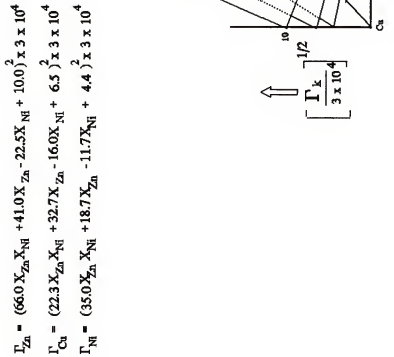


Figure 8.08: The model used for composition dependence of jump frequencies for simulating Wan's⁸ experiments in the Cu-Ni-Zn system. The surfaces representing the jump frequencies are helical and, as shown above, the composition dependence involves second order terms.

(relative to Γ_{Zn}) in the high-zinc, low-nickel area and a lower ratio (again relative to Γ_{Zn}) in the low-zinc, high-nickel area.

The computer simulations on eleven couples studied by Wan were run, based on the above model for the Γ 's. The results are presented in figures 8.09 through 8.11. The agreement between the simulation and experiment is not up to par, particularly in couples # 1, 4, 10 and 11. The reason for this is not immediately obvious, although Wan did report observing Kirkendall porosity (due to the coalescence of a large number of vacancies) that render both the concentration-penetration profile and the Kirkendall shift measurements suspect. Furthermore, as can be seen from figure 8.13, these couples represent the highest values for lattice velocity which in turn helps explain the Kirkendall porosity. One possible conjecture that explains the flattening of these paths in the middle (where the concentration of zinc is essentially constant) is that in the presence of porosity vapor transfer of zinc takes place and therefore the 'diffusion' of zinc is almost instantaneous.

Figure 8.12 shows an example (couple # 9) of the computer generated concentration-penetration and the Kirkendall shift profiles. It is evident that the variation of the lattice velocity along the diffusion direction which is reflected in the Kirkendall shift profile can be quite complicated. For

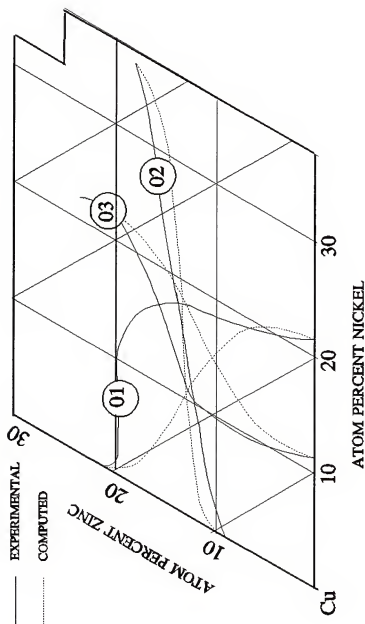


Figure 8.09: A comparison of the composition paths in the Cu-Ni-Zn system studied by Wan,⁸ for couples # 1-3, with the computed paths according to the jump frequency model presented in figure 8.08.

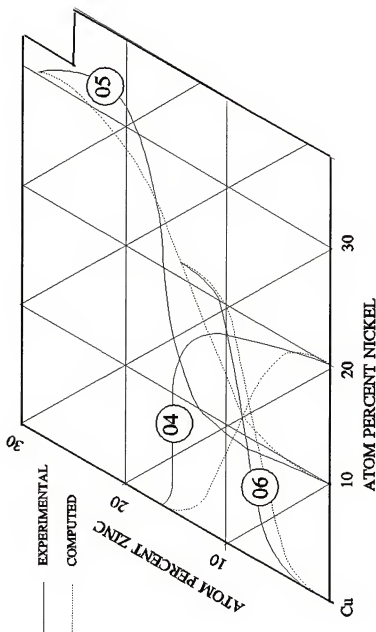


Figure 8.10: A comparison of the composition paths in the Cu-Ni-Zn system studied by Wan,⁸ for couples # 4-6, with the computed paths according to the jump frequency model presented in figure 8.08.

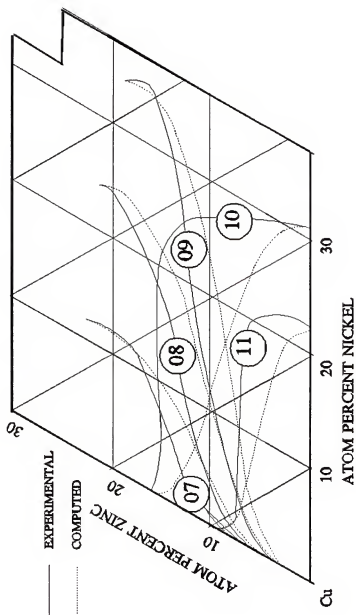


Figure 8.11: A comparison of the composition paths in the Cu-Ni-Zn system studied by Wan,⁸ for couples # 7-11, with the computed paths according to the jump frequency model presented in figure 8.08.

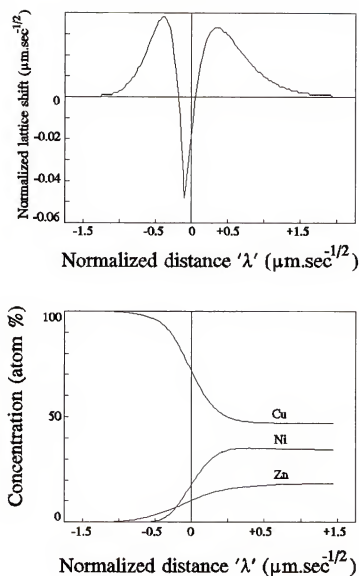


Figure 8.12: An example of the Kirkendall shift and concentration profiles in the Cu-Ni-Zn system (couple # 9, see table 8.03), generated by computer simulation. Wan⁸ measured the Kirkendall shift at the original weld interface, and these values are compared with the simulations in the next figure.

this reason it may not be possible to divine an understanding of lattice motion from just one set of markers (placed at the original weld interface. In this case, for instance, the marker movement will show a slight negative value, while on both sides of the marker the lattice movements are much larger and change signs.

Notwithstanding the above mentioned drawbacks, the computed marker movements are plotted against the experimentally measured ones in figure 8.13. In general, there appears to be a one to one correspondence between the two values (i.e., they are correlated). Couples # 1, 4, 10, 11 do not fit the straight line relationship very well. In all of these couples, the composition paths show a region of constant Zn composition. It is very well possible that a separate explanation is necessary to account for the behavior of these couples. For example, there could be a mechanism other than diffusion, such as the short-circuiting of the concentration profile by vapor transport of zinc along surfaces created by Kirkendall porosity.

Discussion

The simulations in the above three systems suggests a systematic way of exploring diffusion in a composition range of interest in ternary and higher order multi-component isomorphous systems. Unlike the TFA, one would pick a *single couple* in this range, and model the jump frequencies so that

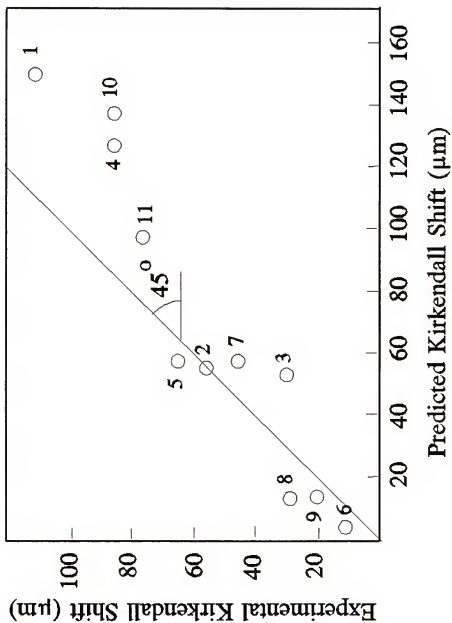


Figure 8.13: A comparison of the measured Kirkendall shifts and those predicted by the computer simulations in the Cu-Ni-Zn system. The couple #'s are as in table 8.03.

they explain the concentration-penetration profile, the composition path and the Kirkendall shift profile for this couple. This model, of course, is by no means unique and therefore its correctness must be tested by selecting *another couple* in the same composition range. The model is then revised to take the behavior of both couples into account. As subsequent couples are investigated, the model is adjusted appropriately until the desired level of confidence is reached, about the model's predictive ability. At this point, one can *predict* with a measure of confidence depending upon the robustness of the mode, *the behavior of any other arbitrarily chosen couple* in the composition range of interest. This type of analysis comes in particularly handy in experimental work on diffusion which seems, for the most part, unfortunately restricted to a narrow composition range of interest to the researcher. By contrast, the TFA generates a series of numbers, scattered over the whole Gibbs triangle (interdiffusion coefficients) whose physical meaning is abstruse.

The models used in the above comparisons are also relatively simple in terms of the input parameters. For instance, the atomic volume, jump distance etc. were assumed to be 'typical' figures, disregarding the actual size of the atomic species involved. Despite the *naivete* evident in such an analysis, the agreement between model and experiment is gratifying. These additional physical considerations, such as

the concentration dependence of the molar volume can easily be accommodated into the computer models with minimum effort. As a matter of fact, since the model is strictly dependent only on the variation of the effective mean jump frequency of a given species in a given volume element, the JFA is, in principle, capable of handling such complex situations as thermal and electrical gradients in addition to the chemical potential gradient due to changes in composition.

One last point of interest is that the Kirkendall shift, which is often not even measured, gives an important clue to the modelling of the Γ 's. Although the measurement of the shifts all along the diffusion direction is no easy task, it might well be worth the extra effort, since this information allows the researcher to produce a more accurate model of the jump frequencies that are consonant with the experiments.

The next chapter will address the question of a moving planar interphase interface in binary multi-phase couples, and conclude with a glimpse at attempts to model diffusion in ternary two-phase systems, and the attendant difficulties.

CHAPTER 9

JFA IN MULTI-PHASE SYSTEMS

The problem of interface migration due to diffusion is of importance in such varied phenomena as growth and dissolution of second phase precipitates in two-phase alloys, coarsening of the precipitate phase in dispersion-strengthened systems, oxidation and other surface processing phenomena and so on. In most situations of practical import, the problem is complicated by such factors as the geometry of the moving interface, finite boundary conditions etc. Therefore, perhaps the logical starting place for studying multi-phase diffusion (which is complicated enough in its own right) is with semi-infinite couples where the phase boundary remains planar and moves in the direction dictated by diffusion.

The Moving Phase Boundary Problem

Consider a simple eutectic phase diagram between components A and B with the terminal phases being α and β respectively {see figure 9.01, for example}. A diffusion sandwich made of pure A and pure B will immediately form an α - β phase boundary at the weld interface. In general, the interface reaction rate is fast enough to form a local equilibrium (appropriate to the temperature of the anneal) at

this interphase interface. Subsequently, the diffusion of A into the B-rich region and vice versa results in a phase transformation reaction at the interface. In consequence, one or the other of the two phases grows at the expense of the other, with an attendant displacement of the interface. This interface motion is directly related to the fluxes at the interface as well as the interface compositions by the interface accommodation equation (IAE).⁵⁹

$$\frac{d\xi}{dt} = \frac{J_k^{\beta\alpha} - J_k^{\alpha\beta}}{C_k^{\beta\alpha} - C_k^{\alpha\beta}} \quad (9.01)$$

where ξ is the position of the interface at time 't', $J_k^{\beta\alpha}$ and $J_k^{\alpha\beta}$ are the *interdiffusion fluxes* at the phase boundary, measured in the laboratory frame, of component k on the β and α sides respectively, and $C_k^{\beta\alpha}$ and $C_k^{\alpha\beta}$ are the corresponding equilibrium interface concentrations.

The IAE is nothing more than a mass conservation statement at the interphase interface. However, since the fluxes in this equation are interdiffusion fluxes, while those generated by the computer in the JFA are intrinsic, equation 9.01 needs to be recast in these terms.

In any reference frame, the flux of species k at any point is related to its concentration and its velocity of motion with respect to that frame as follows

$$J_k^I = C_k^I \cdot v_k^I \quad (9.02)$$

Here, the superscript I refers to the phase in which the volume element of interest lies. Furthermore, in the

laboratory frame, subject to the assumption that the average molar volume weighted velocity of the atom is zero, which seems to be a reasonable assumption to make in condensed solids where convective effects are negligible,¹¹ one can write

$$\sum_{k=1}^n \mathbf{J}_k^I = 0 \quad (9.03)$$

so that there are only $n-1$ independent fluxes in an n -component system in the laboratory frame of reference. {Note: \mathbf{J} in bold lettering denotes that this flux is being measured in the laboratory frame}.

Associated with each point in the system is a lattice velocity v_L . If we superimpose this lattice velocity on the laboratory frame at all points, we obtain what is known as the Kirkendall frame of reference. In this reference frame, the fluxes are all *intrinsic* and are given by

$$J_k^I = C_k^I (v_k^I - v_L^I) = \overline{J}_k^I - C_k^I \cdot v_L^I \quad (9.04)$$

which, when summed over k , yields

$$\sum_{k=1}^n J_k^I = -\sum_{k=1}^n C_k v_L = -C v_L \quad (9.05)$$

where C is the total concentration of atoms per unit volume. {Note that the left hand side of equation 9.05 is also equal to $-J_v$, the vacancy flux in the volume element, and that C is the reciprocal of the molar volume, Ω , so that $J_v = v_L/\Omega$ }

In this relationship, the total atom concentration per unit volume, C (or its reciprocal Ω) is assumed to be

independent of composition. Using equations 9.04 and 9.05, and after suitable algebraic manipulations, the IAE (equation 9.01 can be rewritten in terms of the intrinsic fluxes as

$$(1/\Omega) \cdot \frac{d\xi}{dt} = \frac{(J_k^{\beta\alpha} - J_k^{\alpha\beta})}{(X_k^{\beta\alpha} - X_k^{\alpha\beta})} - \frac{(X_k^{\beta\alpha} \sum_{k=1}^n J_k^{\beta\alpha} - X_k^{\alpha\beta} \sum_{k=1}^n J_k^{\alpha\beta})}{(X_k^{\beta\alpha} - X_k^{\alpha\beta})} \dots (9.06)$$

where X_k^i 's are the mole fractions of the component k on either side of the interface.

As in equation 9.05, the molar volume Ω is assumed independent of composition, and furthermore independent of the phase in which it is measured.

Equation 9.06 can now be directly incorporated into the computer simulation program for calculating the new value of ξ after every incremental time step. In what follows, this idea is applied to binary two-phase systems as well as systems in which an intermediate phase can form and grow at the diffusion temperature. Problems associated with extending the approach to ternary and higher order systems are briefly addressed at the conclusion of this chapter.

Before proceeding any farther, it might be instructive to take a more detailed look at equation 9.06. First of all, like the IAE {equation 9.01}, this equation applies to each of the components in a multi-component system. However, the two equations for the binary case are not independent, a fact that is easily verified by transforming equation 9.06 for component A by using the relationship that the sum of the mole fractions of the two components is one at all points, and arriving at

the same equation for component B. In the case of ternary systems, as explained in detail later in this chapter, there is a bundle of tie-lines from which the system may choose the equilibrium interface compositions. Since each of these tie-lines is completely characterized by specifying any one of the six interface compositions, there are two independent variables, namely ξ , and an interface composition of choice. The bundle of tie-lines have to be modelled suitably at the annealing temperature. In general, for an n-component system, there are n-1 independent statements of equation 9.06 and hence n-2 phase diagram variables. These variables, together with ξ make the system of equations determinate.

Second, equation 9.06 contains certain key quantities that are instrumental in determining the direction and the extent of interface migration during diffusion. Basically, the denominator contains the difference between the equilibrium interface compositions (expressed as mole fractions) of any one of the components on the β and α sides of the interface. Other things being equal, the interface shift will be small, whenever this difference (determined by the phase diagram) is large. The two other key quantities are in the numerator. The first is the imbalance in the flux of the species in question across the interface, while the second is a sort of weighted imbalance in the two vacancy fluxes on either side of the interface, weighted according to the equilibrium mole fraction of this component on either side of

it. These two features of equation 9.06 will appear again and again in the interpretation of the results of the simulations that are described below.

In a recently published work, van Loo et al.⁵⁴ have derived a relationship (their equation 7) which is essentially the same as equation 9.06. From this equation, the authors proceed to derive an equation that describes the interface motion in what they call the Kirkendall frame, which is a reference frame fixed with respect to the lattice (and hence moves with it with respect to the laboratory frame). Finally, using this relationship, they calculate the concentration profiles, the position of the interface and the position of the Kirkendall markers placed at the original weld interface, for binary two phase couples using a 'computer-assisted finite-difference method'. Although equation 9.06 (and hence their equation 7) is valid subject to the restrictive assumptions mentioned, these authors calculate some scenarios that are plainly impossible. In some cases, the markers assume two different positions after diffusion and, as if this is not preposterous enough, they have even presented a case where the markers vanish! In their words, "the behavior of the inert markers placed at the original interface at $t=0$ is difficult to imagine".⁶⁰ The exact source of their anomalous results is not evident, but it would appear that their confusion starts at the point where they attempt to seek a correspondence between the laboratory frame and their

Kirkendall frame by referring to *two different origins for the K-frame, for each of the phases, that don't even necessarily lie in the phase under question*. It is easy to imagine compounding of this difficulty in their analysis when it extended to multi-phase diffusion. For instance, in diffusion couples involving the *formation and growth of an intermediate phase*, this phase doesn't even exist at the outset of the process and hence it would be meaningless to speak of a Kirkendall origin for it.

Planar Interface Migration in Binary Two-phase Systems

Using equation 9.06 and the scheme outlined in chapter 6 for using the jump frequency approach, we are now in a position to undertake a survey of the various possible situations that arise during the course of diffusion in a binary two-phase system with a planar interphase interface that moves with time along the diffusion direction. In order to achieve this goal, a strategy must be devised for characterizing the variability of the system, in terms of the thermodynamics and kinetics as well as in terms of the experimental parameters such as the end-point compositions in a semi-infinite couple. This is done in the following fashion.

In contrast with isomorphous diffusion couples, the variability of the system dramatically increases as one begins to study multi-phase systems. First of all, instead of having

two independent jump frequencies and a possible composition dependence, there are now four different jump frequencies in a two-phase system (one for each component in each phase), all of which may once again be concentration dependent. Second, the phase diagram, which was of no consequence in the isomorphous case, introduces three new parameters in the simple binary two-phase case. These are, as illustrated in figure 9.01,

(A) the proximity of the left hand side end composition, which is in the one-phase field, to the phase boundary {labelled 'x' in figure 9.01},

(B) The width of the two-phase field {labelled 'w' in figure 9.01}, and (C) the proximity of the right hand side end-point composition to its phase boundary {labelled 'y' in figure 9.01}.

The situation is even more complicated for multi-phase systems with an intermediate phase, from the point of view of making a *comprehensive survey* of all possible variations in the system. Therefore, the simulations that were carried out for these cases, although *systematic*, are more *exploratory and inquisitive in nature* designed to ferret out *trends in behavior*, as well as to gain a better understanding of the lattice velocity profiles and the phase boundary migration kinetics during diffusion using the power and versatility of the JFA.

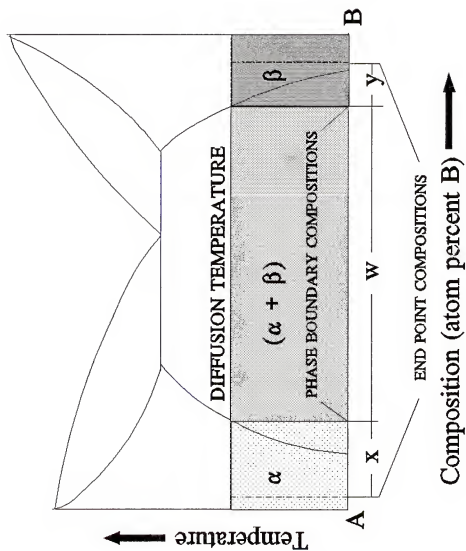


Figure 9.01: An illustration of the variability in binary two-phase diffusion couples, introduced as a consequence of the shape of the phase diagram and the end-point compositions chosen. The relative widths of 'x', 'y' and 'w' control the kinetics of diffusion.

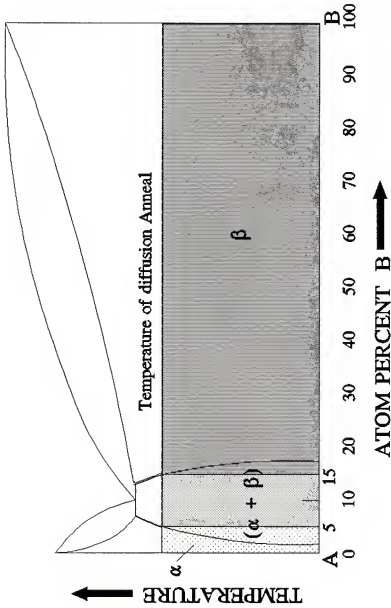
The binary two-phase case

In these simulations three different phase diagrams were used as input, in conjunction with *sixteen* combinations of jump frequencies {see figures 9.02 - 9.04, table 9.01}, as described below. The three phase diagrams are:

- (I) a narrow two-phase field (5 to 15 atom percent B) toward the A-end of the phase diagram,
- (II) a wide two-phase field (5 to 95 atom percent B) almost spanning the entire composition range, and
- (III) an asymmetrical two-phase field (5 to 50 atom percent B) toward the A-end.

In the isomorphous case, the jump frequencies were broadly classified as fast, medium and slow. In this case, only two values were assigned to the jump frequencies (5 and 10 million jumps per second) with no compositional dependence. Even so, there are, as mentioned, 16 combinations of these Γ 's for each one of the above phase diagrams. These are listed in table 9.01.

In presenting the results of these simulations graphically, whenever a measure of distance is involved (except for the interface shift profiles), it is normalized by dividing by the square root of time, so that the resulting figure is independent of annealing time.



PHASE DIAGRAM I : Narrow two-phase field toward the A-end

Figure 9.02: The first of the three phase diagrams explored in the simulation of planar phase boundary migration during diffusion in binary two-phase systems. For each of these phase diagrams, 16 different combinations of jump frequencies (see table 9.01) were used as input.

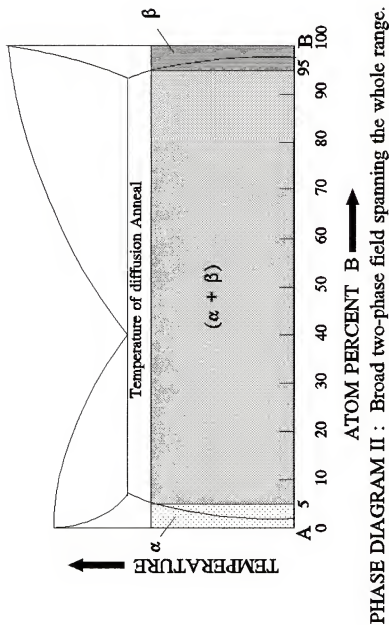
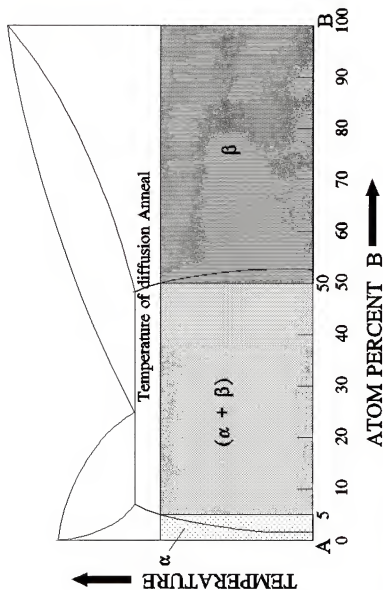


Figure 9.03: The second of the three phase diagrams explored in the simulation of planar phase boundary migration during diffusion in binary two-phase systems. For each of these phase diagrams, 16 different combinations of jump frequencies (see table 9.01) were used as input.



PHASE DIAGRAM III : Asymmetrical two-phase field toward the A-end

Figure 9.04: The last of the three phase diagrams explored in the simulation of planar phase boundary migration during diffusion in binary two-phase systems. For each of these phase diagrams, 16 different combinations of jump frequencies (see table 9.01) were used as input.

Table 9.01: The SIXTEEN combinations of the four jump frequencies (for each of the two components 'A' and 'B' in each of the two phases ' α ' and ' β ') that were used in the exploratory survey of interface migration in binary two-phase diffusion couples.

COUPLE NUMBER	Γ_A (in α)	Γ_A (in β)	Γ_B (in α)	Γ_B (in β)
	(in millions of jumps per second)			
01	1	1	1	1
02	1	1	5	5
03	1	1	1	5
04	1	1	5	1
05	5	5	1	1
06	5	5	5	5
07	5	5	1	5
08	5	5	5	1
09	1	5	1	1
10	1	5	5	5
11	1	5	1	5
12	1	5	5	1
13	5	1	1	1
14	5	1	5	5
15	5	1	1	5
16	5	1	5	1

The Concentration Profiles

The resulting concentration profiles for phase diagrams (I), (II) and (III) are presented in figures 9.05 through 9.07. There is significant interface movement in phase diagram (I), while there is hardly any shift in diagram (II), with diagram (III) falling somewhere in between. These effects are at least qualitatively explained with the help of equation 9.06.

In the case of phase diagram (II), the denominator in equation 9.06 is too large to allow for any significant interface shifts, while this denominator has the smallest value for diagram (I) {narrow two-phase field}, with diagram (II) falling in between. This demonstrates that, for a given set of input parameters (in particular the jump frequencies), the width of the two-phase field has a direct effect on the magnitude of the interface shifts.

Focussing on the results for diagram (I) {figure 9.06}, we see that the smallest shifts belong to couples 01, 04, 13 and 16. These couples correspond to the smallest values of Γ 's of both components in the β phase. Thus, even though the concentration gradient in the β -phase is high (with the phase boundary so far removed from pure B, which is the end-point composition), the fluxes are relatively small. Conversely, for couples 06, 07, 10 and 11, where the Γ^β 's are the highest, the interface shifts are also relatively high. The

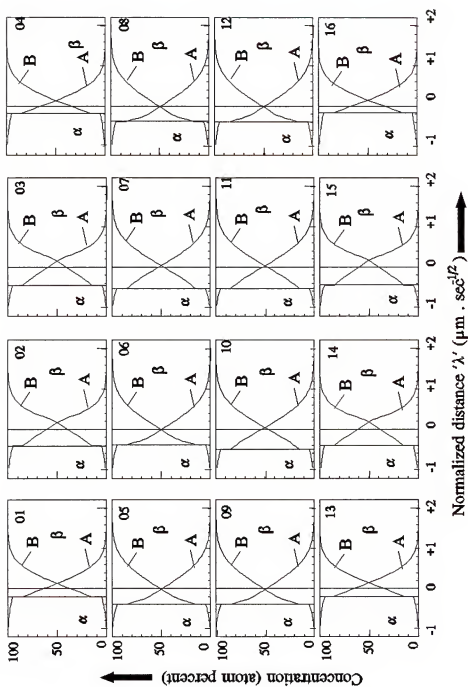


Figure 9.05: The concentration profiles for the sixteen combinations of Γ 's considered, for phase diagram 'I,' (see figure 9.02, table 9.01).

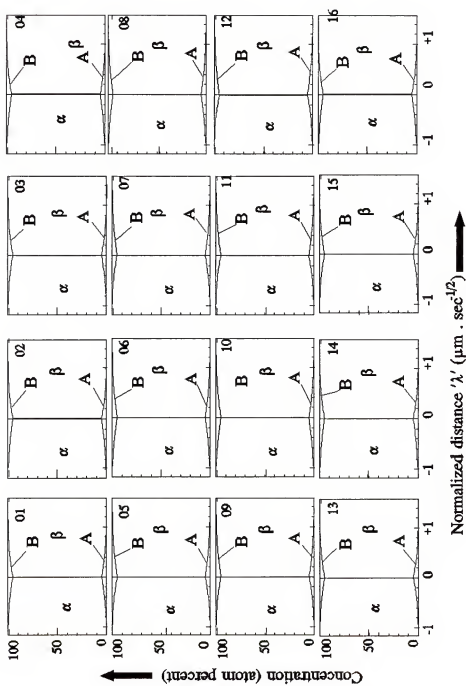


Figure 9.06: The concentration profiles for the sixteen combinations of Γ 's considered, for phase diagram 'II' (see figure 9.02, table 9.01).

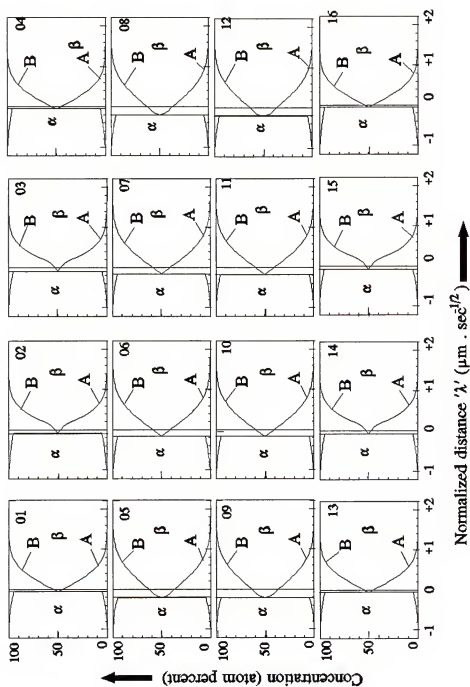


Figure 9.07: The concentration profiles for the sixteen combinations of Γ 's considered, for phase diagram 'III' (see figure 9.02, table 9.01).

gradients on the α -side of the couple are always small (with the phase boundary close to pure A, the end-point composition) and therefore the effect of varying the Γ^α 's is relatively important.

The concentration profiles of diagram (III) depict the same qualitative phenomena, as far as the interface shifts are concerned, as diagram (I), although less dramatically so.

The Kirkendall Shift Patterns

The Kirkendall shift patterns for the 16 couples. for phase diagrams (I), (II) and (III) are presented in figures 9.08, 9.09 and 9.10 respectively. The first point to note is that *there is no Kirkendall shift in the on-diagonal couples # 1, 6, 11 and 16.* Referring back to table 9.01 it can be seen that, in these couples, both A and B have the same value of Γ in a given phase and, in that consequence, there is no imbalance in fluxes and no lattice shift. As a corollary to this effect, it should also be noted that this lack of shift can be true in one or the other of the phases (but not both), when $\Gamma_A = \Gamma_B$ in that phase {see, for example, couple # 03 or 08}.

Complicating matters further is the moving phase boundary. As the problem is set up in the simulation, the phase boundary is not tied to any slice element. Rather, it sweeps across the slices in the direction driven by diffusion. Therefore, a given slice may start its existence in one phase,

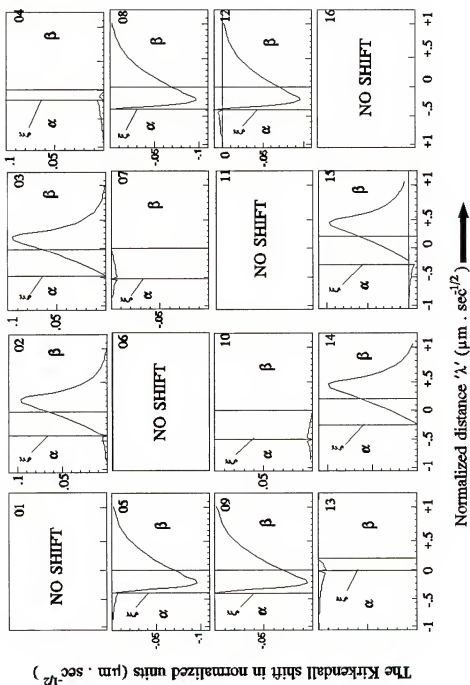


Figure 9.08: The Kirkendall shift patterns for the sixteen combinations of Γ 's considered, for phase diagram ' I' ' (see figure 9.02, table 9.01).

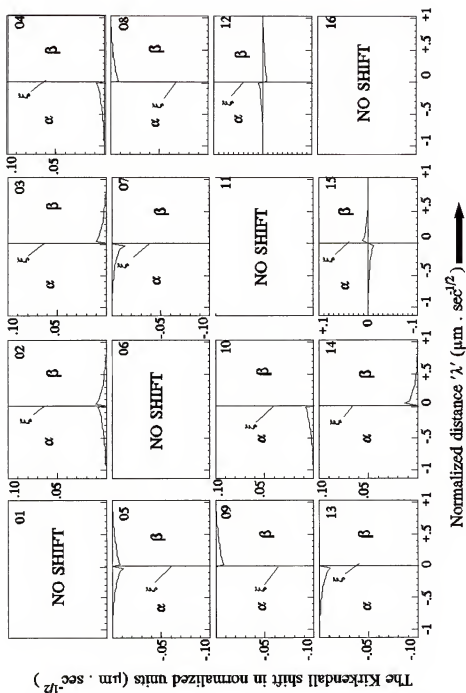


Figure 9.09: The Kirkendall shift patterns for the sixteen combinations of Γ 's considered, for phase diagram 'II' (see figure 9.02, table 9.01).

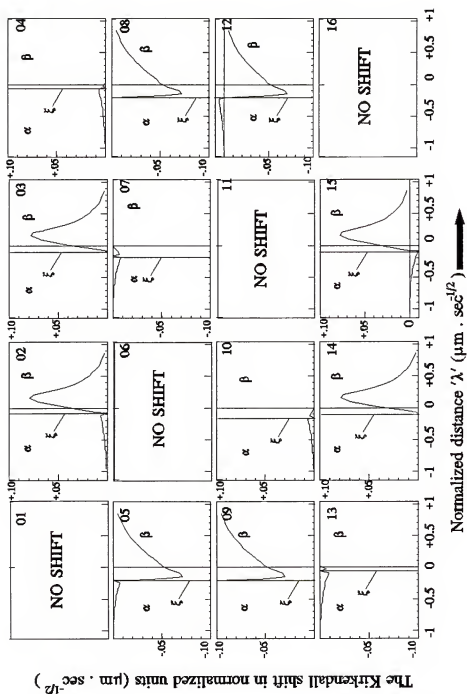


Figure 9.10: The Kirkendall shift patterns for the sixteen combinations of Γ 's considered, for phase diagram 'III' (see figure 9.02, table 9.01).

only to find itself in another at a later time. If the jump frequencies are such that there is a flux imbalance in one of the phases, but not the other, then this slice exhibits a lattice shift up to the point in time when it is in the appropriate phase prior to the interface sweeping across. Take, for example, the profile of couple # 4. In this case, there is no lattice shift in the β -phase, and yet there is a small but significant shift inside the β -phase from the α - β interface to the original zero. This part of the couple lived the early part of its existence during diffusion in the α -phase and hence was shifting in response to the flux imbalances in the α -phase, up to the point where it was transformed into the β -phase.

Finally, in all of the couples, the Kirkendall shift in the α -phase is small. This is due to the fact that the concentration difference, and hence the gradient, is small in this phase. In turn, this means that the fluxes are small and so is the shift, which is proportional to the algebraic sum of these fluxes. For phase diagram (II) {figure 9.09}, this observation applies to both phases, since the two-phase field almost spans the entire composition range of the binary system.

These shift patterns also serve to underscore the fact that the lattice velocity profile at the interface is discontinuous. Therefore, the Kirkendall markers placed at the original interface, which now find themselves in one phase

or the other, tell only an insignificant part of the story about lattice adjustments.

The Interface Shift Patterns

The position of the interface is plotted as a function of the square root of time, for phase diagrams (I), (II) and (III) in figures 9.11, 9.12 and 9.13 respectively. Judging from the premises under which the simulation program has been developed, one would expect a straight line relationship between the interphase interface shift and $t^{1/2}$. Except for a transition period at early times during simulation, this is indeed the case for diagram (I) {figure 9.11}, where the shifts are disk large, i.e., in tens of μm . On the other hand, when the shifts are small, as for all the couples in diagram (II) and some in diagram (III) {figures 9.12 and 9.13}, the straight line relationship falters. This is due to the scale of the finite-difference algorithm which needs to be refined as the shifts become smaller.

Growth of an Intermediate Phase During Diffusion

The dramatic increase in the number of possible variations of the input parameters due to the introduction of two phases and the resultant difficulties in pursuing a systematic explorations of such systems were discussed earlier in this chapter. Now consider the phase diagram shown in figure 9.14. At the temperature of diffusion anneal we have, as possible variations in input (subject, of course, to the

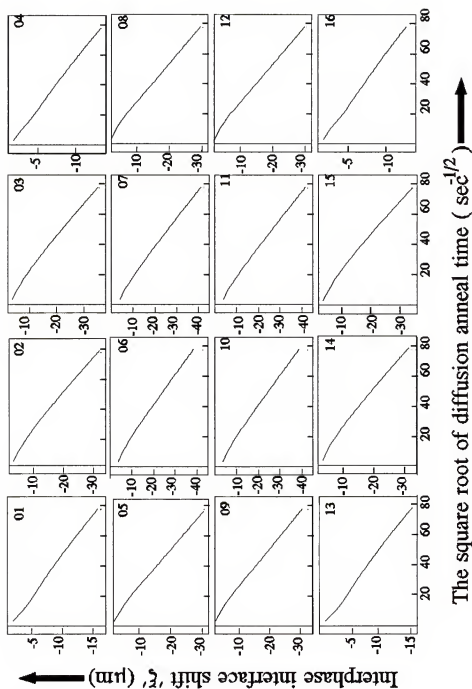


Figure 9.11: The interface shift patterns for the sixteen combinations of Γ 's considered, for phase diagram 'I' (see figure 9.02, table 9.01).

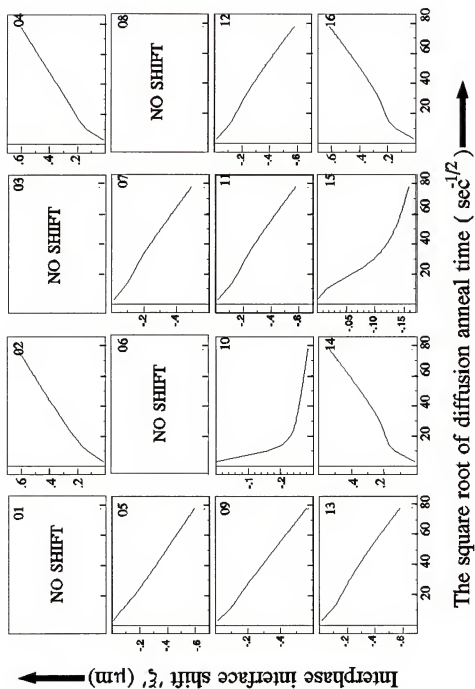


Figure 9.12: The interface shift patterns for the sixteen combinations of Γ 's considered, for phase diagram 'II' (see figure 9.02, table 9.01).

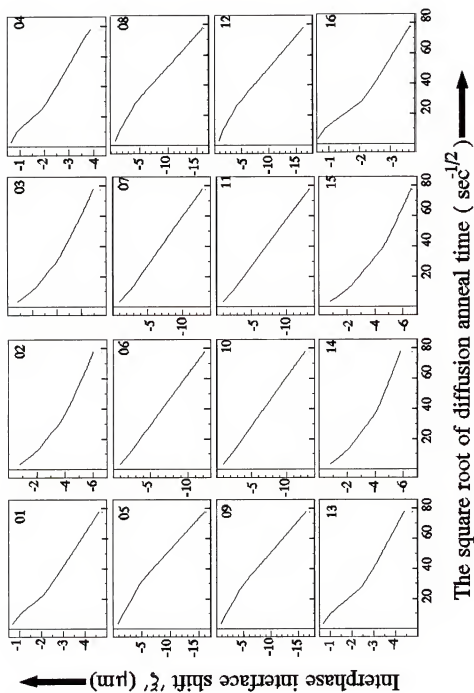


Figure 9.13: The interface shift patterns for the sixteen combinations of Γ 's considered, for phase diagram 'III' (see figure 9.02, table 9.01).

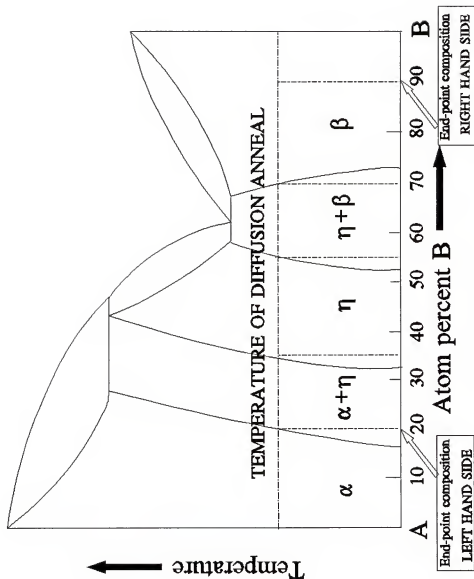


Figure 9.14: The phase diagram employed to illustrate diffusion-induced formation and growth of the intermediate phase (η). The end-point compositions are in the one-phase fields (α , β). The computer-generated kinetic information for this couple is presented in figures 9.15 to 9.17.

conditions that they all have to add up to a maximum of 100%), the following:

- (i) a composition range in the one-phase field α ,
- (ii) the width of the α - η two-phase field,
- (iii) the width of the one-phase field η ,
- (iv) the width of the η - β two-phase field, and
- (v) a composition range in the one-phase field β .

If we were to classify the above five ranges in a very simple way, e.g., narrow, medium and broad, the number of possible combinations becomes large. In addition, as far as the jump frequencies are concerned, there are now *six* different and independent inputs, namely one for each component in each of the three phases, not to mention the possible dependence of each one of these Γ 's on composition!

In view of these considerations, the following strategy has been adopted for a preliminary exploration of diffusion in couples with an intermediate phase. First, a typical example, where the intermediate phase η forms and grows, is produced by way of illustrating the proficiency of the simulation program. Next, for a given phase diagram, using various combinations of Γ 's as input, the maximum width of the one-phase composition range (i.e., the minimum amount of solute in the end-point composition), below which the η -phase will not form during diffusion are computed and tabulated. Then, for a given configuration of the η -phase, and given the pure components as the end-point compositions, and once again using various

combinations of Γ 's as input, the minimum widths of the two-phase fields (i.e., the terminal solubility limits), below which the η -phase will not form, are also computed and tabulated. In both of the above tables, the requisite critical compositions are arrived at through a technique of bracketing and laddering, i.e., the simulation is run a number of times, each time varying the input, thus zeroing in on the desired critical value. Finally, once again holding the configuration of the η -phase constant, and holding the one-phase composition ranges within a narrow limit, the width of the two two-phase fields are varied to study the effect on the parabolic rate constant for interface shift. In this last case the jump frequencies were assumed to be constant and independent of composition.

A Typical Example

For the purpose of this simulation, the phase diagram shown in figure 9.14 was used as input. The end-point compositions are taken to be pure A on the left hand side of the couple and 10 atom % A on the right hand side. The jump frequencies are as follows: $\Gamma_A^\alpha : \Gamma_A^\eta : \Gamma_A^\beta :: 0.5 : 1 : 0.1$ and $\Gamma_B^\alpha : \Gamma_B^\eta : \Gamma_B^\beta :: 1 : 5 : 1$, with all quantities in millions of jumps per second and independent of composition.

In all simulations involving the formation and growth of an intermediate phase, the computer program is set up such that, initially, there is a thin layer (two slices thick) of the intermediate phase. Then, if the displacement of the two

interphase interfaces is such that this thickness of the intermediate phase grows with time, the program is run to its completion. Otherwise, the computer reaches the conclusion that the intermediate phase does not grow (and hence does not form in the first place) and terminates the program.

Figure 9.15 shows the concentration-penetration profile. The distance in this and the next figure is measured from the left hand side of the couple, removed from the diffusion zone. Further, these distances are normalized by dividing by $t^{1/2}$ so as to make the graphs independent of annealing time.

Figure 9.16 is the Kirkendall shift profile. The maximum value of the shift occurs inside the η -phase. This is to be expected, for this region has large composition gradients as well as relatively large Γ 's (as the problem has been set up) and hence large imbalances in the fluxes.

In figure 9.17, the displacements of the α - η and the η - β interfaces, as well as the thickness of the η -phase are plotted as a function of $t^{1/2}$. After a transition period, these curves tend to straighten out, as would be expected. The values of the parabolic rate constants, i.e., the slopes of the straight portion of these curves, are also indicated in this figure (a negative value is a shift to the left, and a positive value to the right).

The maximum value of the one-phase composition for Growth

For these combinations the phase diagram shown in figure 9.18 was chosen. In this diagram, the η -phase is narrow and

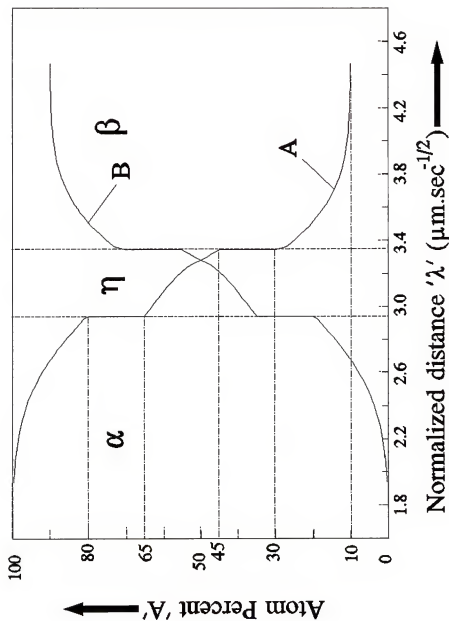


Figure 9.15: The concentration profiles in a binary three-phase system for a typical couple in which the intermediate phase (η) forms and grows during diffusion. The thickness of ' η ' is determined by the motion of the α - η and η - β interfaces. By convention, a shift to the right is deemed positive.

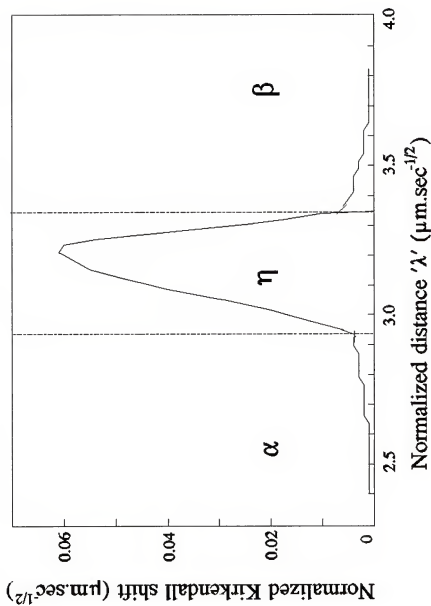


Figure 9.16: The Kirkendall shift pattern for the couple shown in figure 9.15. Both axes are normalized so as to be independent of time.

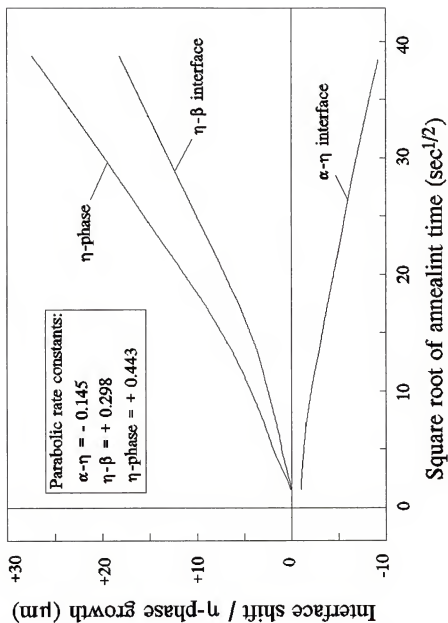


Figure 9.17: The interphase interface shifts and the consequent growth of the η -phase, plotted against the square root of time. By convention, shifts to the right are positive. After an initial period of transition, these growth/shift rates vary parabolically with time. The growth of the η -phase is the algebraic sum of the displacement of the α - η and the η - β interfaces.

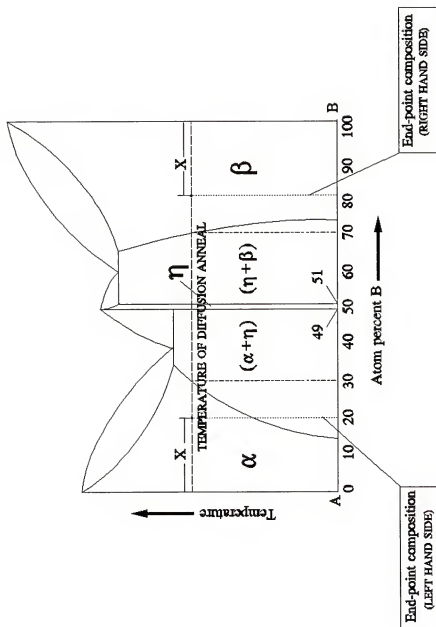


Figure 9.18: The phase diagram used to generate table 9.02. At the diffusion temperature, the η -phase is narrow and in the middle, flanked by symmetrical two-phase fields $(\alpha+\beta)$ and $(\eta+\beta)$, each 19 atom percent wide. For various combinations of the jump frequencies as input, the minimum values of ' x ,' below which the η -phase will not form, are computed and presented in table 9.02.

is in the middle, flanked by two symmetrical two-phase fields, 19 atom percent wide. In these simulations, the problem is set up, as before, with a thin layer (two slices thick) of the intermediate phase, placed between two thick slabs of material with the end-point compositions in the terminal phases. For a given set of jump frequencies as input, the value of X (see figure 9.18), which fixes the end-point compositions is varied through several simulation runs until a critical value is found, for which the η -phase neither dissolves nor grows. The η -phase will only form and grow above this value of X . Ostensibly, the gradient generated due to the difference between the end-point compositions at the outset of the experiment is so high that system fails to recognize the presence of an intermediate phase. Under these circumstances, the α and β phases form an interface with a meta-stable equilibrium condition, and the system behaves as if the intermediate phase is non-existent at the temperature of anneal.

The pertinent values of X for the various combinations of the jump frequencies are shown in table 9.02. The most striking feature of this table, although perhaps not all that surprising, is that it is diagonally symmetric. That is, the values obtained for X are the same for entry $[i,j]$ in the table as they are for entry $[j,i]$. This is due to the symmetry of the phase diagram chosen, that allows for

β	α	FAST			MEDIUM			SLOW		
		η			η			η		
FAST		FAST	MEDIUM	SLOW	FAST	MEDIUM	SLOW	FAST	MEDIUM	SLOW
		26.1	28.0	29.5	25.5	27.7	29.4	24.4	27.2	29.3
MEDIUM		η			η			η		
		FAST	MEDIUM	SLOW	FAST	MEDIUM	SLOW	FAST	MEDIUM	SLOW
		25.5	27.7	29.4	24.7	27.3	29.3	23.2	26.5	29.1
SLOW		η			η			η		
		FAST	MEDIUM	SLOW	FAST	MEDIUM	SLOW	FAST	MEDIUM	SLOW
		24.4	27.2	29.3	23.2	26.5	29.1	20.3	25.0	28.7

Table 9.02: Computer generated values for the end-point compositions (in atom percent of solute), below which the η -phase will not form, for the phase diagram shown in figure 9.18. Both Γ_A and Γ_B in a given phase are set equal so that there is no lattice motion. Twenty seven different combinations of Γ 's are used in the simulations, with Fast:Medium:Slow :: 10:5:1 jumps/sec.

interchanging the labels α and β . In addition, note that maximum flexibility occurs when the jump frequencies are slowing the η -phase as compared to the α and β phases. The smallest number in Table 9.02 is the first entry in row 3, column 3, which is for the case where the jump frequencies are the fastest in the terminal phases and the slowest in the intermediate phase. Thus this combination of Γ 's provides the widest range of possible end-point compositions that allow for the growth of the η -phase.

Effect of the Two-phase field Width on η -phase Growth

In this study, the diffusion couples consist of the pure components as the end-point composition, as shown in figure 9.19. The phase diagram has a narrow η -phase in the middle. The two two-phase fields are arranged symmetrically around this η -phase. The question to which an answer is sought is: what is the minimum width of these two-phase fields, below which the intermediate phase does not form? In this case, the phase diagram is varied through a series of simulations until the value of this critical minimum is established. Once again, as before, 27 different combinations of jump frequencies were employed as input, with a view to scanning possible trends. The reason for the existence of such a minimum, as explained in the previous case, is that below this minimum, the gradients in the one-phase fields are too high at the outset for the system to form and grow the intermediate phase. In this situation, the terminal phases form an

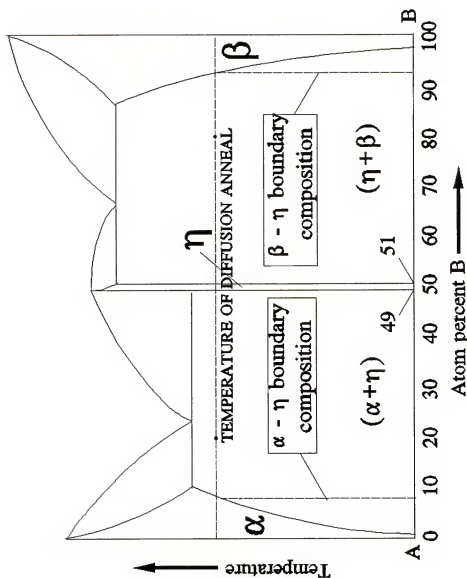


Figure 9.19: The phase diagram used to generate table 9.03. At the diffusion temperature, the η -phase is narrow and in the middle, flanked by symmetrical two-phase fields. For various combinations of T's as input, given pure A and pure B as the end-point compositions, the solubility limit (of B in α or A in β) beyond which the η -phase will not form, is presented in table 9.03.

interface with meta-stable compositions on either side, and the system acts as if there were no η -phase at this temperature.

The values generated by the computer as answer to the above question are presented in table 9.03. This table is also diagonally symmetric (for the same reason as in the previous case) and the maximum flexibility (i.e., the broadest range of compositions for the solubilities in the terminal phases) occurs when atom movements are the slowest in the intermediate phase.

Two-phase Field Width - Effect on the Parabolic Rate Constants

This last series of simulations was designed to explore the effect of the width of the two-phase field on the growth rate of the intermediate phase, *given the configuration of the η -phase (narrow and in the middle), given the end-point compositions (close to the phase boundary) and given a single set of composition-independent jump frequencies*. The η -phase ranges from 49-51 atom percent B, and the end-point compositions are held within 2 atom percent of the phase boundary, in the one-phase field {see figure 9.20}. The jump frequencies which are constant and composition-independent are as follows for either component: $\Gamma_k^\alpha : \Gamma_k^\eta : \Gamma_k^\beta :: 1 : 5 : 1$ millions of jumps per second.

Two sub-cases were explored. In case (1), which is shown in the first six rows of table 9.04, *both two-phase fields were systematically varied from 47 to 2 atom percent*.

α β	FAST			MEDIUM			SLOW		
FAST	η			η			η		
	FAST	MEDIUM	SLOW	FAST	MEDIUM	SLOW	FAST	MEDIUM	SLOW
	8.4	4.7	0.9	11.4	5.8	1.0	16.6	7.9	0.9
MEDIUM	η			η			η		
	FAST	MEDIUM	SLOW	FAST	MEDIUM	SLOW	FAST	MEDIUM	SLOW
	11.4	5.8	1.0	12.2	8.6	1.4	23.3	11.6	2.1
SLOW	η			η			η		
	FAST	MEDIUM	SLOW	FAST	MEDIUM	SLOW	FAST	MEDIUM	SLOW
	16.6	7.9	0.9	23.3	11.6	2.1	35.0	18.6	3.8

Table 9.03: Computer generated values for the solubility limits (in atom percent of solute), below which the η -phase will not form, in couples made of pure A and pure B (see figure 9.19). Both Γ_A and Γ_B in a given phase are set equal so that there is no lattice motion. Twenty seven different combinations of r 's are used in the simulations, with Fast:Medium:Slow :: 10:5:1 jumps/sec.

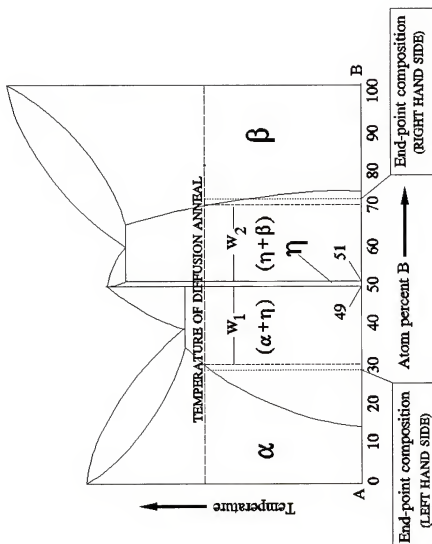


Figure 9.20: The phase diagram used to study the effect of the two-phase field width on the parabolic rate constants representing the displacement of the two interfaces, as well as the growth of the η -phase. The width and position of the η -phase were kept unchanged, while varying w_1 and w_2 . The end-point compositions were kept at 2 atom percent away from the phase boundary in the one-phase field.

CASE #	End-point composition (Left side)	2-phase field width		End-point composition (Right side)	Parabolic rate constants for shift/growth		
		α - η	η - β		α - η	η - β	η
1	0	47	47	100	-0.040	+0.040	+0.080
2	10	37	37	90	-0.047	+0.047	+0.094
3	20	27	27	80	-0.058	+0.058	+0.116
4	30	17	17	70	-0.078	+0.078	+0.156
5	40	7	7	60	-0.128	+0.128	+0.256
6	45	2	2	55	-0.226	+0.226	+0.452
7	0	47	47	100	-0.040	+0.040	+0.080
8	0	47	37	90	-0.038	+0.048	+0.086
9	0	47	27	80	-0.036	+0.063	+0.099
10	0	47	17	70	-0.033	+0.089	+0.122
11	0	47	7	60	-0.026	+0.160	+0.186
12	0	47	2	55	-0.018	+0.299	+0.317

{ ALL COMPOSITION VALUES ARE IN ATOM PERCENT 'B' }

Table 9.04: The values of the parabolic rate constants presented as a function of the two-phase field width. In the first six cases, both w_1 and w_2 are varied from 47 to 2 atom % (see figure 9.21) and in the next six, w_1 is held constant at 47 atom % while w_2 is varied from 47 to 2 atom % (see figure 9.22).

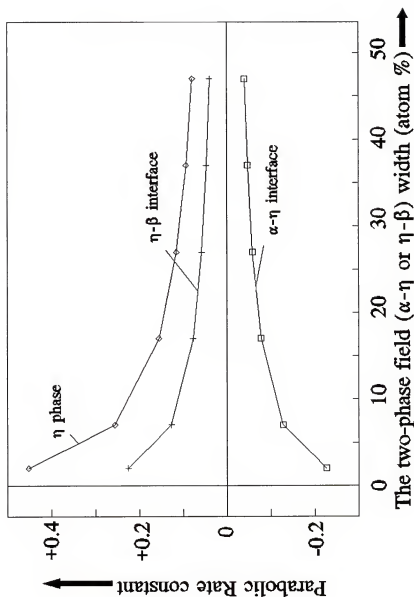


Figure 9.21: The parabolic rate constants plotted as a function of the two-phase field width. In this case, both w_1 and w_2 are varied from 2 to 47 atom percent (see figure 9.20). The end-point compositions are 2 atom percent away from the phase boundary, in the one-phase field. The growth rate of the η -phase diminishes as the two-phase field is widened.

The corresponding end-point compositions are also shown. The last three columns of this table show the parabolic rate constants (i.e., the slopes of the straight lines representing the displacement versus $t^{1/2}$ curve). These values are also graphically represented in figure 9.21. From this graph it is evident that the growth rates decrease as the width of the two-phase field decreases. As mentioned earlier in this chapter, this is as would be expected from an examination of equation 9.06. As the two-phase field is widened, the denominator in equation 9.06 increases and the growth rate drops off.

The second set (the last six rows of table 9.04) is for case (2). In this case, in addition to all other things mentioned before, the width of the α - η field is also held constant, with the η - β field width varying from 47 to 2 atom percent. The pertinent end-point composition values are as indicated. Once again, the last three columns are the computer-generated values for the parabolic rate constants. These are also graphically depicted in figure 9.22. The trend is the same, i.e., the wider the two-phase field, the slower the displacement rates.

In both of the above figures (9.21 and 9.22), a displacement to the right is considered positive, and the thickness of the intermediate phase is simply the algebraic difference between the displacement of the η - β and the α - η interfaces.

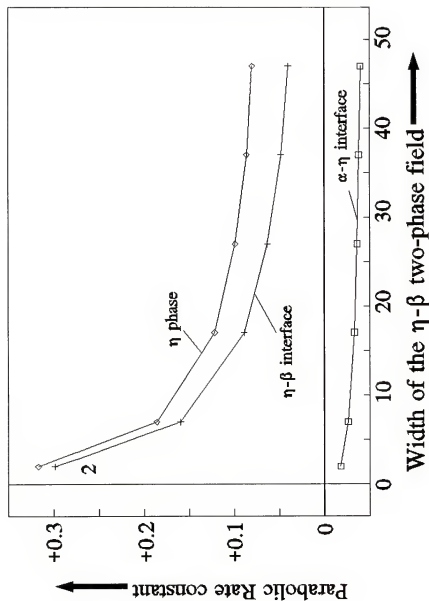


Figure 9.22: The parabolic rate constants plotted as a function of the α - η field width. In this case, w_1 is held constant at 47 atom %, while w_2 is varied from 2 to 47 atom % (see figure 9.20). The end-point compositions are 2 atom percent away from the phase boundary, in the one-phase field. The growth rate of the η -phase diminishes as the two-phase field is widened.

Ternary and Higher Order Systems With Two or More Phases

In discussing equation 9.06 it was pointed out that for an n-component system, there exist (n-1) independent statements for that equation. For example, in the ternary case, there is a bundle of tie-lines that are available for the system to choose from, when the composition paths has to cross the two-phase field. This bundle of tie-lines may be modelled with any number of parameters, but *only one degree of freedom*. For example, specifying any one of the equilibrium interface compositions, in either one of the phases, automatically fixes all the other compositions and hence the tie-line. For example, if we were to characterize the tie-line bundle by the orientation and the length of the lines, then specifying one end-point of this line fixes the other end-point through the model. This is illustrated using the ideal solution model in what follows.

The Ideal Solution Model for Ternary Two-phase Fields

Begin with the condition for equilibrium,

$$\mu_k^{\alpha} = \mu_k^{\beta} \quad (\text{for } k=1, 2, 3) \quad (9.07)$$

i.e., the chemical potential for each component is the same in the two phases. With the presumption that the terminal solid solutions are both ideal, we can write

$$\frac{X_k^\beta}{X_k^\alpha} = \exp \left[\frac{\Delta G^{0\alpha-\beta}}{RT} \right] = K_k \quad (9.08)$$

where the X_k 's are the mole fractions and the ΔG 's are the free energy changes associated with the phase transformation, and K_k 's are parameters defined in the above manner.

In addition we have,

$$\sum_{k=1}^3 X_k^\alpha = 1, \quad \text{and} \quad \sum_{k=1}^3 X_k^\beta = 1 \quad (9.10)$$

Between equation 9.08 and 9.09, we have five conditions and six variables (the equilibrium interface compositions). Thus there is one degree of freedom, for example, any one of the six interface equilibrium compositions. Solving for all the other five interface compositions in terms of X_1^α yields

$$X_2^\alpha = \frac{(K_2 - 1)}{(K_3 - K_2)} + \frac{(K_1 - K_3)}{(K_3 - K_2)} \cdot X_1^\alpha \quad (9.10)$$

$$X_3^\alpha = \frac{(1 - K_2)}{(K_3 - K_2)} + \frac{(K_3 - K_1)}{(K_3 - K_2)} \cdot X_1^\alpha \quad (9.11)$$

$$X_1^\beta = K_1 \cdot X_1^\alpha \quad (9.12)$$

$$X_2^\beta = \frac{K_2(K_3 - 1)}{(K_3 - K_2)} + \frac{K_2(K_1 - K_3)}{(K_3 - K_2)} \cdot X_1^\alpha \quad (9.13)$$

$$X_3^\beta = \frac{K_3(1 - K_2)}{(K_3 - K_2)} + \frac{K_3(k_2 - k_1)}{(K_3 - K_2)} \cdot X_1^\alpha \quad (9.14)$$

Note that, in a Gibbs triangle representation of the isotherm, owing to the nature of equations 9.10 through 9.14, the phase boundaries will be straight lines. An example of such a Gibbs triangle is shown in figure 9.23. A tie-line inside the two-phase field is shown as an example.

It would appear that equation 9.07, taken in conjunction with a model for the tie-line bundle, such as the one shown above for an ideal solution *should* let us determine the tie-line appropriate to the kinetic conditions. Unfortunately, as the computer program is set up, there is a chicken and egg type catch. Equation 9.06 has flux terms, which in turn depend upon the interface compositions, and therefore, a direct evaluation of the interface compositions *ab initio* is not possible. Several unsuccessful attempts were made to start with an initial best guess for the tie-line (for example, the tie line closest to the line joining the end-point compositions) prior to the simulation of diffusion. At the end of each iteration, the program recalculated the tie-line based on equation 9.06. It was hoped that the tie-line composition would go through a transition period where it would fluctuate around or slowly drift toward the eventual tie-line picked by the system. Instead, these attempts have so far resulted in unacceptable values for tie-line compositions (less than 0 or greater than 1), or a perpetually oscillating tie-line composition over a significant range.

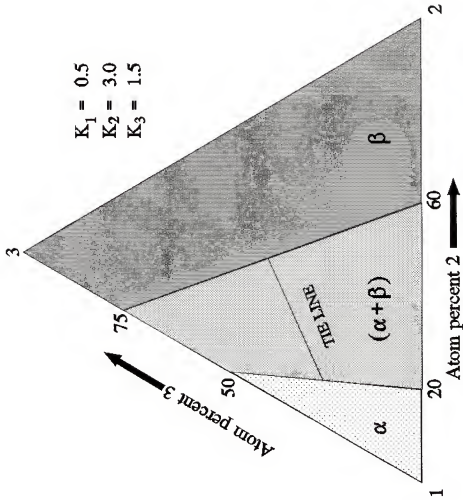


Figure 9.23: An ideal solution model for the bundle of tie-lines in a ternary two-phase field. The parameters K_i define the phase boundaries in terms of thermodynamic quantities. For this model, these phase boundaries are straight lines. Any given tie-line is completely specified by the choice of any one of the six equilibrium interface compositions.

The reason for the lack of success in ternary two-phase system is not obvious at this time. Under certain restrictive assumptions, namely constant interdiffusion coefficients, the phenomenological theory allows for the numerical evaluation of the parabolic rate constant as well as the interface equilibrium compositions, so that the problem is determinate. However, a computer simulation based on the finite difference methods that obviates the need for any assumptions is far more desirable. More work is needed in this area before the problem is successfully resolved. In principle, once a sound mathematical understanding of the process is in place, there is no reason that the computer program cannot be modified to make studies in multi-component multi-phase systems feasible, using the jump frequency approach.

CHAPTER 10
CONCLUSIONS AND RECOMMENDATIONS FOR FUTURE WORK

Conclusions

1. The primary goal of this work, which was to develop and apply a model for the simulation of diffusion in condensed crystalline systems using the jump frequency approach (JFA), has been achieved.

2. As a prelude to the introduction of the JFA, the traditional phenomenological approach to diffusion studies has been reviewed with a view to pointing out its shortcomings in applications involving multi-component or multi-phase diffusion.

3. The concept of the relative penetration tendency (RPT) represents a significant departure from the traditional analyses of diffusion and is a precursor to the development of the JFA. Therefore, an overview of previously published work using the RPT approach has been presented for the purpose of comparing and contrasting it with the JFA.

4. The basic ideas behind the JFA have been developed and a strategy for creating and executing a computer modelling technique for the study of diffusion using the JFA is outlined, using specific examples of varying complexity.

One of these examples is the classic experiment of Darken on the "uphill" diffusion of carbon in steels containing silicon as a substitutional alloying element.

5. A comprehensive survey of diffusion in ternary isomorphous systems has been made using the JFA. The salient features of the results of this survey are discussed in detail. The conclusions reached in this study are compared with those of the RPT approach.

6. The results of some classic experimental studies, in the Fe-Ni-Co, the Cu-Ag-Au and the Cu-Ni-Zn systems have been successfully duplicated using appropriate computer models for the jump frequencies (and their compositional dependence) of the component atoms. Once again, the agreement between these models and the experiment is compared with that of the RPT approach.

7. The question of planar interphase interface migration in two-phase semi-infinite diffusion couples is addressed. A model has been developed for tackling this problem with the JFA. Based on this model, a systematic survey of planar phase boundary migration was made for various combinations of input parameters. The results of these simulations are discussed.

8. Finally, the problem of the formation and growth of an intermediate phase in binary three-phase systems is addressed. Using a suitable computer model, once again based on the JFA, the limits on the various kinetic, experimental and thermodynamic parameters (jump frequencies, end-point

compositions, widths of the phase fields etc.) under which the intermediate phase will form and grow, have been evaluated. These limits are discussed in the light of the insight provided by the JFA.

9. Throughout this work, emphasis has been placed in pointing out that the strength of the JFA over the traditional phenomenology is its ability to produce the entire concentration profile together with the lattice shift patterns that can be *directly compared with the experimental output*, without resorting to any data manipulation. This technique of manipulating the parameters in the theory to accomplish agreement with data, rather than the other way around, has obvious advantages in terms of reducing cumulative errors. Furthermore, the JFA allows the prediction of *patterns of behavior* of the entire system under study, and not just at isolated points scattered throughout the composition triangle.

Recommendations for Future Work

Despite the voluminous appearance of this dissertation, it barely begins to scratch the surface of the possibilities opened up by the concept of the jump frequency approach. Some of these considerations are enumerated in what follows.

As the work presented here has revealed, diffusion is a continuous process involving flows of atoms with the *simultaneous adjustment of the lattice* to accommodate any imbalances in these flows in and out of a given volume

element. Thus, the measurements made in the laboratory frame, namely the concentrations along the diffusion direction, tell only the combined story. The fluxes derived from such measurements, which are the interdiffusion fluxes, have, built into them, terms involving not only the intrinsic atom fluxes but also this lattice motion. Separating these two effects by making measurements of the lattice motion by the placement of inert Kirkendall markers is strongly recommended for the purpose of obtaining a better handle on the process. One possible experimental program to achieve this would be as follows.

One alloy system that is well studied and is known to be amenable to analytical techniques in materials science is the copper-silver-gold system. This system is isomorphous on the Au-Ag binary, isomorphous with two order-disorder reactions on the Au-Cu binary, and a simple eutectic on the Ag-Cu binary. By suitably choosing the end-point compositions, a number of interesting aspects of diffusion, both in isomorphous and in two-phase situations can be explored. The key to the experimental design would be the placement of inert markers at regular intervals along the diffusion direction, whose positions before and after the diffusion anneal would track the lattice motion. Perhaps this could be achieved by either forging together thin foils of these metals (well known for their malleability) or by electroplating successive layers, with markers of a suitable inert material placed in

between them. Two other possibilities that have potential in this regard are (a) the use of micro-hardness indentations on a polished surface parallel to the diffusion direction, and (b) microscopic perforations made by laser at suitably selected intervals along the diffusion direction, in the diffusion zone.

The diffusion data obtained in the above experimental design would consist of the microprobe data on the concentration profiles, augmented by the lattice shift data from the marker measurements. Application of the jump frequency approach to these data will, hopefully, establish the viability of this theory and lead to a better understanding of diffusion processes in substitutional solid solutions.

Throughout this work, the focus has been on tackling the problem of diffusion in semi-infinite couples. However, in principle, there should be no problem adapting the JFA to situations where the boundary conditions and the geometry are different, as for example, in surface phenomena like oxidation, carburizing etc. or in the growth, dissolution or coarsening of second phase particles etc.

It should also be possible to organize the computer programs presented in this work in a form that is suitable for interactive sessions, where the student/researcher merely responds to prompts from the computer regarding input and the computer's output, i.e., the penetration and the lattice shift

profiles, are presented as graphs. Such a software package, apart from aiding in diffusion research, would also serve as a valuable education tool for courses on diffusion.

Ideally, the computer simulation package should be developed to a point where, given the experimental profiles and a first guess on the kinetic parameters, the computer automatically adjusts these parameters and iteratively arrives at a set of jump frequencies (with their compositional dependence) that constitute a "best fit" for the data.

With the increased use of line compounds and intermetallics for high temperature applications in the industry, an understanding of the diffusion behavior at these operating temperatures becomes an imperative, so that potential problems in materials design can be identified and avoided *ab initio*, without the need for learning from experiences in applications-related failures. The JFA provides the industry with a valuable weapon in this regard.

All of the computer simulations presented in this work were based on certain assumptions regarding the input parameters. In particular, the material variables, namely the molar volume and the interatomic distance were assumed to be 'typical' and constant, as mentioned in chapter 6. It would be interesting and instructive to relax these restrictive assumptions and study, for example cases of diffusion where the molar volume is concentration dependent. In addition, the programs restricted themselves to a range of jump frequencies

that were compatible with the design inputs, such as the thickness of the slices, the time increment for each iteration etc. If a real system calls for these jump frequencies to be in a different regime, then obviously one has to modify these inputs accordingly. It must, however be emphasized that *none of these assumptions, be they material properties or experimental design parameters are pivotal to the JFA*. Thus, in future, with minimum effort, these programs can be modified and tailored to any situation that requires experimental scrutiny.

On one final note, the application of JFA to experimental studies in diffusion is analogous to the solving of trigonometric identities. Both the left hand side of the equation, which in this case would be the JFA model, and the right hand side, which would be the appropriate experimental result are worked toward each other until the desired degree of consonance is achieved. Thus, the JfA is not antecedent to experimental design but concurrent with it. What this means is that in a successful application of the JFA, preliminary experiments are designed with a view to producing a tentative model for diffusion, and based on the insight so gained, additional experiments follow and the model is further refined.

APPENDIX
COMPUTER SIMULATION PROGRAMS FOR DIFFUSION USING THE JFA

{NOTE: The programs presented in this appendix serve as typical examples of the several dozen programs that were used to generate the output presented in this study. In particular, a number of modifications were made to programs # 3, 4, 5 & 6 to cater to the specific situations that were being simulated. These modifications are primarily in the I/O (READ/WRITE) area and do not affect the main body of the program}

1. Tracer Diffusion

```
program TRACER;
```

```
{this program simulates the redistribution of a layer of  
tracer atoms that is wedged between two slabs of normal metal  
after an isothermal diffusion anneal}
```

```
const components =2; slices1 =100; slices2 =102; slices3 =202;  
spacing = 2; molarVolume = 2.7e-11; jumpDist = 3e-4  
timeIncrement = 10;
```

```
type precision = real; columns = 1..400; rows = 1..3;  
colArray = array[columns] of precision;  
rowArray = array[rows] of precision;  
allArray = array[rows,columns] of precision;
```

```
var counter, counterLimit :integer;  
jumpFreq :precision;  
xi, xinit, sliceWidth :colArray;  
alloy1, alloy2, alloy3 :rowArray;  
concnK, fluxK, meanConcnK :allArray;  
changeNumAtms, oldNumAtms :allArray;  
i :columns; k :rows;
```

```
BEGIN {start reading input values and initialize the program}  
counter :=1; readLn (counterLimit); jumpFreq :=1e6;  
alloy1[1] :=1; alloy1[2] :=0; alloy2[1] :=0;  
alloy2[2] :=1; alloy3[1] :=1; alloy3[2] :=0;
```

```

for i:=1 to slices3 + 1 do
  BEGIN
    xi[i]:=spacing*(i-1); xinit[i]:=xi[i];
    sliceWidth[i]:= spacing;
  END;
for k:= 1 to components do
  BEGIN
    for i:=1 to slices1 -1 do
      BEGIN
        concnK[k,i]:=alloy1[k]/molarVolume;
        meanConcnK[k,i]:=concnK[k,i];
      END;
    for i:=slices1 to slices2 -1 do
      BEGIN
        concnK[k,i]:=alloy2[k]/molarVolume;
        meanConcnK[k,i]:=concnK[k,i];
      END;
    for i:=slices2 to slices3 +1 do
      BEGIN
        concnK[k,i]:=alloy3[k]/molarVolume;
        meanConcnK[k,i]:=concnK[k,i];
      END;
    END; {finish reading input values and initializing}
    {main iterative computational action starts here}
    while counter <= counterLimit do {main iterative loop}
      BEGIN {calculating fluxes}
        for k:= 1 to components do
          BEGIN
            fluxK[k,1]:=0;fluxK[k,slices3 +1]:=0;
            for i:=2 to slices3 do
              BEGIN
                fluxK[k,i] := (-1/6) * (sqr(jumpDist)*jumpFreq;
                fluxK[k,i] :=fluxK[k,i] *(concnK[k,i+1]-concnK[k,i-1]);
                fluxK[k,i] :=fluxK[k,i] /(xi[i+1]-xi[i-1]);
              END;
            END; {fluxes calculated}
          for k:= 1 to components do
            BEGIN {computes accumulations in each slice for each
              component}
              for i:=1 to slices3 do
                BEGIN
                  changeNumAtms[k,i] := (fluxK[k,i]-fluxK[k,i+1]) *
                                         timeIncrement;
                  oldNumAtms[k,i] :=meanConcnK[k,i]*sliceWidth[i];
                END;
              END; {accumulations calculated}
            for i:=1 to slices3 do
              BEGIN {computes new slice widths}
                for k:=1 to components do
                  sliceWidth[i] :=sliceWidth[i]+changeNumAtms[k,i]*
                                molarVolume;
                END; {new slice widths calculated}
              END;
            END;
          END;
        END;
      END;
    END;
  END;
END;

```

```

for i:=1 to slices3 do {evaluates new xi values}
  xi[i+1]:=xi[i]+sliceWidth[i]; {new xi's evaluated}
for i:=1 to slices3 do {computes new mean concentrations}
  for k:=1 to components do
    meanConcnK[k,i] := (oldNumAtms[k,i] +
      changeNumAtms[k,i])/sliceWidth;
  {new mean concentrations computed}
for k:=1 to components do {calculates new concentrations}
  i:=3;
  while i < slices3 +1 do
    BEGIN
      concnK[k,i] := meanConcnK[k,i] - meanConcnK[k,i-1];
      concnK[k,i] := concnK[k,i] / (1+sliceWidth[i] /
        sliceWidth[i-1]);
      concnK[k,i] := meanConcnK[k,i] - concnK[k,i];
    END; {new concentrations calculated}
  if counter = counterLimit then {start printout statements}
    BEGIN
      for i:=1 to slices3+1 do
        BEGIN
          write (i :8); write (xinit[i] :15:2);
          write (concnK[2,i] :16:4); writeLn;
          END; {end of printout statements}
        counter:=counter +1;
      END;
    END. {end of program}

```

2. Binary Isomorphous Diffusion

```

program KIRKENDALL;
{this program is designed to simulate diffusion in a binary
couple between pure A and pure B, with A atoms jumping an
order of magnitude more frequently than B atoms}

label 1,2;

const components =2; slices =120; spacing =2; counterLimit =1024;
  molarVolume =2.7e-11; jumpDist =3e-4; timeIncrement = 10;

type precision = real; columns = 1..400; rows = 1..3;
  colArray = array[columns] of precision;
  rowArray = array[rows] of precision;
  allArray = array[rows,columns] of precision;

var counter :integer;
  xi,xinit,sliceWidth :colArray;
  alloy1,alloy2,jumpFreqK :rowArray;
  concnK,fluxK,meanConcnK :allArray;
  changeNumAtms,oldNumAtms :allArray;
  i :columns; k :rows;

```

```

BEGIN {start reading input values and initialize the program}
counter :=1;alloy1[1]:=1;alloy1[2]:=0;
alloy2[1]:=0;alloy2[2]:=1;
for k:=1 to components do
  readLn (jumpFreqK[k]);
for i:=1 to 2*slices + 1 do
  BEGIN
    xi[i]:=spacing*(i-1); xinit[i]:=xi[i];
    sliceWidth[i] := spacing;
  END;
for k:= 1 to components do
  BEGIN
    for i:=1 to slices do
      BEGIN
        concnK[k,i]:=alloy1[k]/molarVolume;
        meanConcnK[k,i]:=concnK[k,i];
      END;
    for i:=slices +1 to 2*slices +1 do
      BEGIN
        concnK[k,i]:=alloy2[k]/molarVolume;
        meanConcnK[k,i]:=concnK[k,i];
      END;
    END; {finish reading input values and initializing}
{main iterative computational action starts here}
while counter <= counterLimit do {main loop for time
iteration}
  BEGIN {calculating fluxes}
  for k:= 1 to components do
    BEGIN
      fluxK[k,1]:=0;fluxK[k,2*slices +1]:=0;
      for i:=2 to 2*slices do
        BEGIN
          fluxK[k,i] := (-1/6)*(sqr(jumpDist)*jumpFreqK[k];
          fluxK[k,i] :=fluxK[k,i]*(concnK[k,i+1]-concnK[k,i-1]);
          fluxK[k,i] :=fluxK[k,i]/(xi[i+1]-xi[i-1]);
        END;
      END; {fluxes calculated}
    for k:= 1 to components do
      BEGIN {computes accumulations in each slice for each
component}
        for i:=1 to 2*slices do
          BEGIN
            changeNumAtms[k,i] :=(fluxK[k,i]-
                                fluxK[k,i+1])*timeIncrement;
            oldNumAtms[k,i] :=meanConcnK[k,i]*sliceWidth[i];
          END;
        END; {accumulations calculated}
      
```

```

for i:=1 to 2*slices do
  BEGIN {computes new slice widths}
    for k:=1 to components do
      sliceWidth[i]:=sliceWidth[i]+
        changeNumAtms[k,i]*molarVolume;
    END; {new slice widths calculated}
  for i:=1 to 2*slices do {evaluates new xi values}
    xi[i+1]:=xi[i]+sliceWidth[i]; {new xi's evaluated}
  for i:=1 to slices3 do {computes new mean concentrations}
    for k:=1 to components do
      meanConcnK[k,i] := (oldNumAtms[k,i] +
        changeNumAtms[k,i])/sliceWidth;
    {new mean concentrations computed}
  for k:=1 to components do {calculates new concentrations}
    i:=2;
    while i < 2*slices +1 do
      BEGIN
        concnK[k,i] := meanConcnK[k,i] - meanConcnK[k,i-1];
        concnK[k,i] := concnK[k,i]/(1+
          sliceWidth[i]/sliceWidth[i-1]);
        concnK[k,i] := meanConcnK[k,i] - concnK[k,i];
      END; {new concentrations calculated}
    if counter > counterLimit then goto 2;
  else {start printout statements}
    BEGIN
      case counter of
        8 goto 1; 16 goto 1; 32 goto 1; 64 goto 1; 128 goto 1;
        256 goto 1; 512 goto 1; 1024 goto 1;
      END;
      goto 2;
    1: BEGIN
      for i:=1 to 2*slices do
        BEGIN
          write (xi[i]-xinit[i] :8:3); write (xi :8:3);
          write ((xi[i]-xinit[i])/
            sqrt(counter*timeIncrement) :8:3);
          write (xi/sqrt(counter*timeIncrement) :8:3);
          write (concnK[2,i] :16:4); writeLn;
        END; {end of printout statements}
      counter:=counter +1;
    END;
  END. {end of program}

```

3. Isomorphous Diffusion With Constant Γ 's

program CI-GAMMA;

{this program is written for diffusion in ternary isomorphous systems with composition independent jump frequencies}

```
const components =3;slices =120;spacing =2;counterLimit =600;
    molarVolume =2.7e-11;jumpDist =3e-4;timeIncrement =10;
```

```
type precision = real;columns = 1..400;rows = 1..3;
    colArray = array[columns] of precision;
    rowArray = array[rows] of precision;
    allArray = array[rows,columns] of precision;
```

```
var counter :integer;
    xi,xinit,sliceWidth :colArray;
    alloy1,alloy2,jumpFreqK :rowArray;
    concnK,fluxK,meanConcnK :allArray;
    changeNumAtms,oldNumAtms :allArray;
    i :columns; k :rows;
```

```
BEGIN {start reading input values and initialize the program}
counter :=1;alloy1[1]:=1/3;alloy1[2]:=1/3;alloy1[3]:=1/3;
```

```
for k:=1 to components do
```

```
    BEGIN
```

```
        for i:=1 to slices do
```

```
            concnK[k,i]:=alloy1[k]/molarVolume;
```

```
            readLn (alloy2[k];
```

```
            for i:=slices+1 to 2*slices do
```

```
                concnK[k,i]:=alloy2[k]/molarVolume;
```

```
            END;
```

```
jumpfreqK[1]:=1e7;jumpFreqK[2]:=5e6;jumpFreqK[3]:=1e6;
```

```
for i:=1 to 2*slices + 1 do
```

```
    BEGIN
```

```
        xi[i]:=spacing*(i-1); xinit[i]:=xi[i];
```

```
        sliceWidth[i] := spacing;
```

```
    END;
```

```
for k:= 1 to components do
```

```
    BEGIN
```

```
        for i:=1 to slices do
```

```
            BEGIN
```

```
                concnK[k,i]:=alloy1[k]/molarVolume;
```

```
                meanConcnK[k,i]:=concnK[k,i];
```

```
            END;
```

```
        for i:=slices +1 to 2*slices +1 do
```

```
            BEGIN
```

```
                concnK[k,i]:=alloy2[k]/molarVolume;
```

```
                meanConcnK[k,i]:=concnK[k,i];
```

```
            END;
```

```
    END; {finish reading input values and initializing}
```

```

{main iterative computational action starts here}
while counter <= counterLimit do {main loop for time
iteration}
BEGIN {calculating fluxes}
for k:= 1 to components do
  BEGIN
    fluxK[k,1]:=0;fluxK[k,2*slices +1]:=0;
    for i:=2 to 2*slices do
      BEGIN
        fluxK[k,i] := (-1/6) * (sqr(jumpDist)*jumpFreqK[k];
        fluxK[k,i] := fluxK[k,i] * (concnK[k,i+1] - concnK[k,i-1]);
        fluxK[k,i] := fluxK[k,i] / (xi[i+1] - xi[i-1]);
      END;
    END; {fluxes calculated}
  for k:= 1 to components do
    BEGIN {computes accumulations in each slice for each
      component}
      for i:=1 to 2*slices do
        BEGIN
          changeNumAtms[k,i] := (fluxK[k,i] -
                                fluxK[k,i+1]*timeIncrement;
          oldNumAtms[k,i] := meanConcnK[k,i]*sliceWidth[i];
        END;
      END; {accumulations calculated}
    for i:=1 to 2*slices do
      BEGIN {computes new slice widths}
        for k:=1 to components do
          sliceWidth[i] := sliceWidth[i] +
            changeNumAtms[k,i]*molarVolume;
        END; {new slice widths calculated}
      for i:=1 to 2*slices do {evaluates new xi values}
        xi[i+1] := xi[i] + sliceWidth[i]; {new xi's evaluated}
      for i:=1 to slices3 do {computes new mean concentrations}
        for k:=1 to components do
          meanConcnK[k,i] := (oldNumAtms[k,i] +
                              changeNumAtms[k,i])/sliceWidth;
        {new mean concentrations computed}
      for k:=1 to components do {calculates new concentrations}
        i:=2;
        while i < 2*slices +1 do
          BEGIN
            concnK[k,i] := meanConcnK[k,i] - meanConcnK[k,i-1];
            concnK[k,i] := concnK[k,i] /
              (1+sliceWidth[i]/sliceWidth[i-1]);
            concnK[k,i] := meanConcnK[k,i] - concnK[k,i];
          END; {new concentrations calculated}
        end while
      end for
    end for
  end for
end while

```

```

if counter = counterLimit then
  BEGIN
    for i:=1 to 2*slices do
      BEGIN
        write (xi[i]-xinit[i] :8:3);write (xi :8:3);
        write ((xi[i]-xinit[i])/
          sqrt(counter*timeIncrement) :8:3);
        write (xi/sqrt(counter*timeIncrement) :8:3);
        for k:=1 to components do
          write (100*concnK[k,i]*molarVolume :8:2);
          write ((concnK[2,i] +0.5*concnK[3,i])*molarVolume :8:4);
          writeLn (0.866*concnK[3,i]*molarVolume :8:4);
        END; {end of printout statements}
      counter:=counter +1;
    END;
  END. {end of program}

```

4. Isomorphous Diffusion With Composition Dependent D 's

program CD-GAMMA;

{this program is written for diffusion in ternary isomorphous systems with jump frequencies that vary with composition}

```

const components =3;slices =120;spacing =2;counterLimit =1000;
  molarVolume =2.7e-11;jumpDist =3e-4;timeIncrement =10;

```

```

type precision =real;columns =1..250;rows =1..5;cubic =1..15;
  colArray = array[columns] of precision;
  rowArray = array[rows] of precision;
  allArray = array[rows,columns] of precision;
  coefArray = array[rows,cubic] of precision;

```

```

var   counter :integer;coef : coefArray
      xi,xinit,sliceWidth :colArray;
      alloy1,alloy2 :rowArray;i :columns;k :rows;
      concnK,fluxK,meanConcnK,jumpfreqK :allArray;
      changeNumAtms,oldNumAtms :allArray;

```

BEGIN {start reading input values and initialize the program}

```

counter :=1;alloy1[1]:=1/3;alloy1[2]:=1/3;alloy1[3]:=1/3;
for k:=1 to components do

```

```

  BEGIN
    for i:=1 to slices do
      concnK[k,i]:=alloy1[k]/molarVolume;
      readLn (alloy2[k]);
      for i:=slices+1 to 2*slices +1 do
        concnK[k,i]:=alloy2[k]/molarVolume;
      END;

```

```

coefK[1,1]:=100;coefK[1,2]:=-50;
coefK[1,3]:=-90;coefK[2,1]:= 50;
coefK[2,2]:=-25;coefK[2,3]:=-45;
coefK[3,1]:= 10;coefK[3,2]:= -5;coefK[3,3]:= -9;
for i:=1 to 2*slices + 1 do
  BEGIN
    xi[i]:=spacing*((i-1)-slices);xinit[i]:=xi[i];
    sliceWidth[i]:= spacing;
    for k:=1 to components do
      meanConcnK[k,i]:=0.5*(concnK[k,i]+concnK[k,i+1]);
    END; {finish reading input values and initializing}
  {main iterative computational action starts here}
  while counter <= counterLimit do
    BEGIN {main loop for time iteration}
      for k:= 1 to components do
        BEGIN {calculating fluxes}
          fluxK[k,1]:=0;fluxK[k,2*slices +1]:=0;
          for i:=1 to 2*slices +1 do
            BEGIN {calculates concentration dependent jump
              frequencies}
              jumpFreqK[k,i]:=coefK[k,i]+
                coefK[k,2]*concnK[2,i]*molarVolume;
              jumpFreqK[k,i]:=jumpFreqK[k,i]+
                coefK[k,3]*concnK[3,i]*molarVolume;
            END; {jump frequencies calculated}
          for i:=2 to 2*slices do
            BEGIN
              fluxK[k,i]:=(concnK[k,i+1]*jumpFreqK[k,i]) -
                (concnK[k,i-1]*jumpFreqK[k,i-1]);
              fluxK[k,i]:=fluxK[k,i]/(xi[i+1]-xi[i-1]);
              fluxK[k,i]:=fluxK[k,i]*(-1/6)*1e5*sqr(jumpDist);
            END;
          END; {fluxes calculated}
          for k:= 1 to components do
            BEGIN {computes accumulations in each slice for each
              component}
              for i:=1 to 2*slices do {accumulations by slice}
                BEGIN
                  changeNumAtms[k,i]:=fluxK[k,i] -
                    fluxK[k,i+1]*timeIncrement;
                  oldNumAtms[k,i]:=meanConcnK[k,i]*sliceWidth[i];
                END;
              END; {accumulations calculated}
            for i:=2 to 2*slices do
              BEGIN {computes new slice widths and new xi values}
                for k:=1 to components do
                  sliceWidth[i]:=sliceWidth[i]+
                    changeNumAtms[k,i]*molarVolume;
                xi[i]:=xi[i-1]+sliceWidth[i]
              END; {new slice widths and xi values calculated}
            END;
          END;
        END;
      END;
    END;
  END;

```

```

for i:=2 to 2*slices do {computes new concentrations}
  BEGIN
    for k:=1 to components do
      BEGIN
        meanConcnK[k,i] := (oldNumAtms[k,i]+changeNumAtms[k,i])/
                           sliceWidth[i];
        concnK[k,i] := (meanConcnK[k,i]-meanConcnK[k,i-1]);
        concnK[k,i] := concnK[k,i]/
                       (1+sliceWidth[i]/slcieWidth[i-1]);
        concnK[k,i] := meanConcnK[k,i]-concnK[k,i];
      END; {new concentrations computed}
    END;
  if counter = counterLimit then
    BEGIN
      for i:=2 to 2*slices do
        BEGIN
          write (xi[i]-xinit[i] :8:3);write (xi :8:3);
          write ((xi[i]-xinit[i])/
                sqrt(counter*timeIncrement) :8:3);
          write (xi/sqrt(counter*timeIncrement) :8:3);
          for k:=1 to components do
            write (100*concnK[k,i]*molarVolume :8:2);
            write ((concnK[2,i]+0.5*concnK[3,i])*molarVolume :8:4);
            writeLn (0.866*concnK[3,i]*molarVolume :8:4);
          END; {end of printout statements}
          counter:=counter +1;
        END;
      END. {end of program}

```

5. Planar Phase Boundary Migration in Two-phase Systems

program TWO-PHASE;

{this program simulates the migration of a planar interphase interface in binary two-phase systems, with the end-pint compositions of the semi-infinite diffusion couple in the terminal one-phase fields}

```

const components =2;slices =100;spacing =2;counterLimit =600;
    molarVolume =2.7e-11;jumpDist =3e-4;timeIncrement =10;

```

```

type precision =real;columns =1..250;rows =1..5;cubic =1..15;
    colArray = array[columns] of precision;
    rowArray = array[rows] of precision;
    allArray = array[rows,columns] of precision;
    coefArray = array[rows,cubic] of precision;
    iter = 1..600;timeArray = array[iter] of precision;

```

```

var   counter,istar :integer; coef :coefArray;
      interphase,inter,lambda :precision;
      xi,xinit,sliceWidth :colArray; i :columns; k :rows;
      concnK,fluxK,meanConcnK :allArray;
      changeNumAtms,oldNumAtms :allArray;
      alloy1,alloy2,alphaK,betaK :rowArray;
      fluxAlphaK,fluxBetaK :rowArray;
      slopeAlphaK,slopeBetaK :rowarray;
      jumpFreqAlphaK,jumpFreqBetaK :rowArray;
      time,shift,relshift :timeArray;

BEGIN {start reading input values and initialize the program}
alphaK[1]:=0.95;alphaK[2]:=0.05;betaK[1]:=0.85;betaK[2]:=0.15;
alloy1[1]:=1;alloy1[2]:=0;
alloy2[1]:=0;alloy2[2]:=1;counter :=1;
for k:=1 to components do
  BEGIN
    readLn (jumpFreqAlphaK[k] );readLn (jumpFreqBetaK[k] );
    jumpFreqAlphaK[k]:=jumpFreqAlphaK[k]*1e6;
    jumpFreqBetaK[k]:=jumpFreqBetaK[k]*1e6;
  END;
lambda:=((alloy1[2]+alloy2[2])-(alphaK[2]+betaK[2])*spacing;
lambda:=lambda/((alloy1[2]-alloy2[2])+(alphaK[2]-betaK[2]));
interphase :=lambda;
if lambda >=0 then  istar:=slices+1;if lambda <0 then
istar:=slices;
for k:=1 to components do
  BEGIN
    for i:=1 to istar-2 do
      BEGIN
        concnK[k,i]:=alloy1[k]/molarVolume;
        meanconcnK[k,i]:=concnK[k,i];
      END;
    for i:=istar+2 to 2*slices+1 do
      BEGIN
        concnK[k,i]:=alloy2[k]/molarVolume;
        meanconcnK[k,i]:=concnK[k,i];
      END;
    if lambda > 0 then
      BEGIN
        concnK[k,istar-1]:=alloy1[k]/molarVolume;
        concnK[k,istar]:=(alloy1[k]*lambda)+(alphaK[k]*spacing);
        concnK[k,istar]:=concnK[k,istar]/
          (molarVolume*(spacing+lambda));
        concnK[k,istar+1]:=alloy2[k]/molarVolume;
        meanConcnK[k,istar-1]:=0.5*(concnK
          [k,istar-1]+concnK[k,istar]);
        meanConcnK[k,istar+1]:=concnK[k,istar+1];
      END;

```

```

else if lambda < 0 then
  BEGIN
    concnK[k,istar-1]:=alloy1[k]/molarVolume;
    concnK[k,istar]:=alloy1[k]/molarVolume;
    concnK[k,istar+1]:=(betaK[k]*spacing)-(alloy2[k]*lambda);
    concnK[k,istar+1]:=concnK[k,istar+1]/
      (molarVolume*(spacing-lambda));
    meanConcnK[k,istar-1]:=concnK[k,istar-1];
    meanConcnK[k,istar+1]:=0.5*(concnK[k,istar+1]+
      concnK[k,istar+2]);
  else
    BEGIN
      concnK[k,istar-1]:=alloy1[k]/molarVolume;
      concnK[k,istar]:=betaK[k]/molarVolume;
      concnK[k,istar+1]:=alloy2[k]/molarVolume;
      meanConcnK[k,istar-1]:=0.5*(concnK[k,istar-1]+
        alphaK[k]/molarVolume);
      meanConcnK[k,istar+1]:=0.5*(concnK[k,istar+1]+
        concnK[k,istar+2]);
    END;
  for i:=1 to 2*slices+1 do
    BEGIN
      xi[i]:=spacing*((i-1)*slices);
      xinit[i]:=xi[i];sliceWidth:=spacing;
      END; {finish reading input values and initializing}
    {main iterative computational action starts here}
    while counter <= counterLimit do
      BEGIN {main loop for time iteration}
        for k:= 1 to components do
          BEGIN {calculating fluxes}
            meanConcnK[k,istar]:=(concnK[k,istar]+
              alphaK[k]/molarVolume)*
              (interphase-xi[istar]);
            meanConcnK[k,istar]:=meanConcnK[k,istar]+
              (concnK[k,istar+1]+
                betaK[k]/molarVolume)*
                (xi[istar+1]-interphase);
            meanConcnK[k,istar]:=meanConcnK[k,istar]/
              (2*(xi[istar+1]-xi[istar]));
            fluxK[k,1]:=0;fluxK[k,2*slices+1]:=0;
            for i:=2 to istar-1 do
              BEGIN {computing fluxes in the alpha phase}
                fluxK[k,i]:=(-1/6)*jumpFreqAlphaK[k]*sqr(jumpDist);
                fluxK[k,i]:=fluxK[k,i]*(concnK[k,i+1]-(concnK[k,i-1]));
                fluxK[k,i]:=fluxK[k,i]/(xi[i+1]-xi[i-1]);
              END; {alpha phase fluxes computed}
              fluxK[k,istar]:=(-1/6)*jumpFreqAlphaK[k]*sqr(jumpDist);
              fluxK[k,istar]:=fluxK[k,istar]*((alphaK[k]/molarVolume)-
                concnK[k,istar-1]);
              fluxK[k,istar]:=fluxK[k,istar]/(interphase-xi[istar-1]);
            end

```

```

fluxK[k,istar+1] := (-1/6) * jumpFreqBetaK[k] * sqr(jumpDist);
fluxK[k,istar+1] := fluxK[k,istar+1] * (concnK[k,istar+2] -
    betaK/molarVolume);
fluxK[k,istar+1] := fluxK[k,istar+1] /
    ([xi[istar+2] - interphase]);
for i:=istar+2 to 2*slices do
    BEGIN {computing fluxes in the beta phase}
        fluxK[k,i] := (-1/6) * jumpFreqBetaK[k] * sqr(jumpDist);
        fluxK[k,i] := fluxK[k,i] * (concnK[k,i+1] - (concnK[k,i-1]));
        fluxK[k,i] := fluxK[k,i] / (xi[i+1] - xi[i-1]);
        END; {beta phase fluxes computed}
slopeAlphaK[k] := (fluxK[k,istar] - fluxK[k,istar-1]) /
    sliceWidth[istar-1];
fluxAlphaK := fluxK[k,istar] + slopeAlphaK[k] *
    (interphase - xi[istar]);
slopeBetaK[k] := (fluxK[k,istar+2] - fluxK[k,istar+1]) /
    sliceWidth[istar+1];
fluxBetaK[k] := fluxK[k,istar+1] - slopeBetaK[k] *
    (xi[istar+1] - interphase);
    END; {fluxes calculated}
inter := (betaK[2] * fluxBetaK[1]) - (betaK[1] * fluxBetaK[2]);
    inter := inter + (alphaK[1] * fluxAlphaK[2]) -
(alphaK[2] * fluxAlphaK[1]);
inter := inter * timeIncrement * molarVolume / (betaK[1] - alphaK[1]);
interphase := interphase + inter;
if interphase <= xi[istar] then istar := istar-1;
else if interphase >= xi[istar+1] then istar := istar+1;
else if interphase < xi[istar+1] then istar := istar;
shift[counter] := interphase;
time[counter] := counter * timeIncrement;
for k:= 1 to components do
    BEGIN {computes accumulations in each slice for each
        component}
        for i:=1 to 2*slices do
            BEGIN
                changeNumAtms[k,i] := (fluxK[k,i] -
                    fluxK[k,i+1]) * timeIncrement;
                oldNumAtms[k,i] := meanConcnK[k,i] * sliceWidth[i];
            END;
        END; {accumulations calculated}
    for i:=2 to 2*slices do
        BEGIN {computes new slice widths and new xi values}
            for k:=1 to components do
                sliceWidth[i] := sliceWidth[i] +
                    changeNumAtms[k,i] * molarVolume;
                xi[i] := xi[i-1] + sliceWidth[i]
            END; {new slice widths and xi values calculated}
        for k:=1 to components do
            BEGIN {computes new concentrations}
                i:=2;

```



```

while i < 2*slices+1 do
  BEGIN
    meanConcnK[k,i] := (oldNumAtms[k,i] + changeNumAtms[k,i]) /
      sliceWidth[i];
    concnK[k,i] := (meanConcnK[k,i] - meanConcnK[k,i-1]);
    concnK[k,i] := concnK[k,i] /
      (1 + sliceWidth[i] / sliceWidth[i-1]);
    concnK[k,i] := meanConcnK[k,i] - concnK[k,i];
  END;
  concnK[k,istar] := meanConcn[k,istar-1] -
    meanConcnK[k,istar-2];
  concnK[k,istar] := concnK[k,istar] / (1 + sliceWidth[istar-1] /
    sliceWidth[istar-2]);
  concnK[k,istar] := meanConcnK[k,istar-1] + concnK[k,istar];
  concnK[k,istar+1] := meanConcnK[k,istar+2] -
    meanConcnK[k,istar+1];
  concnK[k,istar+1] := concnK[k,istar+1] / (1 +
    sliceWidth[istar+1] /
    sliceWidth[istar+2]);
  concnK[k,istar+1] := meanConcnK[k,istar+1] -
    concnK[k,istar+1];
  for i:=2 to 2*slices do
    meanConcnK[k,i] := 0.5 * (concnK[k,i] + concnK[k,i+1]);
  END; {new concentrations computed}
if counter = 1 or counter mod 10 = 0 then
  BEGIN
    write (counter); write (sqrt(time[counter]) :8:4);
    writeLn (shift[counter] :8:3);
  END;
if counter = counterLimit then
  BEGIN
    for i:=2 to 2*slices do
      BEGIN
        if i:=istar then
          BEGIN
            write (0.0 :11:2);
            write (interphase/sqrt(counter*timeIncrement) :8:3);
            for k:=1 to components do
              writeLn (100*alphaK[k] :8:2);
            write (0.0 :11:2);
            for k:=1 to components do
              writeLn (100*betaK[k] :8:2);
            END;
            write ((xi[i]-xinit[i]) /
              sqrt(counter*timeIncrement) :8:3);
            write (xi/sqrt(counter*timeIncrement) :8:3);
            for k:=1 to components do
              writeLn (100*concnK[k,i]*molarVolume :8:2);
            END; {end of printout statements}
          counter:=counter+1;
        END;
      END. {end of program}

```

6. Intermediate Phase Growth During Diffusion

program THIRD-PHASE;

{this program simulates the formation and growth of in an intermediate phase in a binary three-phase system during diffusion, with both end-points of the semi-infinite couple in the terminal one-phase fields}

```
const components =2; slices1 =119; slices2 =121; slices3: =240;
    spacing = 2; counterLimit = 600;
    molarVolume =2.7e-11; jumpDist =3e-4; timeIncrement = 10;
```

label 1,2;

```
type precision =real; columns =1..250; rows =1..5; cubic =1..15;
    colArray = array[columns] of precision;
    rowArray = array[rows] of precision;
    allArray = array[rows,columns] of precision;
    coefArray = array[rows,cubic] of precision;
    iter = 1..600; timeArray = array[iter] of precision;
```

```
var    counter, istar1, istar2 :integer; coef :coefArray;
    interim1, interim2, inter1 :precision;
    inter2, lambda1, lambda2 :precision;
    xi, xinit, sliceWidth :colArray; i :columns; k :rows;
    concnK, fluxK, meanConcnK :allArray
    changeNumAtms, oldNumAtms :allArray;
    alloy1, alloy2, alloy3, alphaK, betaK :rowArray;
    etaAlphaK, etaBetaK :rowarray;
    time, shift, relshift :timeArray;
    fluxAlphaK, fluxBetaK :rowArray;
    fluxEtaAlphaK, fluxEtaBetaK :rowArray;
    slopeAlphaK, slopeBetaK :rowArray;
    slopeEtaAlphaK, slopeEtaBetaK:rowarray;
    jumpFreqAlphaK, jumpFreqBetaK, jumpFreqEtaK :rowArray;
```

```
BEGIN {start reading input values and initialize the program}
    alphaK[1]:=0.8; alphaK[2]:=0.2;
    etaAlphaK[1]:=0.65; etaAlphaK[2]:=0.35;
    etaBetaK[1]:=0.45; etaBetaK[2]:=0.55;
    betaK[1]:=0.3; betaK[2]:=0.7
    betaK[1]:=0.85; betaK[2]:=0.15;
    alloy1[1]:=1; alloy1[2]:=0; alloy2[1]:=0.55; alloy2[2]:=0.45;
    alloy3[1]:=0.1; alloy3[2]:=0.9; counter :=1;
    jumpFreqAlphaK[1]:=5e5; jumpFreqAlphaK[2]:=1e6;
    jumpFreqEtaK[1]:=1e6; jumpFreqEtaK[2]:=5e6;
    jumpFreqBetaK[1]:=1e5; jumpFreqBetaK[2]:=1e6;
    istar1:=slices1; istar2:=slices2;
    inter1:=xi[istar1]+1; inter2:=xi[istar2]+1;
```

```

for k:=1 to components do
  BEGIN
    for i:=1 to istar1-2 do
      BEGIN
        concnK[k,i]:=alloy1[k]/molarVolume;
        meanconcnK[k,i]:=concnK[k,i];
      END;
    for i:=istar1+2 to istar2-2 do
      BEGIN
        concnK[k,i]:=alloy2[k]/molarVolume;
        meanconcnK[k,i]:=concnK[k,i];
      END;
    for i:=istar1+2+2 to slices3+1 do
      BEGIN
        concnK[k,i]:=alloy3[k]/molarVolume;
        meanconcnK[k,i]:=concnK[k,i];
      END;
    concnK[k,istar1-1]:=alloy1[k]/molarVolume;
    concnK[k,istar1]:=alloy1[k]/molarVolume;
    concnK[k,istar1+1]:=(etaAlphaK[k]*spacing)-
      (alloy2[k]*inter1);
    concnK[k,istar1+1]:=concnK[k,istar1+1]/
      (spacing-inter1)*molarVolume;
    meanConcnK[k,istar1-1]:=concnK[k,istar1-1];
    meanConcnK[k,istar1+1]:=0.5*(concnK[k,istar1+1]+
      concnK[k,istar1+2]);
    concnK[k,istar2-1]:=alloy2[k]/molarVolume;
    concnK[k,istar2]:=(alloy2[k]*inter2)+(etaBetaK[k]*spacing);
    concnK[k,istar2]:=concnK[k,istar2]/
      (spacing+inter2)*molarVolume;
    concnK[k,istar2+1]:=alloy3[k]/molarVolume;
    meanConcnK[k,istar2-1]:=0.5*(concnK[k,istar2-1]+
      concnK[k,istar2]);
    meanConcnK[k,istar2+1]:=concnK[k,istar2+1];
  for i:=1 to 2*slices+1 do
    BEGIN
      xi[i]:=spacing*((i-1)*slices);
      xinit[i]:=xi[i];sliceWidth:=spacing;
    END; {finish reading input values and initializing}
  {main iterative computational action starts here}
  while counter <= counterLimit do
    BEGIN {main loop for time iteration}
      for k:= 1 to components do
        BEGIN {calculating fluxes}
          meanConcnK[k,istar1]:=(concnK[k,istar1]+
            alphaK[k]/molarVolume)*
            (inter1-xi[istar1]);
          meanConcnK[k,istar1]:=meanConcnK[k,istar1]+
            (concnK[k,istar1+1]+
              etaAlphaK[k]/molarVolume)*
              (xi[istar1+1]-inter1);

```

```

meanConcnK[k,istar1]:=meanConcnK[k,istar1]/
    (2*(xi[istar1+1]-xi[istar1]));
meanConcnK[k,istar2]:= (concnK[k,istar2]+
    etaBetaK[k]/molarVolume)*
    (inter2-xi[istar2]);
meanConcnK[k,istar2]:=meanConcnK[k,istar2]+
    (concnK[k,istar2+1]+
    betaK[k]/molarVolume)*
    (xi[istar2+1]-inter2);
meanConcnK[k,istar2]:=meanConcnK[k,istar2]/
    (2*(xi[istar2+1]-xi[istar2]));
fluxK[k,1]:=0;fluxK[k,slices3 +1]:=0;
for i:=2 to istar1-1 do
    BEGIN {computing fluxes in the alpha phase}
        fluxK[k,i] := (-1/6)*jumpFreqAlphaK[k]*sqr(jumpDist);
        fluxK[k,i] := fluxK[k,i] * (concnK[k,i+1] - (concnK[k,i-1]));
        fluxK[k,i] := fluxK[k,i] / (xi[i+1]-xi[i-1]);
    END; {alpha phase fluxes computed}
fluxK[k,istar1] := (-1/6)*jumpFreqAlphaK[k]*sqr(jumpDist);
fluxK[k,istar1] := fluxK[k,istar1] * ((alphaK[k]/molarVolume) -
    concnK[k,istar1-1]);
fluxK[k,istar1] := fluxK[k,istar1] / (inter1-xi[istar1-1]);
fluxK[k,istar1+1] := (-1/6)*jumpFreqEtaK[k]*sqr(jumpDist);
fluxK[k,istar1+1] := fluxK[k,istar1+1] * (concnK[k,istar1+2] -
    etaAlphaK/molarVolume);
fluxK[k,istar1+1] := fluxK[k,istar1+1] /
    ((xi[istar1+2]-inter1);
for i:=istar1+2 to istar2-1 do
    BEGIN {computing fluxes in the eta phase}
        fluxK[k,i] := (-1/6)*jumpFreqEtaK[k]*sqr(jumpDist);
        fluxK[k,i] := fluxK[k,i] * (concnK[k,i+1] - (concnK[k,i-1]));
        fluxK[k,i] := fluxK[k,i] / (xi[i+1]-xi[i-1]);
    END; {eta phase fluxes computed}
fluxK[k,istar2] := (-1/6)*jumpFreqEtaK[k]*sqr(jumpDist);
fluxK[k,istar2] := fluxK[k,istar2] *
    ((etaBetaK[k]/molarVolume) -
    concnK[k,istar2-1]);
fluxK[k,istar2] := fluxK[k,istar2] / (inter2-xi[istar2-1]);
fluxK[k,istar2+1] := (-1/6)*jumpFreqBetaK[k]*sqr(jumpDist);
fluxK[k,istar2+1] := fluxK[k,istar2+1] * (concnK[k,istar2+2] -
    betaK/molarVolume);
fluxK[k,istar2+1] := fluxK[k,istar2+1] /
    ((xi[istar2+2]-inter2);
for i:=istar2+2 to slices3 do
    BEGIN {computing fluxes in the beta phase}
        fluxK[k,i] := (-1/6)*jumpFreqbetaK[k]*sqr(jumpDist);
        fluxK[k,i] := fluxK[k,i] * (concnK[k,i+1] - (concnK[k,i-1]));
        fluxK[k,i] := fluxK[k,i] / (xi[i+1]-xi[i-1]);
    END; {beta phase fluxes computed}
slopeAlphaK[k] := (fluxK[k,istar1] - fluxK[k,istar1-1]) /
    sliceWidth[istar1-1];

```

```

fluxAlphaK:=fluxK[k,istar1]+slopeAlphaK[k]*
    (inter1-xi[istar1]);
slopeEtaAlphaK[k]:=(fluxK[k,istar1+2]-
    fluxK[k,istar1+1])/
    sliceWidth[istar1+1];
fluxEtaAlphaK:=fluxK[k,istar1+1]+slopeAlphaK[k]*
    (inter1-xi[istar1]+1);
slopeEtaBetaK[k]:=(fluxK[k,istar2] - fluxK[k,istar2-1])/
    sliceWidth[istar2-1];
fluxEtaBetaK:=fluxK[k,istar2]+slopeEtaBetaK[k]*
    (inter2-xi[istar2]+1);
slopeBetaK[k]:=(fluxK[k,istar2+2] - fluxK[k,istar2+1]/
    sliceWidth[istar2+1];
fluxBetaK[k]:=fluxK[k,istar2+1]-slopeBetaK[k]*
    (xi[istar2+1]-inter2);
END; {fluxes calculated}
interim1:=(etaAlphaK[2]*fluxetaAlphaK[1])-
    (etaAlphaK[1]*fluxetaAlphaK[2]);
interim1:=interim1+(alphaK[1]*fluxAlphaK[2])-
    (alphaK[2]*fluxAlphaK[1]);
interim1:=interim1*timeIncrement*
    molarVolume/(etaAlphaK[1]-alphaK[1]);
inter1:=inter1 +interim1;
if inter1 <=xi[istar1] then istar1:=istar1-1;
else if inter1 >=xi[istar1+1] then istar1:=istar1+1;
else if inter1 < xi[istar1+1] then istar1:=istar1;
shift1[counter]:=inter1;
time[counter]:=counter*timeIncrement;
interim2:=(betaK[2]*fluxBetaK[1])-
    (betaK[1]*fluxBetaK[2]);
interim2:=interim2+(etaBetaK[1]*fluxEtaBetaK[2])-
    (etaBetaK[2]*fluxEtaBetaK[1]);
interim2:=interim2*timeIncrement*
    molarVolume/(betaK[1]-etaBetaK[1]);
inter2:=inter2 +interim2;
if inter2 <=xi[istar2] then istar2:=istar2-1;
else if inter2 >=xi[istar2+1] then istar2:=istar2+1;
else if inter2 < xi[istar2+1] then istar2:=istar2;
shift2[counter]:=inter2;
if inter2 < inter1 then go to 1;
for k:= 1 to components do
    BEGIN {computes accumulations in each slice for each
        component}
        for i:=1 to slices3 do
            BEGIN
                changeNumAtms[k,i]:=(fluxK[k,i]-
                    fluxK[k,i+1])*timeIncrement;
                oldNumAtms[k,i]:=meanConcnK[k,i]*sliceWidth[i];
            END;
        END; {accumulations calculated}

```

```

for i:=2 to slices3 do
  BEGIN {computes new slice widths and new xi values}
    for k:=1 to components do
      sliceWidth[i]:=sliceWidth[i]+
        changeNumAtms[k,i]*molarVolume;
    xi[i]:=xi[i-1]+sliceWidth[i]
  END; {new slice widths and xi values calculated}
for k:=1 to components do
  BEGIN {computes new concentrations}
    i:=2;
    while i < slices3+1 do
      BEGIN
        meanConcnK[k,i] := (oldNumAtms[k,i] + changeNumAtms[k,i]) /
          sliceWidth[i];
        concnK[k,i] := (meanConcnK[k,i] - meanConcnK[k,i-1]);
        concnK[k,i] := concnK[k,i] / (1+
          sliceWidth[i]/sliceWidth[i-1]);
        concnK[k,i] := meanConcnK[k,i] - concnK[k,i];
      END;
    concnK[k,istar1] := meanConcn[k,istar1-1] -
      meanConcnK[k,istar1-2];
    concnK[k,istar1] := concnK[k,istar1] / (1+
      sliceWidth[istar1-1]/
      sliceWidth[istar1-2]);
    concnK[k,istar1] := meanConcnK[k,istar1-1] + concnK[k,istar1];
    concnK[k,istar1+1] := meanConcnK[k,istar1+2] -
      meanConcnK[k,istar1+1];
    concnK[k,istar1+1] := concnK[k,istar1+1] / (1+
      sliceWidth[istar1+1]/
      sliceWidth[istar1+2]);
    concnK[k,istar1+1] := meanConcnK[k,istar1+1] -
      concnK[k,istar1+1];
    concnK[k,istar2] := meanConcn[k,istar2-1] -
      meanConcnK[k,istar2-2];
    concnK[k,istar2] := concnK[k,istar2] / (1+
      sliceWidth[istar2-1]/
      sliceWidth[istar2-2]);
    concnK[k,istar2] := meanConcnK[k,istar2-1] + concnK[k,istar2];
    concnK[k,istar2+1] := meanConcnK[k,istar2+2] -
      meanConcnK[k,istar2+1];
    concnK[k,istar2+1] := concnK[k,istar2+1] / (1+
      sliceWidth[istar2+1]/
      sliceWidth[istar2+2]);
    concnK[k,istar2+1] := meanConcnK[k,istar2+1] -
      concnK[k,istar2+1];

    for i:=2 to slices3 do
      meanConcnK[k,i] := 0.5*(concnK[k,i] + concnK[k,i+1]);
    END; {new concentrations computed}
  
```

```

if counter = 1 or counter mod 10 = 0 then
  BEGIN
    write (counter); write (sqrt(time[counter]) :8:4);
    write (shift1[counter] :8:3); write (shift2[counter] :8:3);
    writeLn (shift2[counter]-shift1[counter] :8:3);
  END;
if counter = counterLimit then
  BEGIN
    for i:=2 to 2*slices do
      BEGIN
        if i:=istar1 then
          BEGIN
            write (0.0 :11:2);
            write (inter1/sqrt(counter*timeIncrement) :8:3);
            for k:=1 to components do
              writeLn (100*alphaK[k] :8:2);
            write (0.0 :11:2);
            for k:=1 to components do
              writeln (100*etaAlphaK[k] :8:2);
            END;
          if i:=istar2 then
            BEGIN
              write (0.0 :11:2);
              write (inter2/sqrt(counter*timeIncrement) :8:3);
              for k:=1 to components do
                writeLn (100*etaBetaK[k] :8:2);
              write (0.0 :11:2);
              for k:=1 to components do
                writeln (100*betaK[k] :8:2);
              END;
            write ((xi[i]-xinit[i])/
              sqrt(counter*timeIncrement) :8:3);
            write (xi/sqrt(counter*timeIncrement) :8:3);
            for k:=1 to components do
              writeLn (100*concnK[k,i]*molarVolume :8:2);
            END; {end of printout statements}
            counter:=counter +1;
          END;
        END. {end of program}

```

REFERENCES

1. A.E. Fick, *Pogg. Ann.*, **94**, 59 (1855).
2. L. Boltzman, *Ann. Phys. Leipzig*, **53**, 959 (1894).
3. C. Matano, *Japan Journal of Physics*, **8**, 109 (1933).
4. R.T. DeHoff, K.J. Anusavice and C.C. Wan, *Metallurgical Transactions*, **5**, 1113, (1974).
5. C.C. Wan and R.T. Dehoff, *Acta Metallurgica*, **25**, 287 (1977).
6. A. Vignes and J.P. Sabatier, *Trans. AIME*, **245**, 1795, (1969).
7. T.O. Ziebold and R.E. Ogilvie, *Trans. AIME*, **239**, 942 (1967).
8. C.C. Wan, *Doctoral Dissertation*, University of Florida, Gainesville Fl. (1973).
9. J.B. Fourier, *Theorie Analytique de la Chaleur*, cf Dover Pub., New York (1822).
10. J.B. Fourier, *The Analytical Theory of Heat*, Dover Pub., New York (1955).
11. Haase R., *Thermodynamics of Irreversible Processes*, Dover pub., New York, 217 (1990).
12. P.G. Shewmon, *Diffusion in Solids*, J. Williams Book Co., Jenks, OK, 6 (1983).
13. J.Jost, *Diffusion in Solids, Liquids, Gases*, Acad. Pr. Orlando, FL (1952).
14. J. Crank, *Mathematics of Diffusion*, Oxford Univ. Pr. Cary, NC (1956).
15. P.G. Shewmon, *Diffusion in Solids*, McGraw Hill Pr., Hightstown, NJ (1963).
16. J.S. Kirkaldy and D.J. Young, *Diffusion in the Condensed State*, The Institute of Metals, London (1987).

17. A.C. Smigelskas and E.O. Kirkendall, *Trans. AIME*, **171**, 130 (1947).
18. L.C. Correa Da Silva and R. Mehl, *Trans. AIME*, **191**, 155 (1951).
19. L.S. Darken, *Trans. AIME*, **175**, 184 (1948).
20. R.W. Baluffi, *Acta Metallurgica*, **8**, 871 (1961).
21. T.O. Ziebold, *Doctoral Dissertation*, MIT, Cambridge, Mass. (1965).
22. K.J. Anusavice, *Doctoral Dissertation*, University of Florida, Gainesville Fl. (1970).
23. Assuncao F.R., *Doctoral Dissertation*, University of Florida, Gainesville Fl. (1978).
24. L.S. Darken, *Trans. AIME*, **180**, 430 (1949).
25. F.N. Rhines, R.A. Meussner and R.T. DeHoff, *Trans AIME*, **212**, 860 (1958).
26. F.N. Rhines and J.B. Clark, *Trans. AIME*, **51**, 119 (1959).
27. J.S. Kirkaldy and L.C. Brown, *Canadian Metallurgical Quarterly*, **2**, 89 (1963).
28. J.S. Kirkaldy and D.G. Fedak, *Trans. AIME*, **224**, 490 (1962).
29. J.S. Kirkaldy, *Canadian Journal of Physics*, **35**, 435 (1957).
30. J.S. Kirkaldy, *Canadian Journal of Physics*, **36**, 899 (1958).
31. J.S. Kirkaldy, *Canadian Journal of Physics*, **36**, 917 (1958).
32. J.S. Kirkaldy, *Canadian Journal of Physics*, **37**, 30 (1959).
33. D.E. Coates, *Doctoral Dissertation*, McMaster University, Hamilton, Ontario (1970).
34. D.E. Coates, *Metallurgical Transactions*, **3**, 1203 (1972).
35. R.T. DeHoff, *Unpublished Research*, (1993).
36. R.D. Sisson Jr. and M.A. Dayananda, *Metallurgical Transactions*, **8A**, 1949 (1977).

37. M.A. Dayananda and R.E. Grace, *Trans. AIME*, **233**, 1287 (1965).
38. T.D. Moyer and M.A. Dayananda, *Metallurgical Transactions*, **7A**, 1035 (1976).
39. J. Philibert and A.G. Guy, *Compte Rendu*, **259**, 2281 (1963).
40. A.G. Guy and J. Philibert, *Zeitschrift Metallkunde*, **56**, 841 (1965).
41. T.O. Ziebold and A.R. Cooper, *Acta Metallurgica*, **13**, 465 (1965).
42. H. Schonert, *Z. Phys. Chem.*, **119**, 53 (1980).
43. M.A. Dayananda, P.F. Kirsch and R.E. Grace, *Trans. TMS-AIME*, **242**, 855 (1968).
44. P.T. Carlson, M.A. Dayananda and R.E. Grace, *Metallurgical Transactions*, **3**, 819 (1972).
45. J.S. Kirkaldy, Zia-ul-Haq and L.C. Brown, *Trans. ASM*, **56**, 384 (1963).
46. M.A. Dayananda and G.E. Murch, ed., *Diffusion in Solids: Recent Developments*, AIME pub., Warrendale, Pa., 195 (1985).
47. L.S. Castleman, *Metallurgical Transactions*, **14A**, 45 (1983).
48. A.D. Romig and M.A. Dayananda, ed., *Diffusion Analysis and Applications*, TMS Pub. (1989).
49. R.T. DeHoff, A.M. Gokhale, C.V. Iswaran and F.R. Assuncao, *Unpublished Research*, (1981).
50. Y. Adda and J. Philibert, *La Diffusion dans les Solides*, **1**, Press Universitaires de France, Paris, 142 (1966).
51. Y. Adda and J. Philibert, *La Diffusion dans les Solides*, **1**, Press Universitaires de France, Paris, 594 (1966).
52. F.J.J. van Loo, G.F. Bastin and J.W.G.A. Vrolijk, *Metallurgical Transactions*, **18A**, 801 (1987).
53. J.E. Morral, Yoon-ho Son and M.S. Thompson, *Acta Metallurgica*, **36**, 1971 (1988).
54. F.J.J. van Loo, B. Pieraggi and R.A. Rapp, *Acta Metallurgica*, **38**, 1769 (1990).

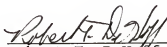
55. B. Pieraggi, R.A. Rapp, F.J.J. van Loo na J.P. Hirth, *Acta Metallurgica*, **38**, 1781 (1990).
56. R.T. DeHoff, *Trans. AIME*, **242**, 608 (1968).
57. M. Chow and C.R. Houska, *Metallurgical Transactions*, **11A**, 111 (1980).
58. A.J. Ardell and R.B. Nicholson, *Acta Metallurgica*, **14**, 1295 (1966).
59. P.G. Shewmon, *Diffusion in Solids*, 2nd ed., TMS pub., Warrendale, Pa., 39 (1989).
60. F.J.J. van Loo, B. Pieraggi and R.A. Rapp, *Acta Metallurgica*, **38**, 1776 (1990).

BIOGRAPHICAL SKETCH

Coimbatore Venkateswaran Iswaran was born in Madras, India, on June 20, 1948. He grew up in New Delhi, India, obtaining his Higher Secondary Certificate under the auspices of the Central Board of Secondary Education, from the Tamil Nadu Educational Association school in Lodhi Estate, New Delhi.

Coimbatore Venkateswaran Iswaran received his Bachelor of Technology degree in metallurgy from the Indian Institute of Technology, Madras, India, in 1969. Subsequently, he came to the United States of America and received his master's degree in materials engineering from Clemson University, Clemson, South Carolina, in 1972. His thesis topic was "Delayed Failure of Titanium as Affected by Impressed Currents."

I certify that I have read this study and that in my opinion it conforms to acceptable standards of scholarly presentation and is fully adequate, in scope and quality, as a dissertation for the degree of Doctor of Philosophy.



Robert T. DeHoff, Chairman
Professor of Materials Science
and Engineering

I certify that I have read this study and that in my opinion it conforms to acceptable standards of scholarly presentation and is fully adequate, in scope and quality, as a dissertation for the degree of Doctor of Philosophy.



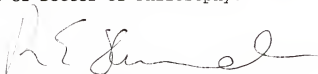
Ellis D. Verink Jr.
Distinguished Service Professor
of Materials Science and
Engineering

I certify that I have read this study and that in my opinion it conforms to acceptable standards of scholarly presentation and is fully adequate, in scope and quality, as a dissertation for the degree of Doctor of Philosophy.



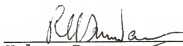
Paul H. Holloway
Professor of Materials Science
and Engineering

I certify that I have read this study and that in my opinion it conforms to acceptable standards of scholarly presentation and is fully adequate, in scope and quality, as a dissertation for the degree of Doctor of Philosophy.



Rolf E. Hummel
Professor of Materials Science
and Engineering

I certify that I have read this study and that in my opinion it conforms to acceptable standards of scholarly presentation and is fully adequate, in scope and quality, as a dissertation for the degree of Doctor of Philosophy.



Kalyan Raman
Assistant Professor of Marketing

This dissertation was submitted to the Graduate Faculty of the College of Engineering and to the Graduate School and was accepted as partial fulfillment of the requirements for the degree of Doctor of Philosophy.

December 1993



Winfred M. Phillips
Dean, College of Engineering

Karen A. Holbrook
Dean, Graduate School